Nuclear Science
NEA/NSC/R(2022)5
March 2023
www.oecd-nea.org

Benchmark Study on Innovative Fuels for Fast Reactors with Fuel Performance Codes

OECD
BETTER POLICIES FOR BETTER LIVES

NEA
NUCLEAR ENERGY AGENCY

Nuclear Energy Agency

NEA/NSC/R(2022)5

Unclassified **English text only**

31 March 2023

NUCLEAR ENERGY AGENCY
NUCLEAR SCIENCE COMMITTEE

Benchmark Study on Innovative Fuels for Fast Reactors with Fuel Performance Codes

This document is available in PDF format only.

JT03515633

ORGANISATION FOR ECONOMIC CO-OPERATION AND DEVELOPMENT

The OECD is a unique forum where the governments of 38 democracies work together to address the economic, social and environmental challenges of globalisation. The OECD is also at the forefront of efforts to understand and to help governments respond to new developments and concerns, such as corporate governance, the information economy and the challenges of an ageing population. The Organisation provides a setting where governments can compare policy experiences, seek answers to common problems, identify good practice and work to co-ordinate domestic and international policies.

The OECD member countries are: Australia, Austria, Belgium, Canada, Chile, Colombia, Costa Rica, the Czech Republic, Denmark, Estonia, Finland, France, Germany, Greece, Hungary, Iceland, Ireland, Israel, Italy, Japan, Korea, Latvia, Lithuania, Luxembourg, Mexico, the Netherlands, New Zealand, Norway, Poland, Portugal, the Slovak Republic, Slovenia, Spain, Sweden, Switzerland, Türkiye, the United Kingdom and the United States. The European Commission takes part in the work of the OECD.

OECD Publishing disseminates widely the results of the Organisation’s statistics gathering and research on economic, social and environmental issues, as well as the conventions, guidelines and standards agreed by its members.

NUCLEAR ENERGY AGENCY

The OECD Nuclear Energy Agency (NEA) was established on 1 February 1958. Current NEA membership consists of 34 countries: Argentina, Australia, Austria, Belgium, Bulgaria, Canada, the Czech Republic, Denmark, Finland, France, Germany, Greece, Hungary, Iceland, Ireland, Italy, Japan, Korea, Luxembourg, Mexico, the Netherlands, Norway, Poland, Portugal, Romania, Russia (suspended), the Slovak Republic, Slovenia, Spain, Sweden, Switzerland, Türkiye, the United Kingdom and the United States. The European Commission and the International Atomic Energy Agency also take part in the work of the Agency.

The mission of the NEA is:

- to assist its member countries in maintaining and further developing, through international co-operation, the scientific, technological and legal bases required for a safe, environmentally sound and economical use of nuclear energy for peaceful purposes;
- to provide authoritative assessments and to forge common understandings on key issues as input to government decisions on nuclear energy policy and to broader OECD analyses in areas such as energy and the sustainable development of low-carbon economies.

Specific areas of competence of the NEA include the safety and regulation of nuclear activities, radioactive waste management and decommissioning, radiological protection, nuclear science, economic and technical analyses of the nuclear fuel cycle, nuclear law and liability, and public information. The NEA Data Bank provides nuclear data and computer program services for participating countries.

Foreword

The Working Party on the Scientific Issues of the Fuel Cycle (WPFC)[1] was established under the auspices of the Nuclear Energy Agency (NEA) Nuclear Science Committee to co-ordinate scientific activities regarding various existing and advanced nuclear fuel cycles, including advanced reactor systems, the associated chemistry and flowsheets, the development and performance of fuels and materials, accelerators and spallation targets. Various expert groups have been established to cover these topics. Within the Working Party on the Scientific Issues of the Fuel Cycle, the Expert Group on Innovative Fuels was created with the objective of conducting joint and comparative studies to support the development of innovative fuels such as homogeneous and heterogeneous fuels; accelerator-driven system fuels; and oxide, metal, nitride and carbide fuels, all of which can be implemented in advanced nuclear fuel cycles with fast reactors. The scope of the expert group covers innovative fuel fabrication techniques, the irradiation performance of innovative fuels, characterisation and post-irradiation examination methods, and predictive codes for innovative fuel fabrication and performance.

This report presents the results of a benchmark study on innovative fuels for fast reactors using fuel performance codes. Irradiation results were shared among participants of the expert group and code calculations were performed to gain further insights on the fuel behaviour. Each participating institution used its own fuel performance code. Code-to-code and code-to-experiment comparisons are expected to provide data on and improve understanding of the effects of minor actinides on fuel behaviour. In conclusion, the need for improving codes will be evaluated and the need for new experimental data identified in order to finalise the code validation.

The NEA Secretariat would like to express its sincere gratitude to the members of the Expert Group on Innovative Fuels for contributing to this report and for providing consistent assessments on fuel issues.

---

[1] Renamed "Working Party on Scientific Issues of Advanced Fuel Cycles (WPFC)" in 2021 (Mandate NEA/SEN/NSC/WPFC(2020)3, not publicly available).

Table of contents

Tables

Figures

Abbreviations and acronyms

AFC	Advanced Fuel Campaign
ALFUS	ALloyed Fuel Unified Simulator
ANL	Argonne National Laboratory (United States)
at.%	Atomic percentage
ASTRID	Advanced Sodium Technological Reactor for Industrial Demonstration
ATR	Advanced Test Reactor
BOI	Beginning of irradiation
BOL	Beginning of life
CEA	Commissariat à l’énergie atomique et aux énergies alternatives (Alternative Energies and Atomic Energy Commission, France)
CEPTAR	Calculation code to Evaluate fuel Pin sTability for AnnulaR fuel design
CH	Central hole
CRIEPI	Central Research Institute of Electric Power Industry (Japan)
DPA	Displacements per atom
EBR	Experimental breeder reactor
EFPD	Effective full power day
EFTTRA	Experimental Feasibility of Targets for TRAnsmutation
EGIF	Expert Group on Innovative Fuels (NEA)
EOI	End of irradiation
EOL	End of life
EXTRA	Exploiting eXascale technology with reconfigurable architectures
FBR	Fast breeder reactor
FCCI	Fuel-cladding chemical interaction
FCMI	Fuel-cladding mechanical interaction
FEM	Finite element method
FFTF	Fast Flux Test Facility
FORTRAN	FORmula TRANslator
FP	Fission product
FGR	Fission gas release
FR	Fast reactor
GEN-IV	Generation 4
HANARO	High flux Advanced Neutron Application ReactOr
HM	Heavy metal
ID	Inner diameter
INL	Idaho National Laboratory (United States)
INTA	Instrumented test assembly

ITU	Institute for Transuranium Elements (Germany)
JAEA	Japan Atomic Energy Agency
JOG	Joint oxyde gaine *(in French)*
JRC	Joint Research Centre (European Union)
KAERI	Korea Atomic Energy Research Institute
KIT	Karlsruhe Institute of Technology (Germany)
LHGR	Linear heat generation rate
LWR	Light water reactor
MA	Minor actinide
MACSIS	Metal fuel rod Analysis Code for Simulating the In-reactor behavior under Steady-state conditions
MBM	MOOSE-BISON-MARMOT
MOOSE	Multiphysics Object-Oriented Simulation Environment
MOX	Mixed oxide
MTR	Material test reactor
NEA	Nuclear Energy Agency
NSC	Nuclear Science Committee
O/M	Oxygen-to-metal
OD	Outer diameter
PDE	Partial differential equation
PFR	Plug flow reactor
PIE	Post-irradiation examination
PPN	Peak power node
PTM	Power to melt
PUMA	Performance of Uranium Metal fuel rod Analysis code
R&D	Research and development
RE	Rare earth element
SEM/EDS	Scanning electron microscopy/energy dispersive spectroscopy
SFR	Sodium-cooled fast reactor
SWLCRP	Swelling creep
TMPOFL	Temperature of fuel shell out surface
TRANSIT	Thermal Property and Vapour Pressure Analysis Module for Minor Actinide Containing MOX Fuel
VVER	Water water energy reactor
WPFC	Working Party on the Scientific Issues of the Fuel Cycle (NEA)

Executive summary

As part of the Nuclear Energy Agency (NEA) Expert Group on Innovative Fuels (EGIF)[2] 2014-2018 activities, seven irradiations under normal operating conditions of metal and oxide fuels for fast reactors were calculated using different fuel performance codes: ALFUS (Central Research Institute of Electric Power Industry, Japan), GERMINAL (French Alternative Energies and Atomic Energy Commission, France), CEPTAR (Japan Atomic Energy Agency, Japan), MACSIS (Korea Atomic Energy Research Institute, Korea), TRANSURANUS (Joint Research Centre Karlsruhe) and FEMAXI-FBR (Karlsruhe Institute of Technology, Germany).

The calculated irradiations – B8-HAM, SUPERFACT, SMIRP-1, AFC-1H, AFC-2C, X501 and METAPHIX-2 – were carried out in the reactors JOYO (Japan), Phénix (France), HANARO (Korea), the Advanced Test Reactor (United States) and EBR-II (United States). The fuels studied were mixed oxides $(U,Pu)O_2$ and metal U-Pu-Zr, with a small percentage of minor actinides (1-5% Am-241, sometimes associated with Am and Cm) with the exception of the SMIRP-1 irradiation fuel of U-10Zr and U-10Zr-Ce.

The objective of this study was to carry out a benchmarking exercise between the different available fuel performance codes devoted to minor actinide (MA) bearing fuels. The study consisted in:

- sharing irradiation data provided by members of the expert group;
- performing code calculations on these irradiations;
- comparing predictions of codes with irradiations results;
- defining improvements needed on codes;
- identifying new irradiations needed to cover a wide range of parameters for complete code validation.

The work performed for the study was organised as follows:

1. Irradiation tests: provision of the set of data needed for code calculations. A template was developed to identify data needed for both the code input data file and the results of post-irradiation examinations to be compared with the code results.
2. Code calculations: participating members carried out a set of calculations for each irradiation with their own codes.
3. Results of calculations were presented.
4. All the results were compared.
5. Conclusions were drawn on fuel performance codes (models, properties, coupled effects). The need for future irradiations was also discussed.

---

[2] Renamed "Expert Group on Innovative Fuel Elements (EGIFE)" in 2021 (Mandate NEA/SEN/NSC/WPFC(2021)4, not publicly available).

Chapter 1 provides the background and the overall objectives of the study. Chapter 2 describes the codes used in the study: history, a description of the methods, validation and capabilities. Chapter 3 details the irradiation experiments selected for the benchmark and describes the fuel characteristics and irradiation conditions. Chapter 4 provides the results of the calculations, analysis and comparison of the codes.

Oxide fuels

Irradiations of AFC-2C, SUPERFACT and B8-HAM were considered and calculations were performed with the codes CEPTAR, FEMAXI-FBR, GERMINAL and TRANSURANUS.

An analysis of the results of the calculations shows some discrepancies between the different codes. One of the most noticeable disagreements between the codes concerns the temperature predictions. This was attributed to the calculations performed on the gap size evolution, the gap thermal conductance and the evaluation of the fuel thermal conductivity. Improvements in the models are therefore recommended to increase the reliability of the codes.

In addition, the presence of MA in the fuel does not appear to be causing any differences in the calculations of the codes.

Metal fuels

Irradiation data of AFC-1H, METAPHIX-2, SMIRP-1 and X501 were shared and calculations were carried out with two codes: ALFUS and MACSIS.

ALFUS and MACSIS reproduced well the data of fuel axial elongation, gas plenum volume and fission gas release. The codes are applicable to short fuel slugs, but some improvements in the models are recommended.

Both codes have a similar level of capability to simulate metal fuel irradiation behaviour. The presence of MA in the fuel does not seem to affect the irradiation behaviour of U-Pu-Zr fuels. However, to fully understand the effects of MA, additional studies are recommended, such as collecting experimental data on fuel-cladding chemical interaction and He behaviour in MA-bearing metal fuel and performing modelling.

Conclusions

Comparing the results from the different codes showed some differences in modelling for both oxide and metal fuels. The effect of minor actinides (up to 5%) in the fuel is not significant and does not change the overall thermochemical behaviour of the fuel. However, the irradiations shared with this benchmark exercise were not highly performant in terms of burnup and transmutation rate. The impact of MA could play a role at higher performance, in particular for helium release, gaseous swelling, increase of oxygen potential and properties degradation, which could favour fuel-cladding chemical interaction and fuel-cladding mechanical interaction.

1. Introduction

1.1. Background

Spent fuel management has become a major concern in the nuclear power sector. One option would be to reprocess the fuel by implementing new innovative technologies in various nuclear fuel cycle schemes. Several NEA (Nuclear Energy Agency) member countries have initiated research and development (R&D) programmes to study the safety aspects of new types of fuel containing minor actinides (MA) for burning under fast neutrons. To review those programmes and the most recent advancements in the field, the NEA Expert Group on Innovative Fuels (EGIF) has published a *State-of-the-Art Report on Innovative Fuels for Advanced Nuclear Systems* (NEA, 2014). This report covers the study of any fuel containing MA to be introduced in advanced nuclear systems and reviews the available data on such MA-bearing fuels. Different fuel types were reviewed (metal, oxide, nitrides, dispersion fuels and special mechanical fuel forms), mainly for fast neutron reactors, examining different technical issues associated with their fabrication, characterisation, irradiation performance and design and safety criteria. The technical maturity of each fuel was also assessed.

Among these fuels, metal and oxide fuels containing MA have been widely investigated, including irradiation tests and post-irradiation examination (PIE). Additional results, however, are needed to gain further insights on He gas release and fuel-cladding chemical interactions (FCCI). Nitride fuels have numerous advantages for use in accelerator-driven systems compared to other types of fuels due to their higher density. However, these fuels are still at an early stage of development and more fundamental research is needed to determine their performance. Dispersion fuels are a relatively new concept. The first irradiation tests of inert matrix fuel containing MA started in the mid-1990s as part of the irradiation programme EFTTRA (Experimental Feasibility of Targets for TRAnsmutation) and was followed by other irradiation programmes. Three types of dispersion fuels have now been subjected to safety tests. Finally, MA can be integrated into special fuel forms (particles) which are considered to be a new concept, namely Vipac and Spherepac. Some irradiation experiments have marked important milestones in the R&D of MA-bearing fuels. However, the fabrication and characterisation of transuranic bearing fuels and the examination of the behaviour and safety issues, are limited to laboratory scale (grammes of transuranics) and their irradiation tests have been limited to small samples or rodlets.

Members of the EGIF decided to continue their activities on innovative fuels by performing calculations with fuel performance codes on some irradiation tests to gain a better understanding of the effects of MA on fuel behaviour.

1.2. Objectives and content of the study

The objective of this study was to perform a benchmark study between the different available fuel performance codes devoted to MA-bearing fuels. The study consisted in:

- sharing irradiation data provided by members of the EGIF;
- performing code calculations on these irradiations;
- comparing predictions of codes with the irradiations results;
- defining improvements needed on codes;

- identifying new irradiations needed to cover a wide range of parameters for a complete code validation.

First, irradiations of interest for the benchmark calculations were identified. It should be noted that, as mentioned above, oxide and metal fuels with a low content of MA have been widely investigated and irradiation tests and PIE have been performed. Phase 1 of the benchmark was dedicated to these types of fuels. Table 1.1 summarises the list of irradiations shared and the codes used by each participating institution to carry out the calculations.

Table 1.1. List of irradiations used in Phase 1 of the benchmark

Fuel	Country	Organisation	Fuel performance codes	Irradiation results to be shared	Type of fuel	Irradiation conditions
Phase 1						
Oxide Low content of minor actinides	United States	INL	MBM[1]	ATR: AFC-2C	(U,Pu,Am$_{2\%}$)Ox	8.18 at.% - 200, 300 W/cm
	France	CEA	GERMINAL	Phénix: SUPERFACT	(U,Pu,Am$_{2\%}$)Ox	6.4 at.% - 415-345 W/cm
	European Union	JRC	TRANSURANUS	Phénix: SUPERFACT	(U,Pu,Am$_{2\%}$)Ox	6.4 at.% - 415-345 W/cm
	Japan	JAEA	CEPTAR	JOYO: B8-HAM	(U,Pu,Am$_{1\%}$)Ox	BOL - 400 W/cm
	Germany	KIT	FEMAXI FBR (steady state or transients)	KNK2: FACT[2]	(U,Am$_{50\%}$)Ox	n/a
Metal Low content of minor actinides	United States	INL	MBM	ATR: AFC-1H,	U-29Pu-4Am-2Np-30Zr U-34Pu-4Am-2Np-20Zr U-25Pu-3Am-2Np-40Zr	26.68 at.% 248 W/cm (time-average)
				EBR-II: X501	U-28Pu-7Am-30Zr U-20.2Pu-9.1Zr-1.2Am-1.3Np	7.6 at.% 450 W/cm
	Japan	CRIEPI	ALFUS	Phénix: METAPHIX-2	U-19Pu-10Zr U-19Pu-10Zr-2MA-2RE U-19Pu-10Zr-5MA-5RE U-19Pu-10Zr-5MA	5.7-6.9 at.% 253-306 W/cm
	European Union	JRC	No	Phénix: METAPHIX-2	U-19Pu-10Zr U-19Pu-10Zr-2MA-2RE U-19Pu-10Zr-5MA-5RE U-19Pu-10Zr-5MA	5.7-6.9 at.% 253-306 W/cm
	Korea	KAERI	MACSIS	HANARO: SMIRP-1	(U-Ce-Zr) without MA	2.4 at.% 128~245 W/cm

Note: BOL: beginning of life, MA: minor actinides (Np, Am, Cm); RE: rare earths (Y, Ce, Nd, Gd)

[1] MBM: MOOSE-BISON-MARMOT.

[2] FACT: irradiation data were not available.

The first phase of the benchmark exercise was organised as follows:

- Irradiation tests: provision of the set of data needed for code calculations. A template was developed to identify data needed for both the code input data file and results of post-irradiation examinations to be compared with the code results.
- Code calculations: participating members carried out a set of calculations for each irradiation with their own codes.
- The results of the calculations were presented to the other participants and all the results were compared.
- Conclusions were derived on fuel performance codes (models, properties, coupled effects). The need for future irradiations was discussed.

The remaining chapters present the results of Phase 1 of the benchmark and summarise the discussions.

References

NEA (2014), *State-of-the-art Report on Innovative Fuels for Advanced Nuclear Systems*, NEA No. 6895, OECD Publishing, Paris, www.oecd-nea.org/jcms/pl_14574.

2. Fuel performance codes

2.1. Oxide fuels

2.1.1. CEPTAR (Japan Atomic Energy Agency)

Introduction and history

The first version of CEPTAR was developed from CEDAR (Code for thErmal and Deformation Analysis of Reactor fuel pin) to evaluate the annular fuel behaviours for fast reactor fuel design in 2006. The models of radial redistribution of MA and Pu, “joint oxyde gaine” (JOG) formation, and fuel restructuring were developed and installed. This code has been improved by applying the latest properties and models up to the present and validated by using the results of several irradiation experiments in JOYO and the steady irradiation in plug flow reactor (PFR) (Ozawa and Abe, 2006). Currently, the latest properties of MA-MOX (minor actinide-mixed oxide) fuels are installed to study MA-MOX fuel behaviour for reducing the degree of hazard and the amount of high-level radioactive wastes. In particular, the computer module TRANSIT (Thermal Property and Vapour Pressure Analysis Module for Minor Actinide Containing MOX Fuel) was developed to compute thermal properties of MA-MOX fuels. TRANSIT can give thermal conductivity, melting temperature and vapour pressures of MA-MOX (Ikusawa et al., 2015).

To improve the thermal calculations, the number of radial meshes in a fuel pellet was expanded from 10 to 50 in the second version of CEPTAR, called CEPTAR.V2, and validated by using the results of irradiation experiments in JOYO (Ozawa et al., 2015).

Brief description of the methods used, validation and capabilities

Figure 2.1 shows the major code structure of CEPTAR.V2. Based on input values for geometries of fuel pellet and cladding, irradiation conditions, and options for fuel and cladding properties, variable values are set and variables except input are set to default values. Once all the variables are defined, burnup and fast neutron fluence and coolant and cladding temperature are calculated. The cladding temperature, i.e. cladding outer temperature, cladding mid-wall temperature or cladding inner temperature, can be directly input instead of coolant flow rate, coolant pressure and equivalent hydraulic diameter. If cladding temperature is not input, cladding outer temperature is calculated based on the coolant temperature calculated from the inlet coolant temperature and the axial power distribution of a fuel rod.

For thermal and mechanical analysis, the cladding and fuel pellet can be radially divided into 6 equal-mass meshes and 50 equal-mass meshes, respectively. The cladding has an additional mesh for the inner corrosion layer. The fuel rod can be axially divided into 20 nodes in addition to 1 node for the upper plenum. The axial migration of materials cannot be taken into account since each axial node is independent for thermal and mechanical analysis.

Subroutine BNDALL (control for boundary conditions) is the control routine for boundary conditions and iterations of thermal and stress-strain analysis, In BNDALL, the fuel outer temperature is calculated from heat transfer in a gap between the fuel pellet and the cladding, and the cladding inner temperature, and obtained by iteration of thermal analysis from the cladding inner temperature to the fuel outer temperature. The fuel temperature is then calculated by using the 1D steady heat conduction cylindrical model, and the fuel centre temperature is obtained by iteration of thermal analysis from the cladding inner temperature to the fuel centre temperature. In addition, prior to stress-strain iteration in subroutine SWLCRP (swelling creep), the thermal expansion deformation of the fuel pellet and the cladding is calculated from the fuel temperature and the cladding temperature, respectively. In SWLCRP, according to generalised plane strain analysis method, the fuel pellet deformation caused by densification, swelling, hot press and creep, and cladding deformation caused by swelling and creep is calculated in addition to elastic strain. Fuel pellet and cladding deformation are obtained by iteration of stress-strain analysis for the fuel pellet and the cladding.

Figure 2.1. Major code structure of CEPTAR.V2

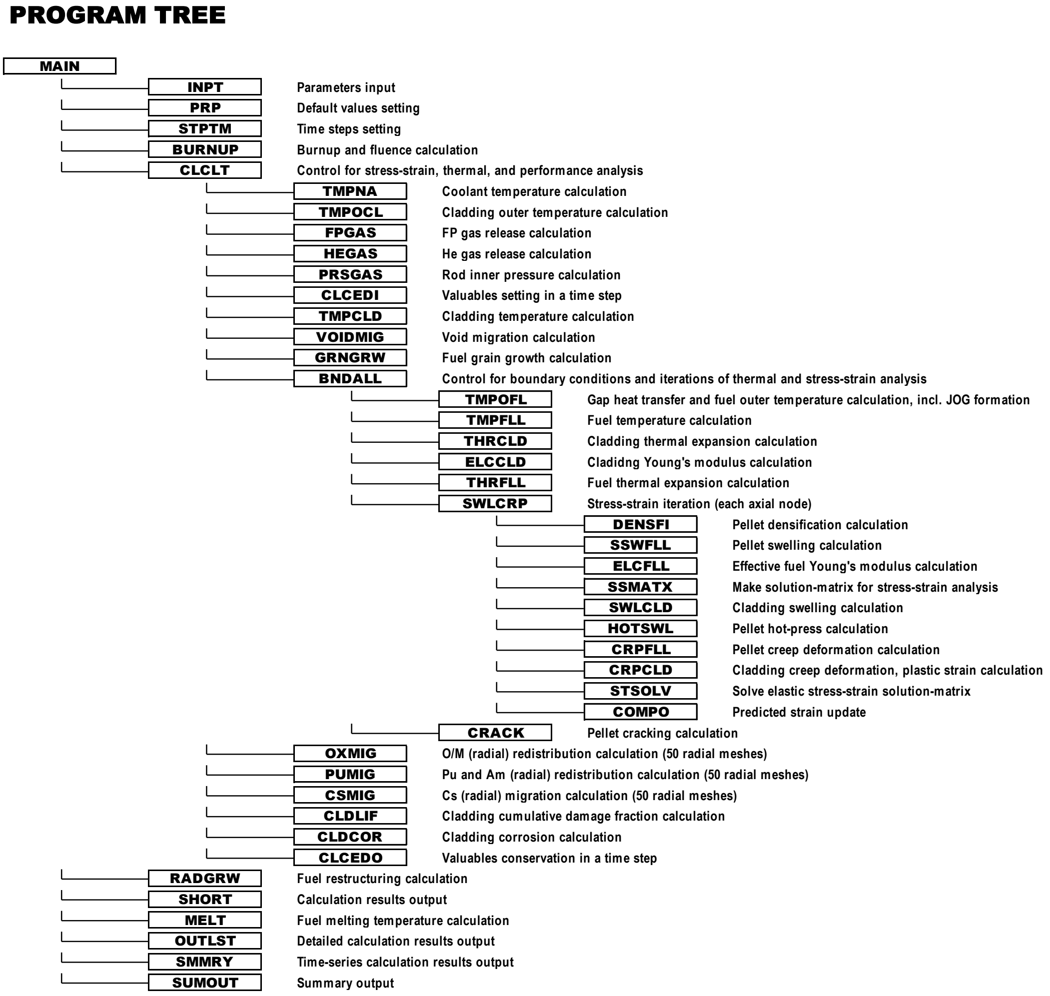

Source: Based on Ozawa and Abe, 2006.

Radial redistribution of caesium is used for JOG formation in subroutine TMPOFL (temperature of fuel shell outer surface). In TMPOFL, heat transfer in a gap is calculated by taking into account the thermal conductivity of JOG based on JOG layer thickness. The radial redistribution of plutonium and americium is calculated as a sum of solid-state transport and vapour phase transport by considering the dependence of the oxygen-to-metal (O/M) ratio, which is radially redistributed, on diffusion coefficient.

Figure 2.2 shows the outline of CEPTAR.V2 connected with TRANSIT. Based on the fuel composition, the O/M ratio and the fuel temperature, which are calculated in CEPTAR, TRANSIT calculates vapour pressure to estimate the velocity of pore migration in CEPTAR.V2. In TRANSIT, based on the Rand-Markin model (Olander, 1976; Ackermann, Faircloth and Rand, 1966), the vapour pressures of vapour species, which were experimentally observed, can be calculated.

Figure 2.2. Outline of CEPTAR.V2 connected with TRANSIT

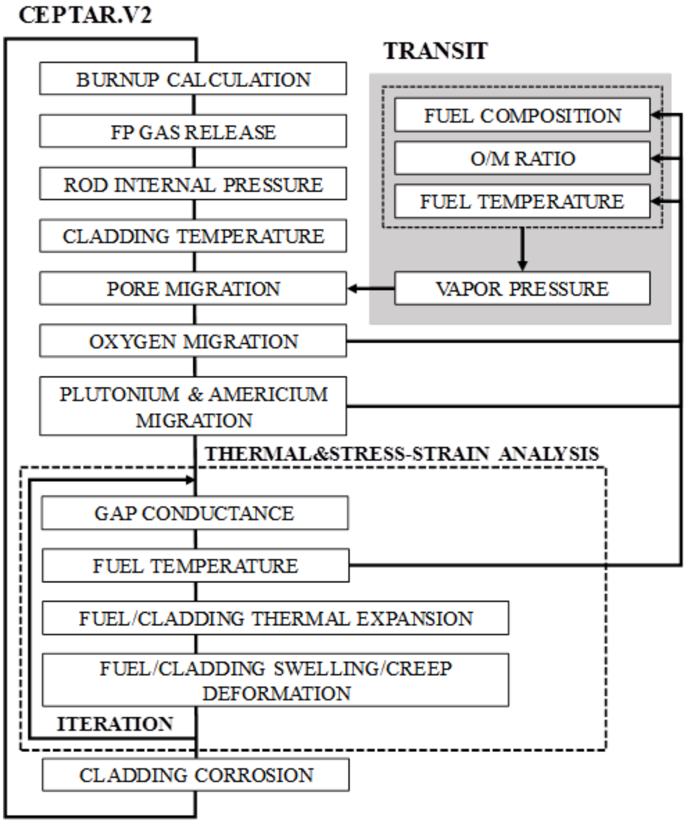

Note: FP: fission product; O/M: oxygen-to-metal.
Source: Based on Ozawa and Abe, 2006.

Code validation and capabilities

The accuracy of thermal calculation for CEPTAR.V2 connected with TRANSIT was verified by using the results of short-term irradiation experiments in JOYO. In this verification, the temperature difference between the cladding inner temperature and the fuel centre temperature (ΔTgap+ΔTfuel) was computed by using the results of instrumented test assembly (INTA) experiments, INTA-1 and INTA-2, and power to melt (PTM) experiments, B5D-2, performed in JOYO (Inoue, Abe and Soto, 2000; Inoue et al., 2003). Figure 2.3 shows the comparison between experimental and computed ΔTgap+ΔTfuel values and indicates that CEPTAR.V2 can calculate the fuel temperature at a higher linear power within 1.5% as a standard deviation (Ozawa et al., 2015). By connecting with TRANSIT, CEPTAR.V2 can be expected to calculate the irradiation behaviour of MA-MOX precisely.

Figure 2.3. Comparison between experimental and computed ΔTgap+ΔTfuel values

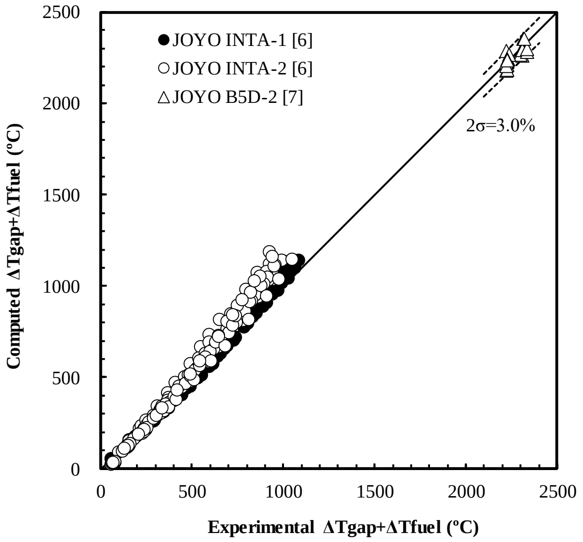

Source: Based on Ozawa et al, 2006.

Table 2.1 defines the applicability of CEPTAR.V2 relative to the main characteristics of the fuel and cladding and the irradiation conditions.

Table 2.1. CEPTAR.V2 applicability

Fuel		Cladding	
Material	UO_2 $(U,Pu)O_{2-x}$ and $(U,Pu,MA)O_{2-x}$	Material	Austenitic SS 316**, PNC1520, c.w.15-15 Ti, AIM1, PNC-FMS, HT-9, Nimonic PE16, ODS
Pellet geometry type	Solid and annular	Outer diameter (mm)	5.8-7.5
Pellet outer diameter (mm)	4.7-6.6	**Fuel pin**	
Pellet inner diameter (mm)	0-2	Type	Homo-/axially heterogeneous
Initial Pu/HM (wt.%)	0-2	** PNC316, c.w.316, c.w.316Ti, M316 85-97	
Initial MA*/HM (wt.%)	19-32		
As-fabricated O/M (-)	0-5		
As-fabricated density (%T.D.)	1.92-2.00		
* MA: Np and/or Am			
Irradiation conditions			
Normal conditions		**Transient conditions**	
Maximum linear heat rating (kW/m)	FR: 67 (solid)/58 (annular) TR: 108 (annular)	Maximum linear heat rating in pre-irradiation (kW/m)	48
Cladding temperature (K)	673-973	Maximum burnup (at.%)	4.6
Fast neutron fluence (n/cm^2)	2.1e23 (PNC316) 5.2e23 (Nimonic PE16)	Base linear heat rating, P0 (kW/m)	66
Maximum burnup (at.%)	16 (solid)/22 (annular)	Transient rate, P/P0	26.26

Note: FR: fast reactor; TR: thermal reactor.

The validation of CEPTAR.V2 was carried out using results of irradiation experiments in JOYO and other foreign fast reactors, i.e. EBR-II, Fast Flux Test Facility (FFTF), PFR, etc. For verifications with short-term irradiation data, or "short-term verifications", thermal data obtained from the INTA experiment and the PTM experiment in JOYO, the EBR-II, the FFTF, and the Material Test Reactor (MTR) in the Harwell laboratory were used.

The main objectives of "short-term verifications" are to verify the computations for the fuel centre temperature and the fuel restructuring. Furthermore, for verifications with long-term irradiation experiments, or "long-term verifications", thermal and mechanical data from the fuel rods irradiated in PFR were used. The main objectives of "long-term verifications" are to verify the computations for the central hole shrinkage and the cladding diameter change. The validation database is as follows:

- Short-term experiments:
    - 15 annular fuel pins in INTA in JOYO;
    - 14 solid fuel pins and 19 top and/or bottom melting extents in the PTM in JOYO;
    - 20 solid fuel pins and 40 top and bottom melting extents in the PTM in the EBR-II;
    - 22 solid fuel pins and 44 top and bottom melting extents in the PTM in the FFTF;
    - 9 annular/solid fuel pins in power ramp in the MTR.
- Long-term experiments:
    - 28 annular fuel pins with M316 cladding and 13 annular fuel pins with PE16 cladding in steady-state irradiation in the PFR.

2.1.2. MOOSE-BISON-MARMOT (US Department of Energy-Idaho National Laboratory)

The fuel simulation codes BISON (Williamson et al., 2012) and MARMOT (Tonks et al., 2012), developed at Idaho National Laboratory (INL), have been built with a vision of multiphysics/multiscale modelling in mind. Both codes are built on the MOOSE framework (Gaston et al., 2009), which is a general partial differential equation (PDE) solver. MOOSE solves PDEs using the finite element method with implicit time integration. The equations are solved fully coupled using the Jacobian-free Newton-Krylov (Knoll and Keyes, 2004) method. They run efficiently on parallel computers.

BISON is a multidimensional nuclear fuel performance analysis code capable of 1D, 2D and 3D simulations. It is applicable to engineering scale analysis of light water reactor (LWR) fuel, TRISO-coated fuel particles (Hales et al., 2013) and metal fuels (Medvedev, 2012; Carlson, Unal and Galloway, 2013). Typically, the PDEs that BISON solves are the energy and solid mechanics equations for temperature and displacements, respectively. BISON's capabilities include a selection of fuel and cladding thermal and mechanical material models, fission gas release, thermal and mechanical contact, evolving gap conductivity and pressure, axial and radial power scaling, fuel densification and swelling, and other models. Due to the evolution of gap size between fuel and cladding in an LWR, solving the energy and mechanics equations in a fully coupled manner is very important. It is also possible to run BISON coupled with a neutronics code (Hales et al., 2015).

MARMOT is a multiphysics mesoscale simulation code focused on modelling the co-evolution of microstructure and material properties. In MARMOT, the system of phase field PDEs is solved simultaneously with PDEs defining additional physics such as heat conduction and solid mechanics. MARMOT takes advantage of advanced tools such as automatic mesh and time step adaptivity. It has been used to model various micro-structural phenomena, ranging from grain boundary migration to bubble growth and coalescence.

At this stage of the benchmark, the development of MOOSE-BISON-MARMOT is not achieved to perform a calculation for fast reactor fuels; therefore, it was not possible for the INL to carry out any calculations.

2.1.3. TRANSURANUS (JRC Karlsruhe)

Introduction and history

TRANSURANUS is a computer programme written in FORTRAN95 for the thermal and mechanical analysis of fuel rods in nuclear reactors that is owned by the Joint Research Centre (JRC) of the European Commission and used by research centres, nuclear safety authorities, universities and industrial partners. TRANSURANUS code users receive a manual, training courses and a licence agreement. The users' network exceeds 40 organisations and meets at regular workshops to discuss problems and define common future priorities.

The development of the TRANSURANUS code began in 1973 at the Technical University Darmstadt (Germany) under the leadership of Prof. K. Lassmann, and in parallel from 1978-82 at the Karlsruhe (Germany) Research Centre (URANUS Code) (Lassmann, 1978). The work was taken over by the JRC at the Institute for Transuranium Elements (ITU) in 1982. After the restructuring of the JRC in 2016, maintenance and development of TRANSURANUS have been pursued at the JRC's Directorate for Nuclear Safety and Security in Karlsruhe, Germany.

The modular code is adapted to individual fuel requirements (Lassmann, 1992; Lassmann, Ronchi and Small, 1989). Oxide, carbide and nitride fuels have all been modelled. In the 1980s, TRANSURANUS was coupled with the European Accident Code, which analysed a hypothetical "fast breeder" reactor (FBR) core accident. In the 1990s, development focused on high burnup models for LWRs (Lassmann et al., 1994; 1995) and a version for Russian-type VVER pressurised water reactors (Lassmann and van de Laar, 1998).

After 2000, a project was launched to extend the TRANSURANUS code capabilities to design-basis accident conditions (Van Uffelen, 2008). The EXTRA (Exploiting eXascale Technology with Reconfigurable Architectures) project (Győri, 2004) focused on the simulation of the Zr1%Nb cladding performance under loss-of-coolant accident conditions and had two main objectives: 1) the compilation of a new database containing VVER-specific experiments to provide an appropriate background for model development and code validation; and 2) the improvement of the TRANSURANUS fuel performance code via the incorporation of newly developed correlations for off-normal conditions. Extensive code validation computations and applications in the safety analyses of VVERs were also carried out. In parallel to this project, similar models for Western-type pressurised water reactors have been implemented and tested as well (Spykman et al., 2004).

After 2010, code developments for design-basis accident conditions in LWRs were pursued to allow larger cladding deformations to be simulated (Di Marcello et al., 2014b). Moreover, considerable development efforts were focused on physics-based modelling of fission gas release (Pastore et al., 2013). The TRANSURANUS model for plutonium and americium redistribution in FBR MOX fuel has also been refined (Di Marcello et al., 2014a; 2012) and is of particular importance for the present benchmark on innovative fuels.

It is based on the PUREDI (plutonium redistribution) model (Lassmann, 1992) and includes the effects of O/M, burnup and their feedback, leading to a consistent numerical structure that couples redistribution phenomena (plutonium and oxygen) together with thermal and nuclides analyses.

International benchmark exercises are of high importance for developing simulation systems of various nuclear reactor components. One of the main benefits is the possibility for cross-comparison and complementary validation of a large number of codes involved. Regarding the performance of nuclear fuel rods, four such exercises have been organised over the last three decades: D-COM in the mid-1980s (Misfeldt, 1983), FUMEX-I from 1992 to 1996 (Chantoin, Turnbull and Wiesenack, 1997), FUMEX-II from 2002 to 2007 (IAEA, 2012), FUMEX-III from 2008 to 2012 (IAEA, 2013a) and FUMAC from 2014 to 2019 (IAEA, 2019). Though the scope of experiments available for international projects in the public domain is limited, they are a unique basis for code-to-code comparisons, as well as for identifying common priorities and needs for further development.

Brief description of the methods used, validation and capabilities

TRANSURANUS is generally referred to as a fuel performance code, meaning that it solves the equations for the radial heat transfer, the radial displacement along with the stress distribution in both the fuel and the surrounding cladding, and describes the fission product behaviour as a function of time. The equations embody the following phenomena:

- thermal performance: heat conduction, radiation and convection;
- mechanical performance: creep, densification, thermal expansion, pellet cracking and relocation, solid and gaseous swelling;
- actinide behaviour: depletion and build-up of main Th, U, Np, Pu, Am and Cm nuclides, impact on the radial power profile;
- fuel restructuring: Pu and Am redistribution, grain growth (normal and columnar), central void formation;
- fission product behaviour: creation in the fuel matrix, diffusion to grain boundaries (Lassmann and Benk, 2000), release to free rod volume after saturation of grain boundaries, a-thermal release, formation of high burnup structure (depletion and porosity).

Main assumptions for thermal performance

The heat conduction in fuel and cladding is based on the Fourier equation for the local temperature T at time t and radial position r:

$$\rho c \frac{\partial T}{\partial t} = \frac{1}{r}\frac{\partial}{\partial r}\left(\lambda r \frac{\partial T}{\partial r}\right) + q'''$$

where ρ is the density, c is the specific heat at constant pressure, λ is the thermal conductivity and q’” denotes the local power density. The heat transfer in the fuel-to-cladding gap is simulated by means of a combination of heat conduction, radiation and convection (URGAP model [Lassmann and Hohlefeld, 1987]).

Main assumptions and equations for mechanical performance[3]

The geometric problem is confined to one-dimensional, plane and axi-symmetric idealisation, i.e. the axial deformation is constant across the radius. The elastic constants E (Young's modulus of elasticity) and ν (Poisson ratio) are isotropic and constant within a cylindrical ring. The total strains ε^{tot}, are split into elastic ε^{el} and non-elastic parts ε^{ex}:

$$\underline{\varepsilon}^{tot} = \underline{\varepsilon}^{el} + \sum \underline{\varepsilon}^{ex}$$

Both strains ε and stresses σ have radial (r), tangential (t) and axial (a) components with the constitutive equations given by:

$$\underline{\varepsilon} = \begin{Bmatrix} \varepsilon_r \\ \varepsilon_t \\ \varepsilon_a \end{Bmatrix} \quad \begin{aligned} \varepsilon_r^{el} &= \frac{1}{E}\left[\sigma_r - \nu\left(\sigma_t + \sigma_a\right)\right] \\ \varepsilon_t^{el} &= \frac{1}{E}\left[\sigma_t - \nu\left(\sigma_r + \sigma_a\right)\right] \\ \varepsilon_a^{el} &= \frac{1}{E}\left[\sigma_a - \nu\left(\sigma_r + \sigma_t\right)\right] \end{aligned}$$

All volume changes due to different processes, such as densification and swelling or cracking, are expressed via strains. The assumptions, together with the compatibility equations:

$$\varepsilon_r = \frac{du}{dR} \qquad \varepsilon_t = \frac{u}{R} \qquad \varepsilon_a = \text{constant} = C_3$$

and the equation of equilibrium:

$$\frac{d\sigma_r}{dR} = \frac{\sigma_t - \sigma_r}{R}$$

lead to the classical semi-analytical solution of the radial deformation u:

$$\begin{aligned} u(R) \quad = \quad & \frac{1-2\nu}{2(1-\nu)}\left\{\frac{1}{R}\int_{R_i}^{R} R\,(\varepsilon_r^{ex} + \varepsilon_t^{ex})\,dR + R\int_{R_i}^{R} \frac{\varepsilon_r^{ex} - \varepsilon_t^{ex}}{R}\,dR\right\} \\ & + \frac{\nu}{1-\nu}\,\frac{1}{R}\int_{R_i}^{R} R\,\varepsilon_{tot}^{ex}\,dR \\ & + C_1 R + \frac{C_2}{R} \end{aligned}$$

where R denotes the radius of the deformed geometry. The constants C_1 and C_2 are determined by means of boundary conditions.

Main assumptions and equations for actinide concentrations[4]

In the TUBRNP model, the calculation of the radial power profiles is split into (a) the approximation of the neutron flux through thermal diffusion theory, and (b) the

---

[3] See Lassmann (1978) and Lassmann and Blank (1988) for a more detailed discussion.

[4] See Lassmann et al. (1994), Lassmann et al. (1998); Di Marcello et al. (2012), Schubert et al. (2008), and Botazzoli et al. (2011) for a more detailed discussion.

computation of the local concentrations of the relevant actinide isotopes with simplified depletion equations. The most recent extension covers the nuclides ^{232}Th, $^{233\text{-}236,238}$U, ^{237}Np, $^{238–242}$Pu, ^{241}Am, ^{243}Am, $^{242–245}$Cm. The general depletion equations read:

$$\begin{aligned} dN_m(r) &= \left[-\sigma_{a,m}N_m(r)f_m(r) + \sigma_{c,m-1}N_{m-1}(r)f_{m-1}(r)\right] \cdot A(r) \cdot dbu(r) \\ &\quad + \left[\sum_i N_i(r)\lambda_i - N_m(r)\lambda_m\right]dt \end{aligned}$$

where Nm(r) is the local concentration of the nuclide; m, $\sigma_{a,m}$ and $\sigma_{c,m}$ are the one-group effective cross-sections for total neutron absorption and neutron capture, respectively; λ_i is the decay constant of nuclide I; A(r) is a conversion factor; dbu(r) is the local burnup increment; dt is the time increment; and $f_m(r)$ is a form factor that reflects the radial dependence of absorption of epi-thermal or resonance neutrons. This factor is applied to ^{238}U and ^{240}Pu. More details are given in Botazzoli et al. (2011).

The thermal heat transfer problem is solved by means of an iterative process that makes use of the finite difference scheme in the radial direction. The equations for the mechanical problem are solved by means of a combination of finite differences (in time) and finite elements (in space).

The axial and radial discretisation of both fuel pellets and cladding are flexible. Once the behaviour of the fuel is computed in each slice, they are coupled in the code via balance equations that regard displacement and axial friction forces. For this reason, standard fuel performance codes are so-called 1.5D codes, while 2D (3D) codes solve the equations simultaneously in two (three) dimensions. Beside the axial friction forces, TRANSURANUS also allows modelling the pellet-clad contact over no-slip condition or slip condition.

The TRANSURANUS code consists of a clearly defined mechanical-mathematical framework into which additional physical models can easily be incorporated. The code has a comprehensive material data bank for oxide, MOX, carbide and nitride fuels, Zircaloy and steel claddings, and several different coolants (water, sodium, potassium, lead, bismuth). TRANSURANUS can be used as a single code system for simulating both long-term irradiations under normal operating conditions as well as transient tests. The "restart" mode allows simulating refabricated fuel rods, e.g. where the fill gas has been completely changed.

The code can be employed in two different versions: as a deterministic and as a statistical code. A combination of restart and Monte Carlo statistics may be used to perform a probabilistic analysis employing the Monte Carlo technique only after the restart. This option may be helpful for the analysis of a long base irradiation followed by a transient. Figure 2.4 gives an overview of these possibilities.

Besides its flexibility for fuel rod design, the TRANSURANUS code can deal with a wide range of different situations, as given in experiments, under normal, off-normal and accident conditions, although some models specific for reactivity-initiated accidents (e.g. plenum temperature) are under development. Furthermore, the code is used for boiling water reactors, pressurised water reactors and VVERs. The time scale of the problems to be treated may range from milliseconds to years. Thus, complex irradiation experiments can be simulated, including refabricated instrumented fuel rods and changing operating conditions.

Figure 2.4. Overview of (a) deterministic analysis, (b) Monte Carlo statistics and (c) a combination of restart and Monte Carlo statistics

a) deterministic analysis; multiple restarts

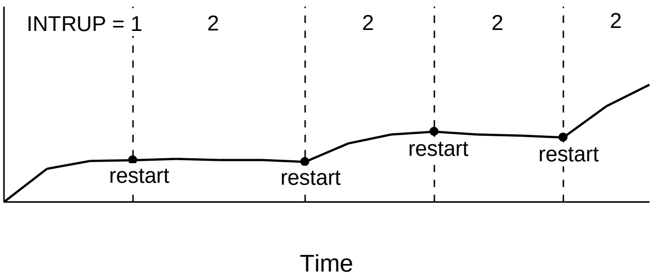

b) Monte Carlo statistics

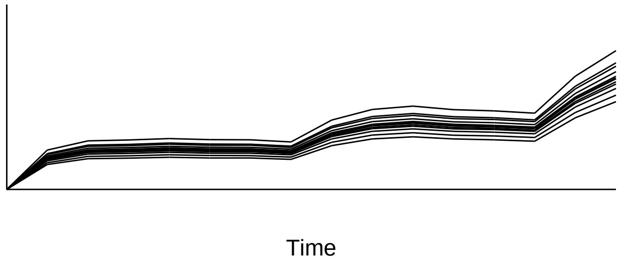

c) Combination of restart and Monte Carlo statistics

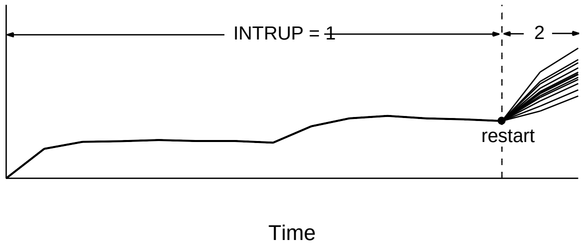

Source: JRC, 2019.

Since its inception, the development as well as the verification of the code is carried out following rigorous quality procedures, and is organised in three steps. The first step consists of verifying the mechanical-mathematical framework. To this end, the models in the code are compared with exact solutions, which are available in many special cases (analytical verification), and several solution techniques are tested, which are applied to optimise the numerical analysis. During the second step, extensive verification of separate models incorporated in the fuel performance code is performed on the basis of separate-effect data. In the third and final step, the verification is completed by code-to-code evaluations as well as comparison with experiments in the frame of international benchmarks organised by the International Atomic Energy Agency and the NEA (see above).

The TRANSURANUS code was originally developed for FBR fuels since 1974. Thanks to its modular structure and robust numerical algorithms, the TRANSURANUS code is stably applicable to the operational conditions of fast reactors in terms of power, fast neutron flux, fuel and cladding temperatures, local deformation as well as local concentrations of major and minor actinides. As the broad validation base of the code has, however, focused on integral experiments under LWRs and heavy water reactors conditions since the 1980s (covering measured fuel temperatures, fission gas release and fuel rod deformation), there is so far no comprehensive comparison of TRANSURANUS simulations to analogous experimental data from fast reactor irradiation experiments. It should be noted that any in-pile measurements under fast reactor conditions are more challenging, hence scarcely available in the open literature (IAEA, 2013b). Since 2003, Euratom joined the GEN-IV initiative and resumed some modelling of FBR fuels. Accordingly, a first summary of improvements for modelling fast reactor rods can be found in Di Marcello et al. (2011). A partial validation of the TRANSURANUS code for fast reactor conditions includes actinide redistribution and central void geometry in two fuel pins irradiated in the Phénix reactor (Di Marcello et al., 2012) and seven fuel pins irradiated in the JOYO reactor (Di Marcello et al., 2014a).

2.1.4. GERMINAL (Alternative Energies and Atomic Energy Commission)

Introduction and history

GERMINAL is a fuel performance code developed by the French Alternative Energies and Atomic Energy Commission (Commissariat à l’énergie atomique et aux énergies alternatives, CEA) and dedicated to the simulation of the in-pile behaviour of sodium-cooled fast reactor (SFR) MOX fuel pins.

GERMINAL is maintained and evolved within the PLEIADES (Marelle et al., 2017) simulation platform. PLEIADES is a unified framework for fuel performance codes, co-developed by the CEA, EDF and Framatome. It includes common resources (solvers, material laws, models, databases) to be shared between different applications, each one dedicated to a precise fuel concept.

A first version of GERMINAL (Melis et al., 1992; Melis, Piron and Roche, 1993; Roche and Pelletier, 1999) was developed from 1980 to 2000, gathering progressively the modelling of the behaviour of Phénix and Superphénix fuel elements. When the ASTRID project was launched in 2006, the decision was taken to update the fuel performance code to support the design studies of the future technological SFR demonstrator in France. Thus, the development of a new version of GERMINAL was realised within the PLEIADES platform, with the goal to provide an updated simulation tool, validated for normal and off-normal conditions. By the end of 2013, GERMINAL V2 (Lainet et al., 2011, 2013; Bouineau et al., 2011) was delivered for use to all partners contributing to ASTRID fuel elements design.

Since then, work has been pursued to improve the modelling of different physical mechanisms having a strong influence on the design criteria evaluation (Lainet et al., 2017, 2019; Michel et al., 2017).

The next section gives a general overview of GERMINAL V2 and ends with a summary of working perspectives.

Brief description of the methods used, validation and capabilities

Fuel pin representation

GERMINAL V2 uses a 1.5D axisymmetric representation of the fuel pin geometry, as illustrated in Figure 2.5. The fuel pin is divided into several axial slices, whose thermal evolutions are coupled by the energy transported by the coolant. Practically, the axial slicing may use from 10 to 40 slices. The slicing definition is correlated first to the fuel column composition: heterogeneous columns usually require more meshes to represent the different parts in a proper way. When simulating an object for code validation, a pertinent slicing may correspond to the axial sampling of experimental data. The discretisation of linear heat rate and cladding damage along the fuel pin also has to be considered; thus, the fuel pin slicing can be adapted according to the core axial power shape by using a non-regular slicing with refined meshes near the power peak.

Figure 2.5. 1.5D fuel pin representation used by GERMINAL V2

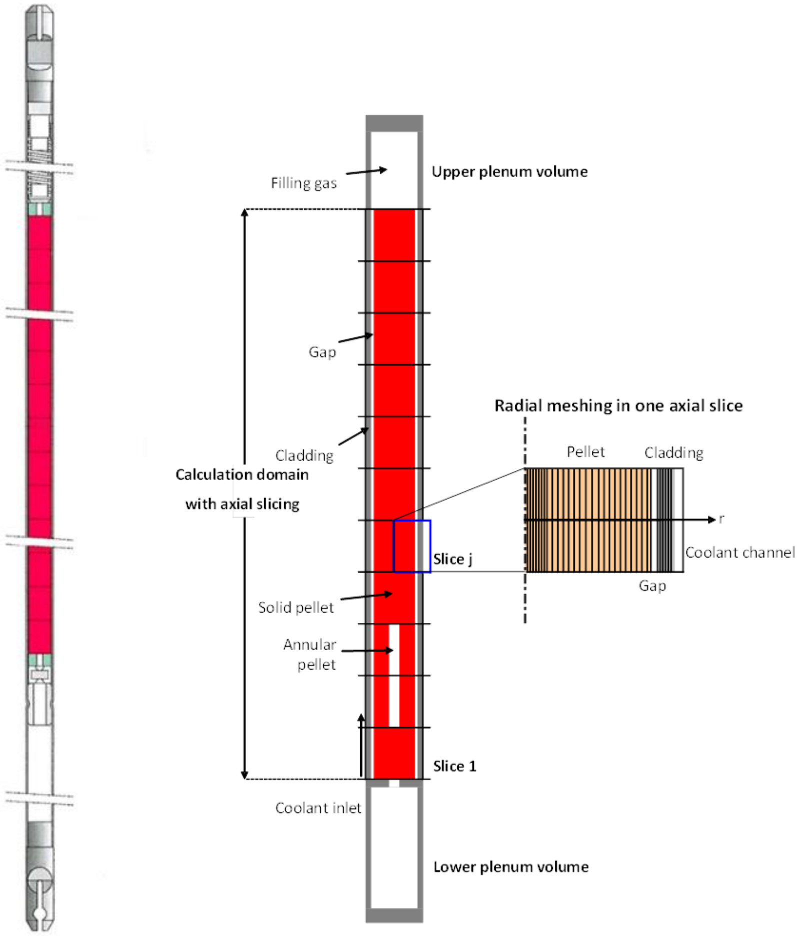

Source: Lainet et al., 2019.

In each axial slice, the resolution of the physical processes uses a radial meshing representing the fuel pellets, the fuel-to-cladding gap and the cladding. The radial meshing of the fuel is more refined near the centre to describe the central hole formation or evolution in case of annular fabricated fuel pellets with a satisfactory precision. The adjusted meshing topology to simulate the validation objects represents a compromise between reasonable calculation times and correct agreement with measures. It includes 25 radial meshes, whose size is growing in geometric progression from 50 µm near the centre to 200 µm at the periphery. For the cladding, a regular meshing with 10 elements in the thickness is usually used; the mesh size is about 50 µm.

The use of a 1.5D calculation scheme leads to an average model size of about 1 000 degrees of freedom, estimated with 25 axial slices. This little model size allows short calculation times, and this is a requirement for study processes – such as uncertainty analyses – which involve thousands of simulations. This type of application is now currently used in fuel elements design (Blanc et al., 2017).

Calculation sequence

GERMINAL V2 determines the evolution of the fuel pin all along its irradiation step by step. The resolution of one-time step is executed according to the sequence defined in Figure 2.6. In this description, global resolutions refer to physical processes affecting the fuel pin in its whole height, whereas local resolutions refer to processes evaluated in one considered axial slice.

Figure 2.6. One-time step resolution by GERMINAL V2

Global resolutions needed by the local resolutions to come

- ☞ Simplified thermal-hydraulics of coolant channel
  Determines the boundary conditions for the local thermal analyses to come: cladding outer temperature in each axial slice
  N.B. Preliminary resolution for a stationary analysis only.
  For a transient analysis, coolant thermal-hydraulics is coupled with fuel pin thermal analysis in each axial slice.

Local resolutions ⇔ Loop on axial slices

- ☞ Neutronics
- ☞ Calculation of average (oxygen-to-metal) (burnup dependent)
- ☞ Local convergence loop
  - ⇒ Thermal analysis of fuel and cladding
    Coupled with coolant thermal-hydraulics for a transient analysis
  - ⇒ Thermally activated fuel physical processes
    - → Oxygen radial migration
      N.B. Time-periodic update with a specific time step criterion
    - → Fuel irradiation shrinkage
    - → Fuel swelling (gas and solid swelling)
    - → Fuel pellet fragments relocation
    - → Gaseous and volatile fission products behaviour
      Includes “joint oxyde gaine” formation
  - ⇒ Mechanics of fuel and cladding
- ☞ Oxygen potential calculation
  N.B. Time-periodic update with a specific time step criterion.
- ☞ Major actinides radial redistribution
  N.B. Time-periodic update with a specific time step criterion.
- ☞ Fuel restructuring: radial migration of porosities, central hole formation
  N.B. Time-periodic update with a specific time step criterion.

Global resolutions needing the previous local resolutions

- ☞ Plenum gas composition and pressure
- ☞ Fuel column axial relocation
- ☞ Cladding internal and external corrosion
- ☞ Fuel column compression spring reaction

Source: Lainet et al., 2011.

The physical processes arising during the fuel pin irradiation are strongly coupled. Thermal analysis is at the centre of these couplings, having direct interactions with mechanics and fuel physics, and relaying the effects of mechanics on fuel physics. Finite elements computations with CAST3M (Verpeaux, Challas and Millard, 1988) solver are involved for thermal analysis and mechanics.

Code applicability and validation

Table 2.2 shows the applicability of GERMINAL V2 relating to the main characteristics of the fuel and cladding and the operating conditions.

Table 2.2. GERMINAL V2 applicability

Fuel	
Material	$(U,Pu)O_{2-x}$, $(U,MA)O_2$, UO_2
Pellet geometry	Solid / Annular
Pellet ϕ_{ext}	[4,2 → 12,2] mm
Pellet ϕ_{int}	[0 → 2,5] mm
Initial Pu/M	[0 → 45] %
Initial MA/M	[0 → 21] %
As-fab. O/M	[1,926 → 1,999]
As-fab. density	[85 → 98] %Dth

MA: Minor Actinides, Np and/or Am

Cladding	
ϕ_{ext}	[5,1 → 28,0] mm
Materials	Austenitic steels: 316*, cold work 15-15 Ti and AIM1 Inconel 706, Nimonic PE16 EM12, HT9
Fuel pin	
Types	Homogeneous Axially heterogeneous

* Tempered 316, cold work 316, cold work 316 Ti

Operating conditions			
Normal operating conditions		Power transients (CRWA, TOP)**	
Linear heat rate	[50 → 590] W/cm	LHR max. (RIA)	→ 1300 W/cm
Clad nominal temp.	[550 → 700] °C	Pmax / Pn (TOP)	→ 26,3
Damage	[0 → 155] dpa	Coolant temp.	→ 900 °C
Burn-up	[0 → 23,7] at.%		

** Control Road Withdrawal Accident
Transient Over Power

The validation of GERMINAL V2 was carried out by using a selection of 100 objects extracted from the CEA database BREF. BREF is a manufacturing, irradiation and post-irradiation examination database for SFR fuel pins, containing information about more than 5 000 objects. These selected objects can be classified by technological type:

- Phénix standard geometry:
    - 45 fuel pins of internal core; 10 fuel pins of external core.
- Phénix geometry, non-standard objects:
    - one pin with annular pellets;
    - four pins loaded with MA;
    - three heterogeneous pins;
    - four fertile pins.

- Other geometries than Phénix:
    - 2 PFR fuel pins; 6 RAPSODIE pins; 6 CABRI1 pins;
    - 15 SUPER-PHÉNIX 1-fuel pins with annular pellets;
    - 1 pin with CAPRA oxide fuel.

Phénix operation clearly provides the most feedback for GERMINAL V2 validation. The validation database also includes the 15 Superphénix 1-fuel pins with annular pellets of larger diameter and other specific designs or compositions (e.g. the 3 Phénix heterogeneous pins or MA-bearing fuels).

The GERMINAL V2 validation base also includes eight transient tests operated in the CABRI reactor, reproducing off-normal conditions such as power ramps or reactivity insertion accidents.

Working perspectives

A constant effort is maintained to improve the modelling carried out with GERMINAL (Lainet et al., 2019) to obtain simulations that are closer and closer to observations. Current work based on tri-dimensional simulations of the fuel fragments (Michel et al., 2017) will result in a revision of the fuel fragment relocation model, to be used by the 1.5D calculation scheme. The study of pellet-clad mechanical interaction also reveals the need to update characterisations of the fuel material. Another axis of work is the implementation of a coupling of GERMINAL with the OpenCalphad (Sundman et al., 2015) thermochemistry component. This represents the starting point for future evolutions to evaluate heat removal at high burnup, in the presence of a JOG, and also to evaluate cladding integrity with a refined estimation of corrosion. In addition, a new major version of GERMINAL is now being developed within the PLEIADES simulation framework, whose main goal is to improve computation performance through parallel implementation. This future version of GERMINAL will naturally integrate all modelling evolutions currently underway.

2.1.5. FEMAXI-FBR (Karlsruhe Institute of Technology)

Introduction and history

The FEMAXI-FBR code (Okawa et al., 2015) is the module devoted to the fuel behaviour calculation of the core disruptive accident analysis code ASTERIA-FBR for fast reactors (Ishizu et al., 2012).

The FEMAXI-FBR code was developed based on the FEMAXI-6 code (Suzuki and Saitou, 2005). Since the FEMAXI-6 simulates the behaviour of LWR fuels, models for the fuel restructuring and material relocation have been included to take into account the differences with the FBR fuels. The material properties implemented in the code are based on empirical correlations from FBR irradiation data. The FEMAXI-FBR code simulates the FBR fuel pin behaviour at steady state. In addition, for the purpose of application for the core disruptive accident analysis code, it includes models to simulate fuel behaviour during transient and at pin failure conditions, estimating fuel melting and expansion, cavity formation, gas release and pressure increase inside the pin.

As shown in Figure 2.7, an axial-symmetric finite element scheme is adopted in which the fuel and the cladding are modelled into a maximum of 40 axial nodes. The fuel and the cladding are represented respectively through ten and two radial nodes.

Brief description of the methods used, validation and capabilities

Thermal analysis models

The FEMAXI-FBR code calculates fuel pin behaviour taking account of the thermalhydraulics of the coolant. The thermal analysis models calculate the temperature distributions in the fuel rod and inside the fuel pellet, taking into account the boundary conditions on the cladding surface, as the cladding temperature profile imposed by the user or the flow conditions of the coolant. The gap conductance is evaluated by the gas composition, gap width and contact force between the pellet and the cladding at the gap closure. Once the temperature distribution is established, the fission products gas release rate, the structure grain diameter variation, the fuel rod gas pressure and the relocation of the fuel and the voids are evaluated. The fission gas release model is the same as the FEMAXI-6, which models the intra-granular fission product gas diffusion and the intergranular growth of bubbles and their connection for the release.

Mechanical analysis models

The mechanical analysis models calculate fuel and cladding stresses and displacements by an axisymmetric finite element method (FEM) for the fuel rod over the total pin length. The variation of the fuel geometries, the fuel cracking, relocation, swelling and densification are modelled and calculated. The mechanical analysis models estimate the strains due to densification, swelling and thermal expansion. In case of mechanical interaction between the pellets and cladding, the related stress and deformation are calculated.

As shown in Figure 2.7, the thermal and mechanical analyses are iterated until convergence within the time step.

Figure 2.7. FEMAXI-FBR geometry model and calculation flow

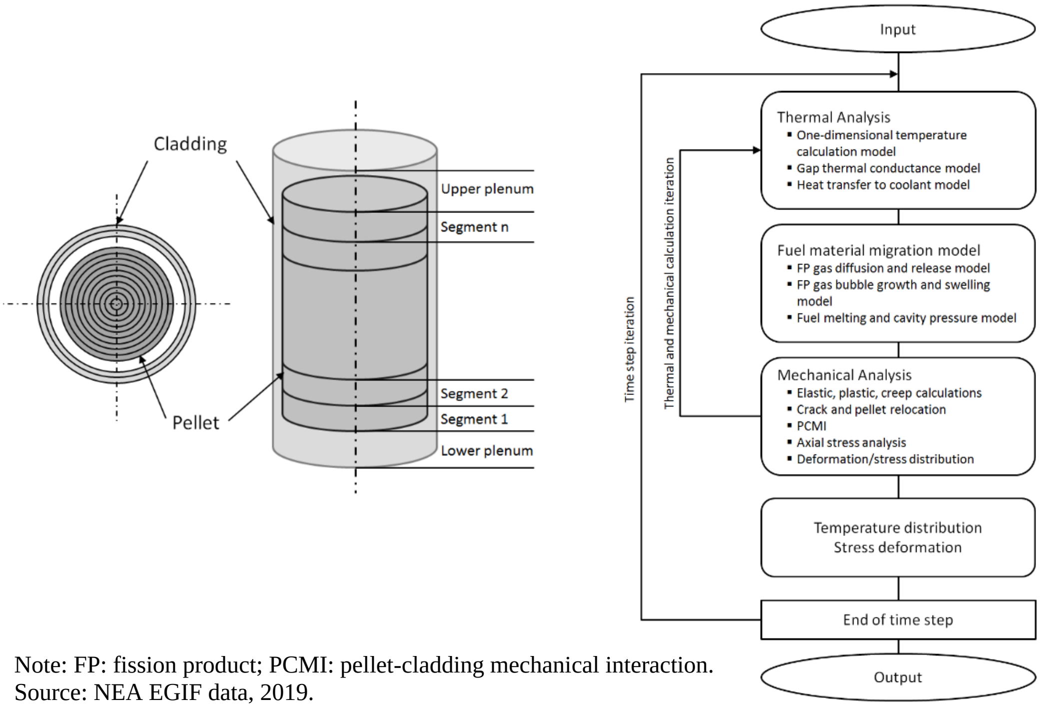

Note: FP: fission product; PCMI: pellet-cladding mechanical interaction.
Source: NEA EGIF data, 2019.

Validation of FEMAXI-FBR

The FEMAXI-FBR thermal analysis model has been validated by the B5D-2 PTM test performed in the experimental fast reactor JOYO at the JAEA Oarai Research and Development Center (Okawa et al., 2015; Inoue et al., 2003). The experimental data of the transient test E12 and BI2 conducted at the CABRI reactor in Cadarache have been compared with FEMAXI-FBR calculation results for the validation of the pin failure models (Okawa et al., 2015; Tsuboi et al., 2012).

2.2. Metal fuels

2.2.1. MACSIS (Korea Atomic Energy Research Institute)

Introduction and history

MACSIS (Metal fuel rod Analysis Code for Simulating the In-reactor behaviour under Steady-state conditions) (Hwang et al., 1998; Lee et al., 2004; Kim, 2014) is a computer programme to predict the in-reactor behaviour of metal fuel pins under normal operating conditions of a sodium-cooled reactor. MACSIS was developed as a design tool and fuel performance analysis for metallic fuel pins by adding the models and features specific to metal fuel.

Since 2012, the Korea Atomic Energy Research Institute's (KAERI) new SFR metal fuel performance analysis code, PUMA (Performance of Uranium Metal fuel rod Analysis code), has been developed through a multiphysics approach with one-level Newton scheme by using backward differentiation formula (Cheon et al., 2013). PUMA is not yet ready for fuel performance analysis, since some additional thermal and mechanical models need to be incorporated into it. Verification and validation of PUMA is planned to be carried out in a few years with irradiation data.

Brief description of the methods used, validation and capabilities

MACSIS is a computer code that calculates the in-reactor performance characteristics and dimensional changes of metal fuel pins in a fast neutron environment. It is comprised of a series of subroutines that model fast reactor fuel phenomena. Models in MACSIS were developed to the EBR-II (Experimental Breeder Reactor-II) irradiation test data published. For validation purposes, calculations of the total of 43 fuel pins in the EBR-II X419, 420, X421, X423, X425 and X447 experiments were carried out to verify each model (fuel constituent redistribution, temperature prediction, fission gas release and cladding strain). The results showed that MACSIS' predictions agree well with the available irradiation data.

The fuel column is divided axially into a user-specified number of segments with equal height (equal fuel volume). One-dimensional radial heat transfer is assumed at the axial centre of each of these segments. The axial segments are thermally coupled only through the calculated coolant temperatures. Axial heat conduction, as well as mechanical coupling between axial segments, is not considered. However, released fission gas is accumulated over the segments, and the sum of the release in each segment is used to calculate plenum pressure. Thermal expansion and gas pressure inside the fuel pin are then used to compute the strains and stresses in the cladding. For each segment, the following calculations are performed: coolant temperature; cladding surface temperature; fuel/cladding heat transfer coefficient; fuel temperature; fuel constituent redistribution; fission gas generated and released; and fuel and cladding displacements due to swelling and thermal expansion. For each time increment, the fission gas release is updated, the plenum pressure is computed and the fuel temperatures are adjusted to account for the changing gap conductance. Figure 2.8 shows the MACSIS flowchart.

Figure 2.8. MACSIS flowchart

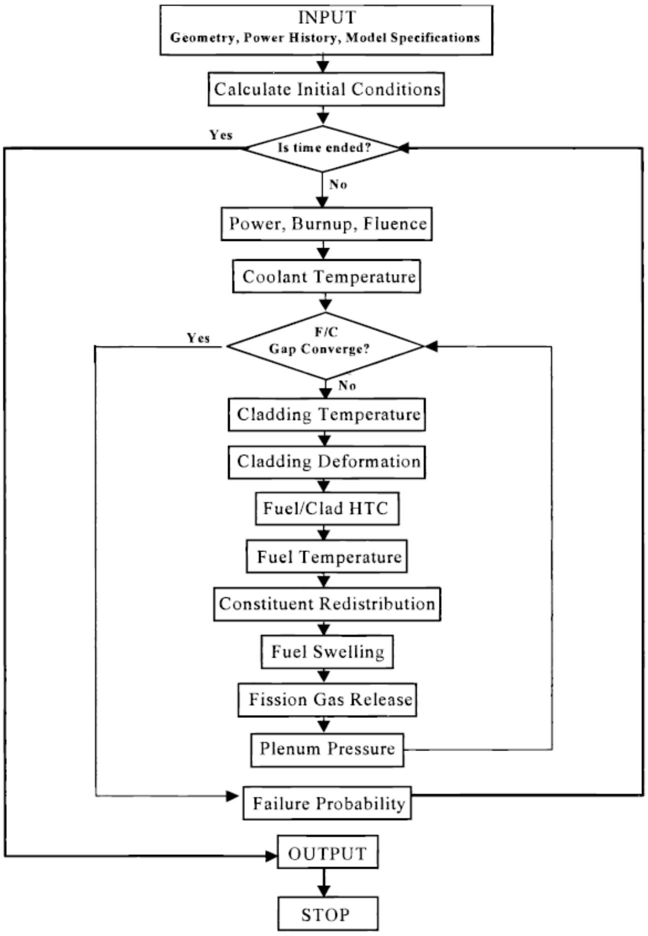

Source: Hwang et al., 1998.

MACSIS code consists of a driver routine, input/output routines, mathematical models and a physically based theoretical model for fission gas release as well as a correlated model for fuel swelling. The mathematical models are heat transfer, gas pressure, and, to a certain extent, dimensional change of fuel and cladding.

To evaluate the predictive capability of MACSIS, the calculation results of fuel constituent redistribution, temperature prediction, fission gas release and cladding strain were compared with the experimental results. For the comparison of models for fuel constituent redistribution and the fuel temperature profile with the experimental data, the DP-11 pin, which was irradiated at the EBR-II by the Argonne National Laboratory, was used (Hofman, Hayes and Petri, 1996; Yacout, 1996a). Figure 2.9 shows the radial distribution of zirconium as a function of elapsed time for the DP-11 pin. As shown in Figure 2.9, the calculated zirconium concentration agrees well with the experimental data at end of life (EOL).

Figure 2.10 shows the fuel temperature distributions at the EOL of the DP-11 pin. The calculated temperature profiles by MACSIS are in good agreement with Yacout et al.’s data (Yacout, 1996a) when assuming that only the outermost (α+γ) region is logged by bond sodium. Figure 2.11 shows the fission gas release fraction according to the burnup variation, predicted by the semi-theoretical models in MACSIS. The predictions by the semi-theoretical model in the code show comparatively good agreement with the experimental results from the ANL (Hofmann and Walters, 1994; Hofmann, Walters and Bauer, 1997; Yacout, 1996a). Figure 2.12 shows the comparison of the cladding strains predicted by MACSIS with the measured strain data of the U-10Zr/HT9 fuel pin (Yacout, 1996b). The diametrical strains predicted by MACSIS seem to agree well with the trend. The foregoing comparisons show that MACSIS is capable of efficiently simulating the in-reactor behaviour of metallic fuel.

Figure 2.9. Radial distribution of zirconium as a function of elapsed time for the DP-11 pin

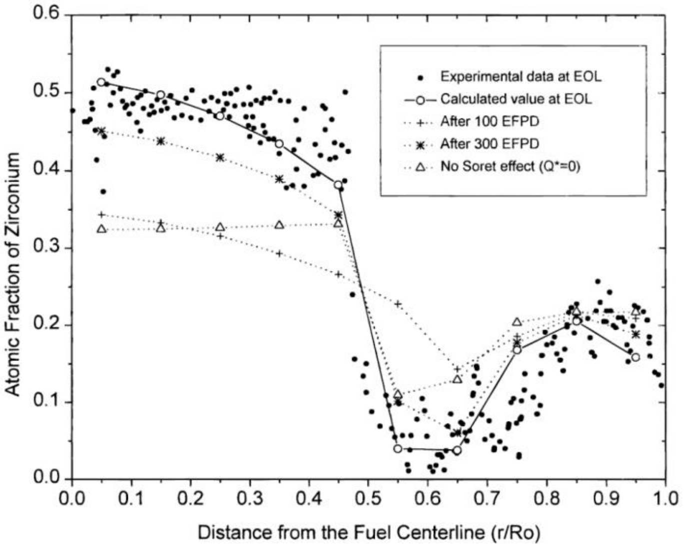

Note: EOL: end of life; EFPD: effective full power day.
Source: Hwang et al., 1998.

Figure 2.10. Fuel temperature distributions at the end of life of the DP-11 pin

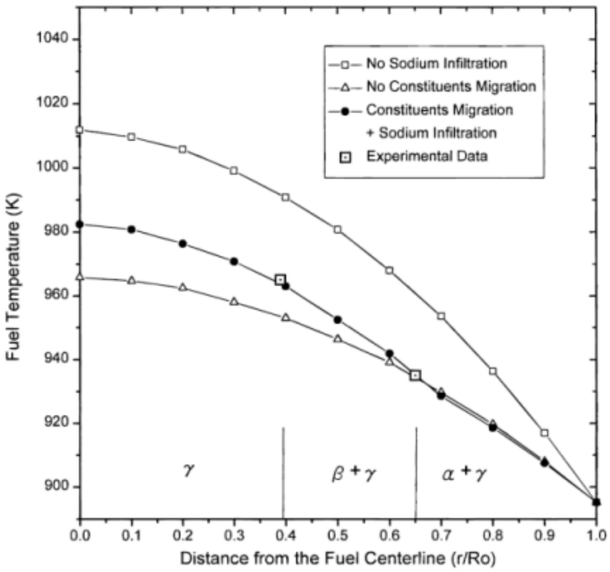

Source: Hwang et al., 1998.

Figure 2.11. Comparison between fission gas release measurements and those calculated by MACSIS

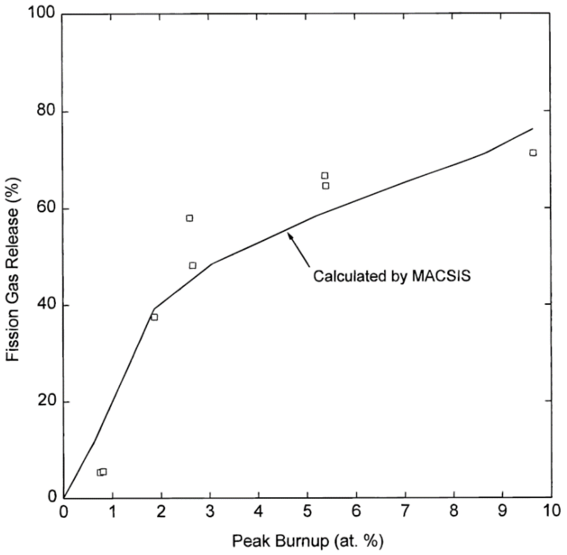

Source: Hwang et al., 1998.

Figure 2.12. Comparison of fuel clad strain between measured data and MACSIS prediction

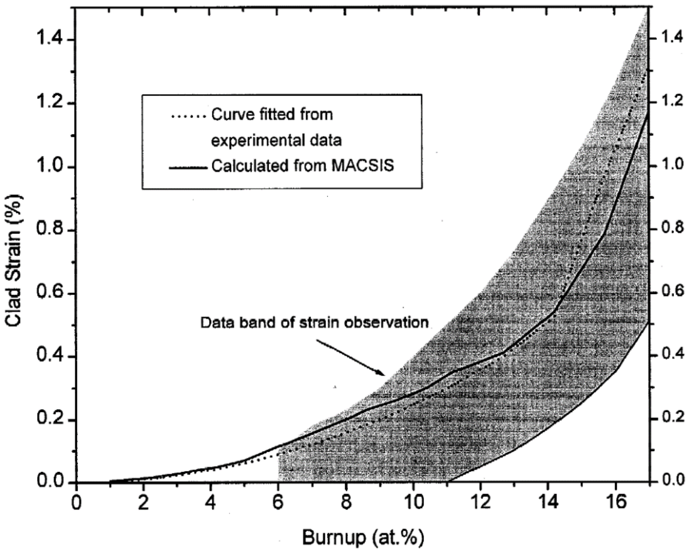

Source: Hwang et al., 1998.

2.2.2. ALFUS (Central Research Institute of Electric Power Industry)

Introduction and history

A metal fuel irradiation behaviour analysis code, ALFUS (ALloyed Fuel Unified Simulator) (Ogata and Yokoo, 1999; Ogata, Kim and Yacout, 2012), was developed by the CRIEPI for examining life-controlling factors of U-Pu-Zr metal fuel. The irradiation phenomena that are modelled in the ALFUS code are shown with blue-coloured text in Figure 2.13, which summarises major irradiation phenomena in fast reactor metal fuel. To reasonably reproduce the fuel-cladding mechanical interaction (FCMI), ALFUS contains some key models for metal fuel slugs, such as an open pore formation model that is consistent with a fission gas behaviour model and stress-strain analysis model, a hot press model to describe open pore volume decrease, and a crack model to treat anisotropic swelling. Although a fuel constituent migration model is also incorporated into ALFUS, it is not actually activated because the mechanical property data of U-Pu-Zr fuel alloys are not sufficient enough for the mechanical properties, such as creep strain rate, to be correlated with fuel alloy composition.

Figure 2.13. Phenomena modelled in ALFUS

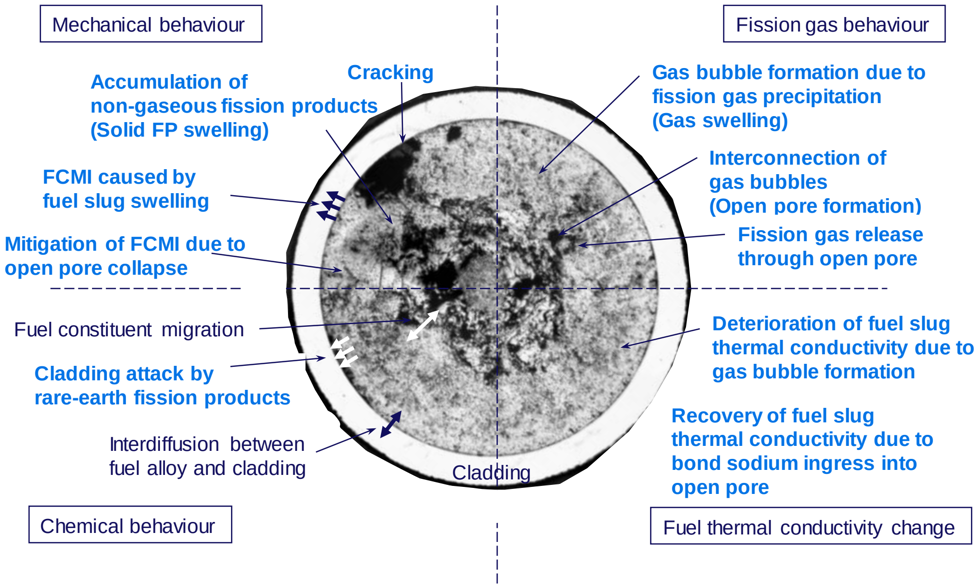

Note: FCMI: fuel-cladding mechanical interaction.
Source: NEA EGIF data, 2019.

Before ALFUS was developed, another metal fuel irradiation behaviour analysis code, SESAME (Kobayashi et al., 1990), was developed and used for understanding anisotropic swelling of binary U-Zr fuel slugs in relatively low burnup. The SESAME code was not capable of simulating highly anisotropic swelling of ternary U-Pu-Zr fuel slugs because no model of radial crack, which is characteristic of U-Pu-Zr fuel slugs, was installed in SESAME. For the ALFUS code, an empirical model to incorporate the effect of large radial crack formed in U-Pu-Zr fuel slugs has been developed and installed. ALFUS can appropriately simulate highly anisotropic swelling of U-Pu-Zr fuel slugs and FCMI behaviour at high burnup.

Brief description of the methods used, validation and capabilities[5]

The ALFUS code includes the following analytical models:

- an r-z 2D stress-strain analysis model based on a finite element method, including gas bubble compressibility and open pore volume decrease (treated as “hot press”);

---

[5] Based on Ogata, Kim and Yacout (2012).

- a mechanistic model to describe fission gas behaviour, such as coalescence and growth of the gas bubbles, formation of the open pores and fission gas release;
- an empirical model to incorporate the effect of large radial crack formed in U-Pu-Zr ternary fuel slugs;
- a model to calculate the volume increase of the fuel alloy matrix due to an accumulation of non-gaseous fission products (solid fission product swelling);
- an empirical correlation to estimate the cladding wastage by rare earth fission products;
- a temperature analysis model with effective thermal conductivity of the swollen, porous fuel slug infiltrated by the bond sodium.

Figure 2.14 illustrates the calculation flow in the ALFUS code (Ogata, Kim and Yacout, 2012). The parameters in the models have been adjusted so that ALFUS can consistently reproduce the irradiation performance data, such as burnup dependence of fission gas release and Pu-content dependence of fuel slug axial elongation, of U-Pu-Zr test fuel pins irradiated in the EBR-II. ALFUS has been validated with the data of the EBR-II irradiation test assemblies: X245 and X441, in terms of FCMI-related data such as axial distribution of cladding diametral change and history of maximum cladding diametral change up to 20 at.% burnup (Ogata, Kim and Yacout, 2012).

Figure 2.14. Calculation flow in ALFUS

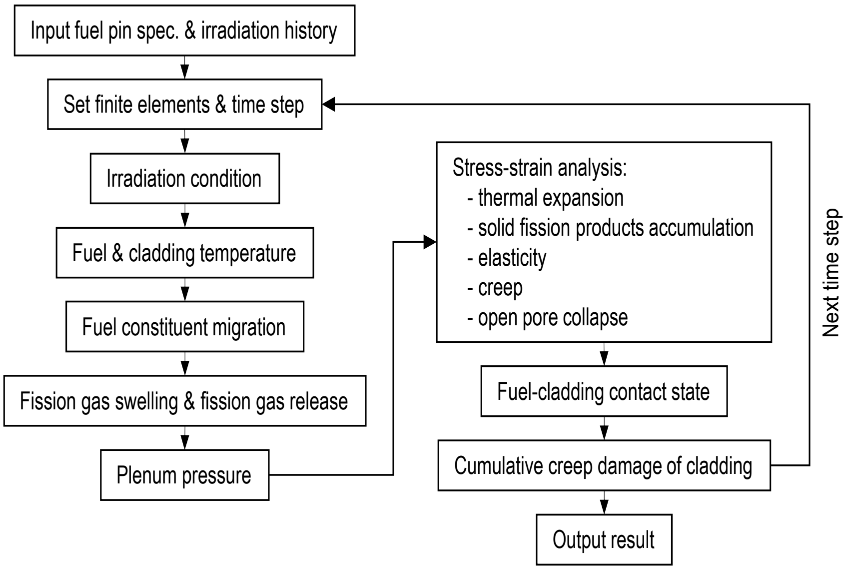

Source: NEA EGIF data, 2019.

2.3. Summary and comparison of code capabilities

Table 2.3 summarises the main characteristics of each code described in this chapter.

Table 2.3. Summary of code characteristics

	Fuel performance codes for oxide fuel				Fuel performance code for metal fuel – sodium-cooled fast reactor	
	GERMINAL	TRANSURANUS	CEPTAR	FEMAXI-FBR	MACSIS	ALFUS
Modelling dimension	1.5D	1.5D	1.5D	1.5D	1.5D	2D
Meshing						
– fuel axial	50	60	20	100	20	20
– fuel radial	50	50	50	100	10	10
– clad radial	20	10	6	3	1	10
MODELS						
Thermal-hydraulics conditions						
– Fixed clad temperature	X	X	X	X	X	
– Convection between Na and clad						
– Na flux+ equivalent Na channel	X	X	X	X	X	X
Thermal behaviour						
– Heat conduction in fuel pellet		X				
– Fuel melting	X	X	X	X	X	X
– Axial transfer of melt fuel	X			X		
– Fuel/clad heat transfer:						
– heat conduction in gap	X	X	X	X	X	X
– heat conduction in JOG	X		X		n/a	n/a
– radiation	X	X	X	X	X	n/a
– solid-solid contact	X	X	X	X	X	n/a
– Heat conduction in clad	X	X	X	X	X	X
Pellet mechanical behaviour						
– Swelling (solid, gaseous)	X	X	X	X	X	X
– Creep	X	X	X	X	X	X
– Densification	X	X	X	X		X
– Thermal expansion	X	X	X	X	X	X
– Cracking/healing		X	X			X

Table 2.3. Summary of code characteristics (Continued)

	Fuel performance codes for oxide fuel				Fuel performance code for metal fuel – sodium-cooled fast reactor	
	GERMINAL	TRANSURANUS	CEPTAR	FEMAXI-FBR	MACSIS	ALFUS
– Pellet fragment relocation (gap closure)	X	X	X	X	n/a	n/a
– swelling	X	X	X	X	X	X
– creep	X	X	X	X	X	X
– thermal expansion	X	X	X	X	X	X
– FCMI	X	X	X	X	X	X
– corrosion	X	X	X	X	X	X
Physico-chemistry						
– Fission gas release	X	X	X	X	X	X
– Fission gas retention as a function of radial position	X	X	X	X	X	X
– U, Pu, MA redistribution	X	X	X	X	U,Pu	
– Oxygen-to-metal ratio evolution in burnup	X	X			n/a	n/a
– Fuel restructuring for oxide (central hole, columnar grain)	X	X	X	X	n/a	n/a
– Fuel restructuring for metal (Zr redistribution)	n/a	n/a	n/a	n/a	X	
– Na logging	n/a	n/a	n/a	n/a	X	X
– JOG formation	X	n/a	X		n/a	n/a
REACTOR OPERATING CONDITIONS						
– Nominal	X	X	X	X	X	X
– Loss of flow (LOF)	X	X	X			X
– Power ramp (control rod withdrawal)	X	X	X	X		X
– Transient over power (TOP)	X	X	X	X		X

Table 2.3. Summary of code characteristics (Continued)

	Fuel performance codes for oxide fuel				Fuel performance code for metal fuel – sodium-cooled fast reactor	
	GERMINAL	TRANSURANUS	CEPTAR	FEMAXI-FBR	MACSIS	ALFUS
VALIDATION						
– Number of pins for validation cases	100	35	108	16	43	6
– Area of validation (see sections dedicated to each code)	Nominal, Power ramp, TOP		Nominal and power ramp	Nominal, power ramp and TOP	Nominal	Nominal
FUEL PROPERTIES	AGT 010101 (1990)	JRC (2019)	Ozawa and Abe (2006)	Okawa et al., 2015)	See Hofman and Walters (1994); Hofman et al. (1996); Hofman et al. (1997); Yacout et al. (1996a); Yacout et al. (1996b)	Ogata et al. (1999); Ogata et al. (2012)

Note: JOG: joint oxyde gaine; FCMI: fuel-cladding mechanical reaction.

References

Ackermann, R.J., R.L. Faircloth and M.H. Rand (1966), “A thermodynamic study of the vaporization behavior of the substoichiometric plutonium dioxide phase”, *Journal of Physical Chemistry*, Vol. 70/11, pp. 3698-3706, https://doi.org/10.1021/j100883a055.

AGT 010101 (1990), “Catalogue européen des propriétés de l’oxyde mixte (U, Pu)O2”, Fast Reactor Data Manual, issue 1, CEA Technical Note CEA SPU/LPCA n°02.

Blanc, V., V. Dupont, T. Beck, T. Lambert, E. Thebaud, F. Charollais, M. Pelletier, A. Bouloré, J.-C. Dumas and B. Michel (2017), “Fuel melting margin assessment of fast reactor oxide fuel pin using a statistical approach”, IAEA-CN-245-333, FR17, June, Yekaterinburg, Russian Federation.

Botazzoli, P., L. Luzzi, S. Brémier, A. Schubert, P. Van Uffelen, C.T. Walker, W. Haeck and W. Goll (2011), “Extension and validation of the TRANSURANUS burn-up model for helium production in high burn-up LWR fuels”, *Journal of Nuclear Materials*, Vol. 419/1-3, pp. 329-338, https://doi.org/10.1016/j.jnucmat.2011.05.040.

Bouineau, V., M. Lainet, A. Courcelle and M. Pelletier (2011), “Toward an improved GERMINAL V2 code to model oxide fuel for SFR”, SMiRT 21, November, New Delhi.

Carlson, N.N., C. Unal and J.D. Galloway (2013), “Formulation of the constituent distribution model implemented into the BISON framework for the analysis of performance of metallic fuels with some initial simulation results”, Technical Report LA-UR-13-26824, Los Alamos National Laboratory, https://doi.org/10.2172/1091811.

Chantoin, P., J.A. Turnbull and W. Wiesenack (1997), “How good is fuel modelling at extended burn-up?”, *Nuclear Engineering International*, Vol. 32.

Cheon, J.S., J.H. Kim, B.O. Lee and C.B. Lee (2013), “PUMA development through a multiphysics approach”, *Transactions of the Korean Nuclear Society Spring Meeting*, Gwangju, Korea, 30-31 May 2013, www.kns.org/files/pre_paper/2/13S-04C-6A-%EC%B2%9C%EC%A7%84%EC%8B%9D.pdf.

Di Marcello, V., P. Botazzoli, A. Schubert and P. Van Uffelen (2011), "Improvements of the TRANSURANUS code for FBR fuel performance analysis", IAEA Technical Meeting on "Design, Manufacturing and Irradiation Behaviour of Fast Reactors Fuels", Obninsk, Russian Federation, 30 May-3 June 2011, IAEA-TECDOC-CD-1689.

Di Marcello, V., V. Rondinello, A. Schubert, J. van de Laar and P. Van Uffelen (2014a), "Modelling actinide redistribution in mixed oxide fuel for sodium fast reactors", *Progress in Nuclear Energy*, Vol. 72, pp. 83-90, https://doi.org/10.1016/j.pnucene.2013.10.008.

Di Marcello, V., A. Schubert, J. van de Laar and P. Van Uffelen (2014b), "The TRANSURANUS mechanical model for large strain analysis", *Nuclear Engineering and Design*, Vol. 276, pp. 19-29, https://doi.org/10.1016/j.nucengdes.2014.04.041.

Di Marcello, V., A. Schubert, J. van de Laar and P. Van Uffelen (2012), "Extension of the TRANSURANUS plutonium redistribution model for fast reactor performance analysis", *Nuclear Engineering and Design*, Vol. 248, pp. 149-155, https://doi.org/10.1016/j.nucengdes.2012.03.037.

Gaston, D., C. Newman, G. Hansen and D. Lebrun-Grandié (2009), "MOOSE: A parallel computational framework for coupled systems of nonlinear equations", *Nuclear Engineering and Design*, Vol. 239/10, pp. 1768-1778, https://doi.org/10.1016/j.nucengdes.2009.05.021.

Győri, Cs., Z. Hózer, K. Lassmann, A. Schubert, J. van de Laar, B. Hatala and M. Cvan (2004), "Extension of Transuranus code applicability with niobium containing cladding models (EXTRA)", Final Report, EVOL-EXTRA-D5/FIKS-CT2001-00173.

Hales, J.D., R.L. Williamson, S.R. Novascone, D.M. Perez, B.W. Spencer and G. Pastore (2013), "Multidimensional multiphysics simulation of TRISO particle fuel", *Journal of Nuclear Materials*, Vol. 443/1-3, pp. 531-543, https://doi.org/10.1016/j.jnucmat.2013.07.070.

Hales, J.D., M.R. Tonks, F.N. Gleicher, B.W. Spencer, S.R. Novascone, R.L. Williamson, G. Pastore and D.M. Perez (2015), "Advanced 39ultiphysics coupling for LWR fuel performance analysis", *Annals of Nuclear Energy*, Vol. 84, pp. 98-110, https://doi.org/10.1016/j.anucene.2014.11.003.

Hofman, G.L. and L.C. Walters (1994), "Metallic fast reactor fuels", *Materials Science and Technology*, Vol. 10A.

Hofman, G.L., L.C. Walters and T.H. Bauer (1997), "Metallic fast reactor fuels", *Progress in Nuclear Energy*, Vol. 31/1-2, pp. 83-110, https://doi.org/10.1016/0149-1970(96)00005-4.

Hofman, G.L., S.L. Hayes and M.C. Petri (1996), "Temperature gradient driven constituent redistribution in U-Zr alloys", *Journal of Nuclear Materials*, Vol. 227/3, pp. 277-286, https://doi.org/10.1016/0022-3115(95)00129-8.

Hwang, W., C. Nam, T.S. Byun and Y.C. Kim (1998), "MACSIS: A metallic fuel performance analysis code for simulating in-reactor behaviour under steady-state conditions", *Nuclear Technology*, Vol. 123/2, pp. 130-141, https://doi.org/10.13182/NT98-A2887.

IAEA (2019), *Fuel Modelling in Accident Conditions (FUMAC)*, IAEA-TECDOC-1889, International Atomic Energy Agency, Vienna, www.iaea.org/publications/13604/fuel-modelling-in-accident-conditions-fumac

IAEA (2013a), *Improvement of Computer Codes Used for Fuel Behaviour Simulation (FUMEX-III)*, IAEA-TECDOC-1697, International Atomic Energy Agency, Vienna, www-pub.iaea.org/MTCD/publications/PDF/TE-1697_CD/PDF/IAEA-TECDOC-1697.pdf.

IAEA (2013b), "In-pile testing and instrumentation for development of generation-IV fuels and materials", Proceedings of a Technical Meeting Held in Halden, Norway, 21-24 August 2012, IAEA-TECDOC-CD-1726, International Atomic Energy Agency, Vienna, www-pub.iaea.org/MTCD/publications/PDF/TE-CD-1726/PDF/IAEA-TECDOC-CD-1726.pdf.

IAEA (2012), *Fuel Modelling at Extended Burnup (FUMEX-II)*, IAEA-TECDOC-1687, International Atomic Energy Agency, Vienna, www.iaea.org/publications/8782/fuel-modelling-at-extended-burnup-fumex-ii.

Ikusawa, Y., T. Ozawa, M. Kato, K. Maeda and M. Kato (2015), "Development and verification of the thermal behavior analysis code for MA containing MOX fuels technical publication", *Volume 1: Plant Operations, Maintenance, Engineering, Modifications, Life Cycle and Balance of Plant; Nuclear Fuel and Materials; Plant Systems, Structures and Components; Codes, Standards, Licensing and Regulatory Issues*, 22nd International Conference on Nuclear Engineering, 7-11 July 2014, Prague, https://doi.org/10.1115/ICONE22-30005.

Inoue, M., K. Abe and I. Sato (2000), "A method for determining an effective porosity correction factor for thermal conductivity in fast reactor uranium-plutonium oxide fuel pellets", *Journal of Nuclear Materials*, Vol. 281/2-3, pp. 117-128, https://doi.org/10.1016/S0022-3115(00)00243-9.

Inoue, M., K. Yamamoto, T. Sekine, M. Osaka, N. Kushida and T. Asaga (2003), "Power-to-melts of uranium-plutonium oxide fuel pins at a beginning-of-life condition in the experimental fast reactor JOYO", *Journal of Nuclear Materials*, Vol. 323/1, pp. 108-122, https://doi.org/10.1016/j.jnucmat.2003.08.030.

Ishizu, T., H. Endo, I. Tatewaki, T. Yamamoto and N. Shirakawa (2012), "Development of integrated core disruptive accident analysis code for FBR", *The Proceedings of the International Conference on Nuclear Engineering (ICONE)*, pp. 826-835.

JRC (2019), *TRASURANUS Handbook*, European Commission.

Kim, J.H., J.S. Cheon, B.O. Lee and C.B. Lee (2014), "Comparison of thermal creep strain calculation results using time hardening and strain hardening rules", *Transactions of the Korean Nuclear Society Spring Meeting*, Jeju, Korea, 29-30 May 2014, www.kns.org/files/pre_paper/31/488%EA%B9%80%EC%A4%80%ED%98%95.pdf.

Knoll, D.A. and D.E. Keyes (2004), "Jacobian-free Newton-Krylov methods: A survey of approaches and applications", *Journal of Computational Physics*, Vol. 193/2, pp. 357-397, https://doi.org/10.1016/j.jcp.2003.08.010.

Kobayashi, T., M. Kinoshita, S. Hattori, T. Ogawa, Y. Tsuboi, M. Ishida, S. Ogawa and H. Saito (1990), "Development of the SESAME metallic fuel performance code", *Nuclear Technology*, Vol. 89/2, pp. 183-193, https://doi.org/10.13182/NT90-A34345.

Lainet, M., V. Bouineau, T. Helfer and M. Pelletier (2013), "Recent modelling improvements in fuel performance code GERMINAL for SFR oxide fuel pins", IAEA-CN-199/241, FR13, March, Paris.

Lainet, M., V. Bouineau, T. Helfer and M. Pelletier (2011), "Recent improvements of mechanical modelling in fuel performance code GERMINAL", MMSNF, September, Aix-en-Provence, France.

Lainet, M., B. Michel, J.-C. Dumas, M. Pelletier and I. Ramière (2019), "GERMINAL, a fuel performance code of the PLEIADES platform to simulate the in-pile behaviour of mixed oxide fuel pins for sodium-cooled fast reactors", *Journal of Nuclear Materials,* Vol. 516, pp. 30-53, https://doi.org/10.1016/j.jnucmat.2018.12.030.

Lainet, M., B. Michel, J.-C. Dumas, K. Samuelsson and M. Pelletier (2017), "Current status and progression of GERMINAL fuel performance code for SFR oxide fuel pins", IAEA-CN-245-222, FR17, June, Yekaterinburg, Russian Federation.

Lassmann, K. (1992), "TRANSURANUS: A fuel rod analysis code ready for use", *Journal of Nuclear Materials*, Vol. 188, pp. 295-302, https://doi.org/10.1016/0022-3115(92)90487-6.

Lassmann, K. (1978), "URANUS – A computer programme for the thermal and mechanical analysis of the fuel rods in a nuclear reactor", *Nuclear Engineering and Design*, Vol. 45/2, pp. 325-342, https://doi.org/10.1016/0029-5493(78)90225-X.

Lassmann, K. and H. Benk (2000), "Numerical algorithms for intragranular fission gas release", *Journal of Nuclear Materials,* Vol. 280/2, pp. 127-135, https://doi.org/10.1016/S0022-3115(00)00044-1.

Lassmann, K. and H. Blank (1988), "Modelling of fuel rod behaviour and recent advances of the transuranus code", *Nuclear Engineering and Design,* Vol. 106/3, pp. 291-313, https://doi.org/10.1016/0029-5493(88)90292-0.

Lassmann, K. and F. Hohlefeld (1987), "The revised URGAP model to describe the gap conductance between fuel and cladding", *Nuclear Engineering and Design,* Vol. 103/2, pp. 215-221, https://doi.org/10.1016/0029-5493(87)90275-5.

Lassmann, K., C. O'Carroll, J. van de Laar and C.T. Walker (1994), "The radial distribution of plutonium in high burnup UO2 fuels", *Journal of Nuclear Materials,* Vol. 208/3, pp. 223-231, https://doi.org/10.1016/0022-3115(94)90331-X.

Lassmann, K., C. Ronchi and G.J. Small (1989), "The development of fuel performance models at the European Institute for Transuranium Elements", *Journal of Nuclear Materials,* Vol. 166/1-2, pp. 112-119, https://doi.org/10.1016/0022-3115(89)90183-9.

Lassmann, K. and J. van de Laar (1998), "The Transient TRANSURANUS version", *Proceedings of IAEA RER/4/019, Licensing Fuel and Fuel Modelling Codes for WWER Reactors, Seminar* "Implementation of the WWER version of the TRANSURANUS code and its application to safety criteria", Sofia, Bulgaria, 7-11 December 1998.

Lassmann, K., C.T. Walker and J. van de Laar (1998), "Extension of the TRANSURANUS burnup model to heavy water reactor conditions", *Journal of Nuclear Materials,* Vol. 255/2-3, pp. 222-233, https://doi.org/10.1016/S0022-3115(98)00019-1.

Lassmann, K., C.T. Walker, J. van de Laar and F. Lindström (1995), "Modelling the high burnup UO2 structure in LWR fuel", *Journal of Nuclear Materials*, Vol. 226/1-2, pp. 1-8, https://doi.org/10.1016/0022-3115(95)00116-6.

Lee, B.O., W.S. Park, Y. Kim and T.Y. Song (2004), "The preliminary performance analysis of the transmutation fuel for HYPER", OECD/NEA 8th Information Exchange Meetings on Actinide and Fission Product Partitioning and Transmutation, Las Vegas, Nevada, 9-11 November 2004.

Marelle, V., P. Goldbronn, C. Introini, S. Bernaud, A. Bouloré, M. Casella, C. Fillaux, J. Julien, K. Mer-Nkonga and L. Noirot (2017), "Validation of PLEIADES/ALCYONE 2.0 fuel performance code", Proceedings of the Water Reactor Fuel Performance Meeting, Jeju, Korea.

Medvedev, P. (2012), "Fuel performance modeling results for representative FCRD irradiation experiments: Projected deformation in the annular AFC-3A U-10Zr fuel pins and comparison to alternative designs", Technical Report INL/EXT-12-27183 Revision 1, Idaho National Laboratory.

Melis, J.C., L. Roche, J.-P. Piron and J. Truffert (1992), "GERMINAL – A computer code for predicting fuel pin behaviour", *Journal of Nuclear Materials*, Vol. 188, pp. 303-307, https://doi.org/10.1016/0022-3115(92)90488-7.

Melis, J.-C., J.-P. Piron and L. Roche (1993), "Fuel modeling at high burn-up: Recent development of the GERMINAL code", *Journal of Nuclear Materials*, Vol. 204, pp. 188-193, https://doi.org/10.1016/0022-3115(93)90216-L.

Michel, B., M. Temmar, M. Lainet, I. Ramière, M. Pelletier and J.-C. Dumas (2017), "3D simulation in the PLEIADES software environment for sodium fast reactor fuel pin behavior under irradiation", IAEA-CN-245-223, FR17, June, Yekaterinburg, Russian Federation.

Misfeldt, I. (1983), "The D-COM blind problem on fission gas release: Experimental description and results: Summary report on OECD-NEA-CSNI/IAEA Specialists' Meeting on Water Reactor Fuel Safety and Fission Product Release in Off-Normal and Accident Conditions", IAEA-IWGFPT/16.

Ogata, T. and T. Yokoo (1999), "Development and validation of ALFUS: An irradiation behavior analysis code for metallic fast reactor fuels", *Nuclear Technology*, Vol. 128/1, pp. 113-123, https://doi.org/10.13182/NT99-A3018.

Ogata, T., Y.S. Kim and A.M. Yacout (2012), "Metal fuel performance Modelling and simulation", In: Konings, R.J.M. (ed.), *Comprehensive Nuclear Materials*, Vol. 3, pp. 713-753, Elsevier, Amsterdam, https://doi.org/10.1016/B978-0-08-056033-5.00075-6.

Okawa, T., I. Tatewaki, T. Ishizu, H. Endo, Y. Tsuboi and H. Saitou (2015), "Fuel behavior analysis code FEMAXI-FBR development and validation for core disruptive accident", *Progress in Nuclear Energy*, Vol. 82, pp. 80-85, https://doi.org/10.1016/j.pnucene.2014.11.002.

Olander, D.R. (1976), "Fundamental aspects of nuclear reactor fuel elements", TID-26711-P1, Energy Research and Development Administration, pp. 155-160.

Ozawa, T. and T. Abe (2006), "Development and verifications of fast reactor fuel design code CEPTAR", *Nuclear Technology*, Vol. 156/1, pp. 39-55, https://doi.org/10.13182/NT156-39.

Ozawa, T. et al. (2015), "Fuel restructuring behavior analysis of MA-bearing MOX fuels irradiated in a fast reactor", ANS Winter Meeting.

Pastore, G., L. Luzzi, V. Di Marcello and P. Van Uffelen (2013), "Physics-based modelling of fission gas swelling and release in UO2 applied to integral fuel rod analysis", *Nuclear Engineering and Design*, Vol. 256, pp. 75-86, https://doi.org/10.1016/j.nucengdes.2012.12.002.

Roche, L. and M. Pelletier (1999), "Modelling of the thermomechanical and physical processes in FR fuel pins using the GERMINAL code", IAEA-SM-358/25.

Schubert, A., P. Van Uffelen, J. van de Laar, C.T. Walker and W. Haeck (2008), "Extension of the TRANSURANUS burn-up model", *Journal of Nuclear Materials*, Vol. 376/1, pp. 1-10, https://doi.org/10.1016/j.jnucmat.2008.01.006.

Spykman, G., D. Märtens, D. Bour, P. Kock, K. Lassmann, A. Schubert and J. van de Laar (2004), "Implementation of a cladding failure model for a loss of coolant accident (LOCA)-analysis in Transuranus", *Proceedings of Enlarged Halden Programme Group Meeting on*

High Burn-up Fuel Performance, Safety and Reliability, Sandefjord, Norway, 9-14 May 2004.

Sundman, B., U.R. Kattner, M. Palumbo and S.G. Fries (2015), “Open-Calphad – a free thermodynamic software”, *Integrating Materials and Manufacturing Innovation*, Vol. 4, pp. 1-15, https://doi.org/10.1186/s40192-014-0029-1.

Suzuki, M. and H. Saitou (2005), “Light water reactor fuel analysis code FEMAXI-6 (Ver. 1): Detailed structure and user’s manual”, JAEA-Data-Code-2005-003.

Tonks, M.R., D. Gaston, P.C. Millett, D. Andrs and P. Talbot (2012), “An object oriented finite element framework for multiphysics phase field simulations”, *Computational Materials Science*, Vol. 51/1, pp. 20-29, https://doi.org/10.1016/j.commatsci.2011.07.028.

Tsuboi, Y., H. Endo, T. Ishizu, I. Tatewaki, H. Saito and H. Ninokata (2012), “Analysis of fuel pin behavior under slow-ramp type transient overpower condition by using the fuel performance evaluation code ‘FEMAXI-FBR’”, *Journal of Nuclear Science and Technology*, Vol. 49/4, pp. 4975-4987, https://doi.org/10.1080/00223131.2012.669242.

Van Uffelen, P., Cs. Győri, A. Schubert, J. van de Laar, Z. Hózer and G. Spykman (2008), “Extending the application range of a fuel performance code from normal operating to design basis accident conditions”, *Journal of Nuclear Materials*, Vol. 383, 137.

Verpeaux, P., T. Charras and A. Millard (1988), “CASTEM 2000: Une approche moderne du calcul des structures”, *Calcul des structures et intelligence artificielle*, Editions Pluralis, France, www-cast3m.cea.fr.

Williamson, R.L., J.D. Hales, S.R. Novascone, M.R. Tonks, D.R. Gaston, C.J. Permann, D. Andrs and R.C. Martineau (2012), “Multidimensional multiphysics simulation of nuclear fuel behaviour”, *Journal of Nuclear Materials*, Vol. 423/1-3, pp. 149-163, https://doi.org/10.1016/j.jnucmat.2012.01.012.

Yacout, A.M., W.-S. Yang, G.L. Hofman and Y. Orechwa (1996a), “Average irradiation temperature for the analysis of in-pile integral measurements”, *Nuclear Technology*, Vol. 115/1, pp. 61-72, https://doi.org/10.13182/NT96-A35275.

Yacout, A.M., S. Salvatores and Y. Orechwa (1996b), “Degradation analysis estimates of the time-to-failure distribution of irradiated fuel elements”, *Nuclear Technology*, Vol. 113/2, pp. 177-189, https://doi.org/10.13182/NT96-A35187.

3. Irradiation experiments selected for the benchmark

3.1. Oxide fuels

3.1.1. Irradiation AFC-2C (rodlet 3) in ATR (US Department of Energy-Idaho National Laboratory)

The destruction of long-lived MA isotopes generated in irradiated nuclear fuel by transmutation in fast reactors is a goal of the United States Department of Energy's Fuel Cycle Research & Development programme (Hayes et al., 2002; US DOE, 2003). Transmutation of MA would dramatically decrease the volume of material requiring disposal and reduce the longer term radiotoxicity and heat load of high-level waste sent to a geologic repository (Hayes et al., 2002; US DOE, 2003). Transmutation also requires a closed fuel cycle, which may result in rare earth carry over into the recycled fuel. To better understand the fuel performance implications of adding MA and rare earth carry over to a fuel system, the Advanced Fuel Campaign (AFC) experiments examine the performance of fast reactor transmutation fuel in the INL Advanced Test Reactor (ATR). The AFC-2C test explored the performance of MA-MOX fuel (McClellan et al., 2015).

The AFC-2C series was irradiated in the ATR East Flux Trap. Figure 3.1 illustrates the cross-section of the AFC-2C experiment. Each AFC-2C experiment is designed as a miniature fast reactor fuel rod and consists of an oxide fuel, helium bond, cladding material (HT-9 ferritic martensitic steel) and inert gas plenum. It is further encapsulated in a stainless steel capsule that serves as the primary boundary between the ATR primary coolant and the experiment.

Figure 3.1. AFC-2C cross-section with capsule and rodlet (Cd basket not present)

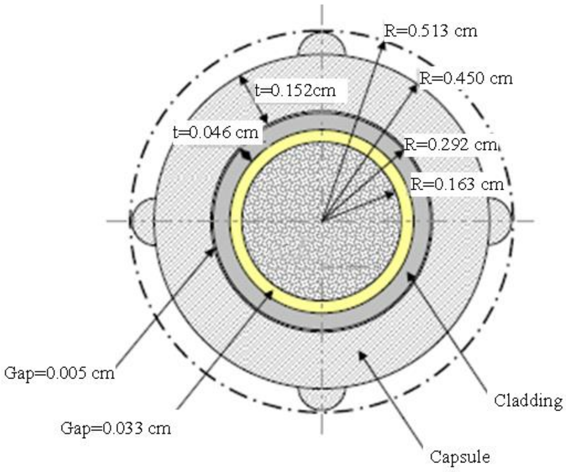

Source: Harp et al., 2018.

The power in the rodlets is driven by the power of the ATR, and the enrichment of the fuel material is tailored to give the programmatically desired linear heat generation rate at the expected ATR power conditions. The gas gap between the rodlet and the capsule is used to control the irradiation temperature in the rodlet given a linear heat generation rate. The fuel material and the cladding material are referred to as the "rodlet" (Figure 3.2 illustrates a schematic description of the AFC-2C rodlet), and the stainless steel capsule is referred to as the “capsule”; one single capsule contains six rodlets. When positioning the experiments in different ATR positions, the capsules are placed in “baskets”. These experiments utilised a Cd-shrouded basket to eliminate thermal neutrons, thus creating a neutron energy spectrum that is closer to a fast reactor spectrum than can normally be achieved in a thermal neutron reactor such as the ATR (Chang and Ambrosek, 2005; Medvedev et al., 2018).

Figure 3.2. Schematic description of the AFC-2C rodlet

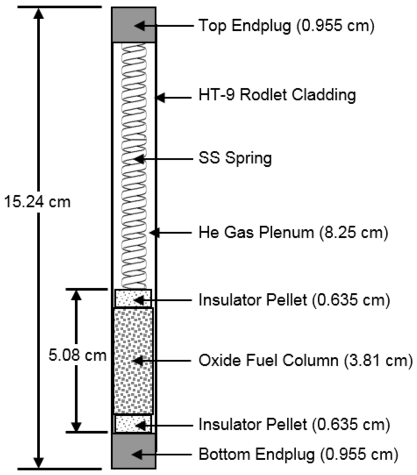

Source: NEA EGIF data, 2019.

For the purpose of the benchmark exercise, rodlet 3 was selected. AFC-2C rodlet 3 has a nominal fuel composition of $U_{0.75}Pu_{0.2}Am_{0.03}Np_{0.02}O_{1.98}$, it was irradiated for 262 effective full power days (EFPD) in the ATR reaching ~8 at.% HM burnup. Figure 3.3 shows the linear heat generation rate (LHGR) profile during irradiation and Table 3.1 reports the experimental design characteristics for fuel, rodlet and capsule and irradiation condition.

Figure 3.3. AFC-2C rodlet 3 linear heat generation rate profile during irradiation

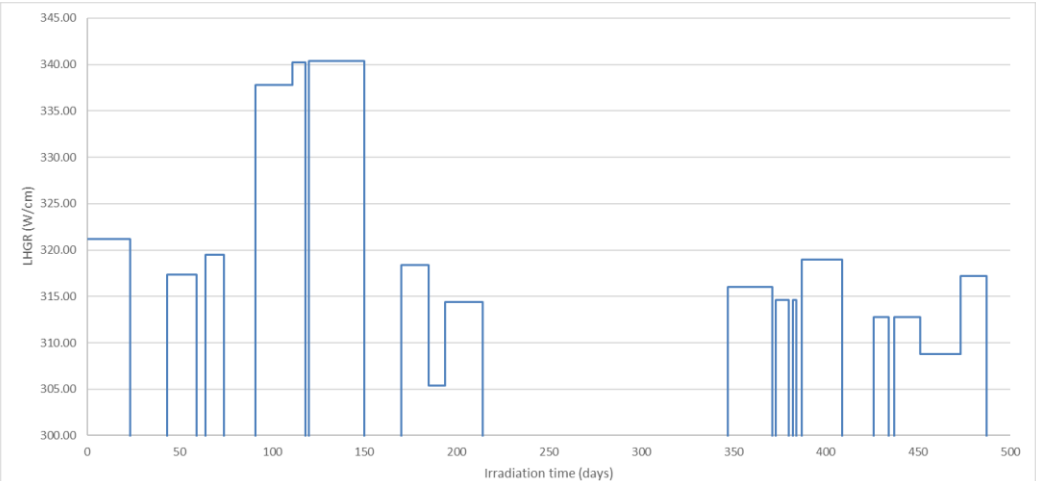

Source: NEA EGIF data, 2019.

Table 3.1. Detailed fuel characteristics and irradiation conditions of the AFC-2C rodlet 3

	Description	Measured/ calculated	Type of measurement/ instrument	AFC-2C rodlet 3 value	Comment
INPUTS					
Reactor irradiation conditions					
Reactor name	ATR				
Irradiation name	AFC-2C rodlet 3				
Power history	Power vs. time plot; linear power (W/cm)	C	MCNP/ORIGEN	320 W/cm	Averaged time linear heat generation rate (LHGR). Cd basket used in experiment hardware approximates fast reactor neutron spectrum but is not exact. The axial flux profile over the 35 mm enriched fuel stack is negligible (see Figure 3.3).
Burnup		C, M	MCNP/ORIGEN	5.5% FIMA	Measured via chemistry of fuel sample. Chemistry results from more recent experiments suggest that the calculated values overpredict burnup by approximately 30%.
Coolant type				Water	Experiment is doubly encapsulated – fuel rodlet is inside a 316L SS capsule. He gas fill between the rodlet and capsule walls. Capsule is in contact with ATR primary coolant (water).
Coolant inlet temperature		M		52°C	Average value.
Coolant pressure		M		250 psi	Average value.
Coolant flow rate		C		1 133.6 cm/s	Average value.
Fuel radial power profile		C	MCNP/ORIGEN	Semi-flat profile	In Cd basket experiment the radial fission power profile is somewhat flat. It goes from 82-85% of nominal power at the centre of fuel to 120-130% of nominal power at the periphery.
Axial power profile		n/a			The axial power profile over the 35 mm enriched fuel stack is negligible.
Equivalent coolant channel diameter (or cladding temperature)		C		n/a	
Final total dose (DPA)		C			DPA has not been calculated.
Fuel element					
Cladding	Cladding is defined by name			HT-9	Database of properties in the code.
Geometry	Pin	M		OD=5.842 mm, ID=4.9276 mm; 9-10 cm plenum length, total pin length (152.4 cm)	
Gap					
Geometry	Defined by experiment	M		90% TD 0.029 mm radial gap	Diametral gap coming from specifications.

Table 3.1. Detailed fuel characteristics and irradiation conditions of the AFC-2C rodlet 3 (Continued)

	Description	Measured/ calculated	Type of measurement/ instrument	AFC-2C rodlet 3 value	Comment
Bond mass		M		n/a	
Plenum gas composition		M	Gas MS	22.1% He remaining Ar	
Plenum gas pressure		M	Transducer	12.4 psi	Assumed, not measured directly.
Upper plenum volume				1.7215 cm^3	
Lower plenum volume				No lower plenum	
Fuel					
Element composition	Defined by experiment	M	ICP-MS	$(U_{0.75},Pu_{0.20},Am_{0.03},Np_{0.02})O_{1.986}$	
Geometry	Defined by experiment	M		0.487 cm diameter 3.797 cm length	
Average grain size	Initial microstructure	M		Not measured	
Average porosity/density	Initial microstructure	M	Immersion	9.700 g/cm^3	Average value.
Surface roughness		M		Not measured	
OUTPUTS					
Temperature	Everywhere, all times	C		~550-560°C	Inner cladding.
Plenum gas pressure		M, C	GASR	740 kPa (at 32°C)	Pressure measured at puncture and expansion into GASR system, plenum volume measured, fission gas pressure calculated.
Plenum gas composition: – total volume – composition (at least He, Xe, Kr)		M	Gas MS	FGR (Xe+Kr): 78% He release: 73%	
Fuel axial growth		M	Neutron radiography	1.4%	
Clad dilation/ deformation/ growth		M, C	Contact profilometry	Max value: 5.889 mm (0.8%)	Length not measured (HT-9 has negligible axial growth), bow not measured.
Axial maximum burnup		M	Isotopic ICP-MS + gamma scan	5.5% FIMA	Flat profile.
Fuel swelling		M	Immersion density, NRAD geometric measurement, microscopy	30%	From optical microscopy, can see that fuel touches cladding.
Fuel clad gap	Size of the gap along the column	M	Radiography (X-ray)	Not measured	
Clad FCCI		M	Microscopy	90-100 µm	Indirect measured by imagine analysis.

Note: FIMA: fissions per initial metal atom; DPA: displacements per atom; OD: outer diameter; ID: inner diameter; GASR: Gas assay, sample and recharge; FCCI: fuel-cladding chemical interaction.

3.1.2. Irradiation B8-HAM in JOYO (Japan Atomic Energy Agency)

The highly Am-containing MOX irradiation experiments, B8-HAM, were performed in JOYO in 1992 to evaluate the irradiation behaviour of Am-MOX (Ozawa, 2017). MOX pellets used for B8-HAM irradiation experiments were originally fabricated for the A1M irradiation experiment, which was a demonstration of Monju fuel irradiation behaviour, and had been stored for seven years. Am content increased up to ~1 wt.% HM during the seven-year storage period. The A1M09 rod was disassembled and MOX pellets were unloaded. All MOX pellets unloaded from A1M09 were degassed, inspected and reassembled as the B8-HAM rod.

Figure 3.4 shows the major specifications and the schema of the B8-HAM rod. The B8-HAM rod had a heterogeneous fuel column with UO_2 and highly Am-containing MOX. The cladding material was advanced austenitic stainless steel, PNC316, with an outer diameter of 6.5 mm. The diameter and density of the Am-MOX pellet was specified as 5.40 mm and 85%T.D., respectively.

Figure 3.4. Major specifications and rod schema of the B8-HAM rod

Item	Specification	
Cladding material	PNC316	
Cladding outer diameter (mm)	6.5	
Cladding inner diameter (mm)	5.56	
Cladding thickness (mm)	0.47	
Fuel pellet type	Solid	
Am-MOX pellet diameter (mm)	5.40	
Am-MOX pellet density (%T.D.)	85	
O/M ratio	1.99	
Pu content (wt.%)	as-fabricated*	28.70
	after irradiation**	27.71
	at SXMA***	27.35
U-235 enrichment (wt.%)	21.5	
Pu-238/Pu-239/Pu-240/Pu-241/Pu-242 (wt.%)	as-fabricated*	0.87/68.13/22.05/5.83/3.12
	after irradiation**	0.76/67.70/23.31/4.98/3.25
	at SXMA***	0.73/68.59/23.62/3.76/3.30
Am-241/Pu (wt.%)	as-fabricated*	3.12
	after irradiation**	3.97
	at SXMA***	5.27
Am-241/HM (wt.%)	as-fabricated*	0.90
	after irradiation**	1.10
	at SXMA***	1.44
UO_2 pellet diameter (mm)	5.40	
UO_2 pellet density (%T.D.)	93	
U-235 enrichment (wt.%)	0.224 (depleted)	
O/U ratio	2.01	

* as-fabricated on 8/5/1991, ** after irradiation on 3/26/1993, *** SXMA on 8/13/1999

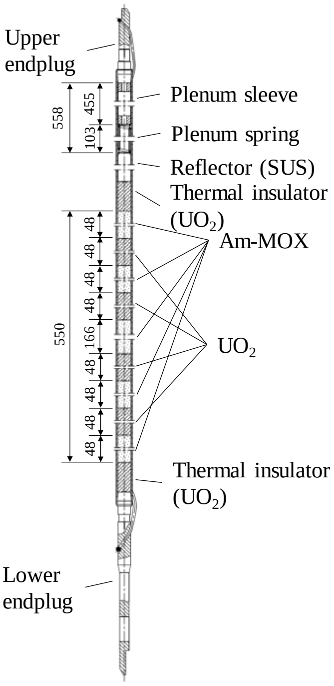

Note: MOX: mixed oxide; O/M: oxygen-to-metal.
Source: Based on Ozawa, 2017.

The B8-HAM rod was loaded into the maximum flux position in PFB080, which was the type B uninstrumented fuel irradiation subassembly (UNIS-B) (JAEA, n.d.), and PFB080 was irradiated at 3F2 in the JOYO core. The irradiation was performed from the 25th to the 27th operation cycle in JOYO in 1992-93. Figure 3.5 shows the history of the reactor thermal power and the maximum linear power of the B8-HAM rod as well as the major irradiation conditions during 25th-27th operation cycles. The irradiation was stable except for a shut-down due to reactor strum during the 27th operation cycle. The B8-HAM rod was irradiated for 134.5 EFPD up to the maximum burnup of 26 GWd/t and the maximum linear power was 386 W/cm at the beginning and 371 W/cm at the end of irradiation.

Figure 3.5. History of reactor thermal power and maximum linear power of the B8-HAM rod, and major irradiation conditions during the 25th-27th operation cycles

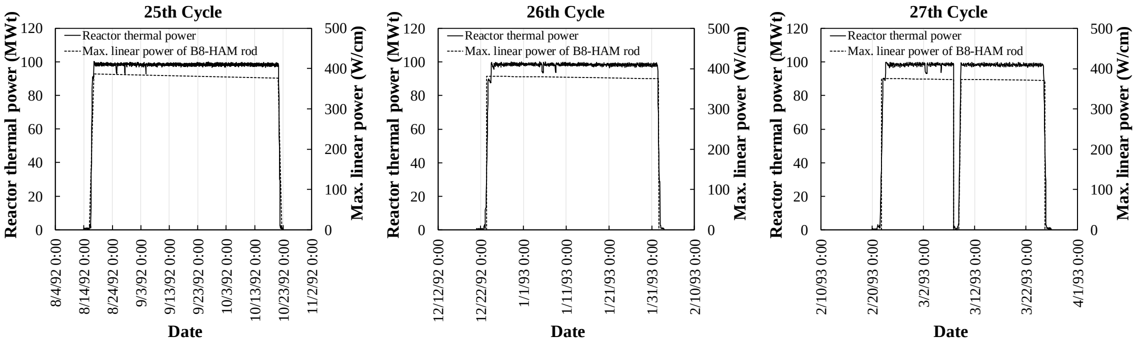

Operation cycle		25	26	27	Total
Duration		8/14/1992- 10/22/1992	12/21/1992- 2/2/1993	2/20/1993- 3/26/1993	
Max. thermal power (MW)		100	100	100	
Operation time (H)		1648.88	1029.25	785.51	3463.64
Effective full power days (EFPD)		64.849	39.513	30.085	134.447
Max. linear power （W/cm)		386-376	382-375	376-371	
Max. neutron flux ($x10^{15}$ n/cm^2/s)	**Total**	3.57	3.62	3.63	
	E>0.1MeV	2.51	2.55	2.55	
Outlet temperature of compartment (ºC)	**BOC**	547	546	545	
	EOC	543	544	543	
Coolant flow rate (kg/s)	**BOC**	0.29	0.29	0.29	
	EOC	0.29	0.29	0.29	

Source: Based on Ozawa, 2017.

Table 3.2 shows the detailed fuel characteristics and irradiation conditions for the benchmark calculations.

Table 3.2. Detailed fuel characteristics and irradiation conditions of B8-HAM

	Description	Measured/ calculated	Type of measurement/ instrument	Value	Comment
INPUTS					
Reactor radiation conditions					
Reactor name	JOYO				
Irradiation name	B8-HAM				
Linear power history (W/cm)		C		Max. 386	
Burnup		C		26 GWd /tHM	
Coolant type				Sodium	Database of properties in the code.
Coolant inlet temp		M		370ºC	
Coolant pressure		M		4.5 bar	The coolant inlet pressure is not directly measured in JOYO, but the discharge pressure of the pump is about 4.50 bar.
Coolant flow rate		C			
Fuel radial power profile	vs. radius	C		Flat	In the fuel not the core, calculated by neutronics code.
Equivalent coolant channel diameter (or cladding temperature)	if cladding temperature vs axial position	C		467.6ºC	Averaged cladding outer temperature.

Table 3.2. Detailed fuel characteristics and irradiation conditions of B8-HAM (Continued)

	Description	Measured/ calculated	Type of measurement/ instrument	Value	Comment
Final total dose (DPA NRT)		C		14.6 dpa 2.9×10^{22} n/cm^2	
Fuel element					
Cladding	Cladding is defined by name			PNC316	Database of properties in the code.
Geometry	Pin	M		OD 6.495 mm, ID 5.559 mm Thickness 0.468 mm	Axially averaged dimensions.
Gap					Important to know if geometry is from specifications or measurements (as-fabricated).
Geometry	Defined by experiment	M		Diametral gap width 150 μm for MOX, 159 μm for UO_2	Axially averaged dimensions.
Plenum gas composition		M	Gas MS	100% He	
Plenum gas pressure		M	Transducer	0.1 MPa	
Upper plenum volume				11.07 cm^3	
Lower plenum volume				0 cm^3	
Fuel					Classically the code is specific for each fuel/reactor. Advanced codes are universal dependent on input parameters + uncertainties.
Element composition	Defined by experiment	M	ICP-MS	$(U_{0.704}, Pu_{0.287}, Am_{0.9})O_{1.99}$	Classic and advanced.
Geometry	Defined by experiment	M		Pellet OD 5.405 mm for MOX, 5.400 mm for UO_2	Classic is code specific; Advanced: mesh is defined for geometry.
Average grain size	Initial microstructure	M/assumed	SEM	4 μm	Classic.
Average porosity/density	Initial microstructure	M	Immersion, SEM	14.43% closed porosity	
Surface roughness		M		1 μm	Cladding inner surface roughness is 0.6 μm.
Density	Material properties	M		85.57% TD for MOX 93.68% TD for UOX	
OUTPUTS					
Temperature	Everywhere, all times	C (M)		–	Not measured.
Plenum gas pressure		M	PIE	0.32396 MPa at cold state	Plenum volume = 10.614 cc.
Plenum gas composition: – total volume – composition (at least He, Xe, Kr)		M	GasMS	Released Xe+Kr 20.05 cm^3 STP Released He 3.27 cm^3 STP He/Kr/Xe:40.9/7.8/ 51.3%	Observed fission product gas release rate 45.3%.
Fuel axial growth		M	NRAD, gamma scan	+6.9 mm	As-fabricated: 354.8 mm PIE: 361.7 mm.
Clad dilation/deformation/ growth	vs. axial position	M, C	Profilometry	Max. 0.4 %ΔD/D	Radially averaged dimensions.

Table 3.2. Detailed fuel characteristics and irradiation conditions of B8-HAM (Continued)

	Description	Measured/ calculated	Type of measurement/ instrument	Value	Comment
Maximum burnup	vs. axial position	M	Isotopic ICP-MS + gamma scan	2.96 at.% (26.1 GWd/tHM)	
Fuel swelling	vs. axial position	M	Immersion density, NRAD geometric measurement, microscopy	Not measured	
Fuel clad gap	vs. axial position	M	Radiography (X-ray)	Not measured	
Clad FCCI		M	Microscopy	No	
Clad FCMI				No	

Note: DPA: displacements per atom; OD: outer diameter; ID: inner diameter; MOX: mixed oxide; SEM: scanning electron microscopy; FCCI: fuel-cladding chemical interaction; FCMI: fuel-cladding mechanical interaction.

3.1.3. Irradiation SUPERFACT (CEA-JRC Karlsruhe)

The SUPERFACT programme (Prunier et al., 1993; Walker and Nicolaou, 1995; Nicolaou et al., 1993) was carried out by JRC Karlsruhe, formerly called ITU, and the CEA during the 1980s. The irradiation was performed in the Phénix reactor (1986-88). The main goal was to demonstrate the technical feasibility of transmutation in fast reactors in a homogeneous approach.

The SUPERFACT irradiation was completed several years after with the TRABANT irradiations in High Flux Reactor (HFR), AM1 in the JOYO fast reactor and AFC-2C and -2D irradiations carried out in the ATR.

Fuel fabrication

The experimental capsule contained:

- 4 MOX pins with pellets containing 2% ^{241}Am or 2% ^{237}Np (homogeneous concept);
- 4 pins UOX with 45% ^{237}Np or 20% ^{241}Am + 20% ^{237}Np (heterogeneous concept).

The fabrication was performed at ITU with the sol-gel process. Figure 3.6 presents the main steps.

Figure 3.6. Fabrication flow sheet for the SUPERFACT fuel at JRC Karlsruhe

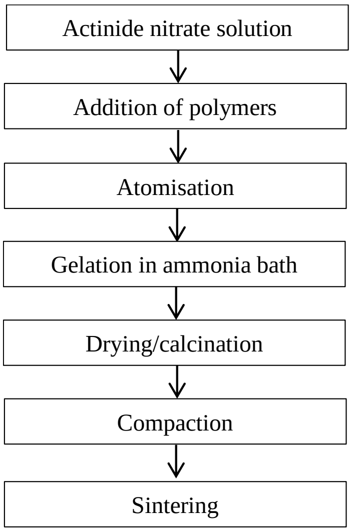

Source: Walker and Nicolaou, 1995.

The process requires the addition of polymers in the initial mixture to increase viscosity. After atomisation, the beads are recovered as a solid in a bath of ammonia. The beads are then washed and dried before being pressed into pellets and sintered at 1 600°C under Ar-5% H_2 for 6 hours. Table 3.3 details the obtained characteristics of the fuel pellets.

Table 3.3. Characteristics of the SUPERFACT fuel pellets

Fuel composition	$(U_{0.74}Pu_{0.24}Np_{0.02})O_2$	$(U_{0.74}Pu_{0.24}Am_{0.02})O_2$	$(U_{0.55}Np_{1.45})O_2$	$(U_{0.6}Np_{0.2}Am_{0.2})O_2$
Pressing	5.1-6.4t/cm^2	4.4-5.6t/cm^2	6.1t/cm^2	6.1t/cm^2
Green density	58.6% TD	58.0% TD	55.6% TD	56.4 TD
Sintering	1620°C/6h Ar 5% H_2	1 620°C/6h Ar 5% H_2	1 620°C/6h Ar 5% H_2	1 620°C/6h Ar 5% H_2
Pellet diameter	5.363±0.052 mm	5.417±0.029 mm	5.418±0.037 mm	5.434±0.013 mm
Pellet density (%T.D.)	97.5±0.8%	96.8±0.7%	95.1±0.6%	95.9±10%
O/M	1.973	1.957	1.996	1.926
Lattice parameter (X-ray diffraction)	5.4578±5Å	5.4570±5Å	5.4545±5Å	5.4735±5Å 5.4696±5Å

Note: TD: theoretical density; O/M: oxygen-to-metal.
Source: Based on Nicolaou et al., 1993.

Irradiation conditions

Table 3.4 gives the irradiation conditions of the fuel pins of the SUPERFACT experiment.

Table 3.4. SUPERFACT fuel pins' irradiation conditions

Fuel	Number of pins	Fissile column length (cm)	Linear power (W/cm)		BU_{max}(at.%)
			Beginning of life	End of life	End of life
$(U,Pu_{0.24},Np_{0.02})O_{1.97}$	2	85	417	345	6.4
$(U,Pu_{0.24},Am_{0.02})O_{1.96}$	2	85	413	345	6.4
$(U,Np_{0.20},Am_{0.02})O_{1.93}$	2	40	174	286	4.1
$(U,Np_{0.45})O_{1.99}$	2	40	197	302	4.56
$(U,Pu_{0.20})O_{2}$	11	85	402	353	7.38

The irradiation conditions of the homogeneous pins (No. 7 and 13 with 2%Np, No. 4 and 16 with 2%Am) are:

- 382 EFPD;
- maximum linear heat rate = 415 W/cm to 345 W/cm;
- burnup = 6.4 at.%.

Main results

The SUPERFACT experiment demonstrated the good in-pile performance of fuels fabricated with the sol-gel technique. The non-destructive examinations of the four pins did not show any anomaly in their behaviour. In particular, no accelerated corrosion was observed.

Figure 3.7. SUPERFACT micrographs

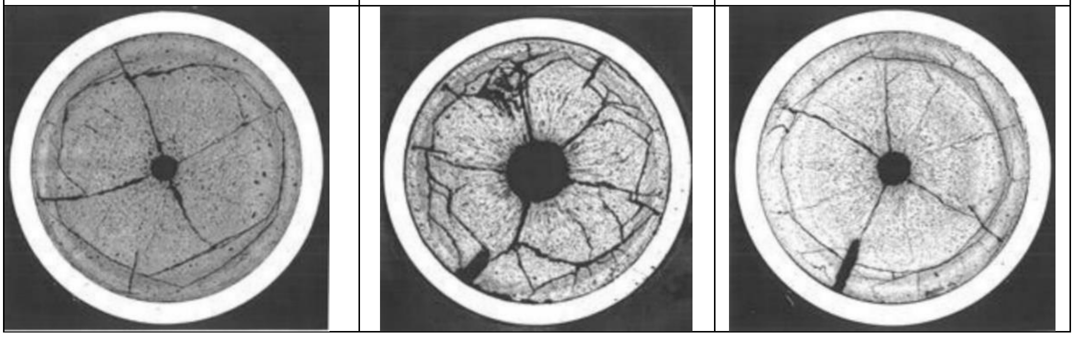

MOX +
2%Am:
380-350 W/cm

Std MOX:
400-350 W/cm

MOX +
2%Np:
385-350 W/cm

Source: Walker and Nicolaou, 1995.

The interpretation of the physicochemical and ceramographic examinations of the fuels (Walker and Nicolaou, 1995; Nicolaou et al., 1993) led to the following conclusions:

- The temperature in pellet was probably higher for the Am-containing fuel.
- The fission gas production and release were as predicted for the operating power.
- The Am pins had a higher helium production, mainly due to the daughter products with high specific alpha activity (e.g. ^{242}Cm and ^{238}Pu). The released helium contributed to increase the internal pressure of the pin. In addition, higher porosities and swelling were found, probably due to the helium still confined in the fuel. A volume of 40 cm^3 of He was released for a fissile column of 85 cm. This can be compared to 10 cm^3 of released He into the standard MOX pins that were simultaneously irradiated (with an equivalent mass of fuel of about 210 g).

- Fuel restructuring is similar to $(U,Pu)O_2$ at the same linear power.
- U, Pu, Am and Np radial distributions are very flat, there were no specific actinide redistributions.
- The corrosion depth was as expected.
- Caesium was found at the end plugs. Its accumulation is probably due to the particularity of the pins with high Am and Np contents (short fuel column).
- The caesium-profiles for the neptunium-containing fuels showed anomalous behaviour of this fission product compared to the other pins.
- The clad diametrical deformation was slightly higher (+0.4 to 0.5%) than for standard pins (+0.3%).

Analyses of the samples of fresh and irradiated SUPERFACT fuels performed by the ITU are in excellent agreement with the observations made at the CEA. The neptunium measurement is difficult (not available at the CEA) and has a higher uncertainty than the measurement of the usual nuclides. The measured extent of transmutation (CEA and ITU) of americium at the maximal flux level is 28% for fuels with low MA content. From neptunium analyses, an average extent of transmutation of 30% was determined for the three samples. Comparison of the measured values with calculations is satisfactory in the case of americium. In the case of neptunium, comparison with calculations showed less agreement for the fuels with low minor actinide content. At intermediate burnup and for low linear power, there is no real influence of the low MA amount in the fuel behaviour except for the He production and release.

Table 3.5. Detailed fuel characteristics and irradiation conditions of SUPERFACT

	Description	Measured/ calculated	Type of measurement/ instrument	SUPERFACT pin 4 value	Comment
INPUTS					
Reactor irradiation conditions				Phénix	
Reactor name	Phénix				
Irradiation name	SUPERFACT pin 4				
Power history	Power vs. time plot; linear power (W/cm)	C		413 W/cm max at BOL 345 W/cm max at EOL	Fabrication time: 1981 BOL: October 86 EOL: August 1988 PIE: 1991.
Coolant type				Na	Database of properties in the code.
Coolant inlet temperature		M		390°C	
Coolant pressure		M		2.2 bar	
Coolant flow rate		C		100 g/s	
Fuel radial power profile		C		Flat	In the fuel not the core, calculated by neutronics code.
Axial power profile					
Equivalent coolant channel diameter (or cladding temperature)		C		1.834 mm	Cladding outer temperature history provided (C).
Final total dose (DPA)		C		52 dpa	
Clad FCMI				No	

Table 3.5. Detailed fuel characteristics and irradiation conditions of SUPERFACT (Continued)

Fuel element				$U_{0.74}Pu_{0.24}Am_{0.0215}O_{1.957}$	
Cladding	Cladding is defined by name			Austenitic steel 15/15 Ti cw	Database of properties in the code.
Geometry	Pin	M		OD=6.55 mm ID=5.65 mm 9.7 cm upper plenum length 77.4 cm lower plenum length 179.3 cm total pin length	
Gap					
Geometry	Defined by experiment	M		116.7 µm	Radial gap.
Bond mass					
Plenum gas composition		M	Gas MS	100% He	
Plenum gas pressure		M	Transducer	1 bar	
Upper plenum volume				1 930 mm^3	
Lower plenum volume				19 530 mm^3	
Fuel					
Element composition	Defined by experiment	M	ICP-MS	$U_{0.74}Pu_{0.24}Am_{0.0215}O_{1.957}$	
Geometry	Defined by experiment	M		Pellet characteristics Cylindrical shape 5.417 mm diameter 7.392 mm height Fissile column height 847.8 mm	
Average grain size	Initial microstructure	M/assumed	SEM	5.9 µm	Classic.
Average porosity/ density	Initial microstructure	M	Immersion, SEM	3.73%/97.0%TD 10.719 g/cm^3	Closed porosity.
Surface roughness		M		2 µm	Oxide fuels.
OUTPUTS					
Temperature	Everywhere, all times	C (M)	In-pile		No thermocouple.
Plenum gas pressure					Not measured.
Plenum gas – composition: total volume – composition (at least He, Xe, Kr)		M	Gas MS	Total volume 217 cm^3 TPN Xe+Kr: 154.61 cm^3 TPN He: 61.29 cm^3 TPN = 21.4 (initial) + 39.89 (released) 60.6% Xe, 10.7% Kr, 28.2% He	Fission gas release: 68% Helium release: 100%.
Fuel axial growth		M	NRAD, gamma scan	854 mm (847.8 mm)	Measured before and after irradiation.
Clad deformation/ growth		M, C	Profilometry	Maximum diametrical deformation +0.47% Total pin length at EOL 179.5 cm	
Burnup		M	Isotopic ICP-MS + gamma scan	6.4 at.% max	ICP-MS at 1 position, use scaling on gamma scan axial profile.
Fuel swelling					Not measured.
Fuel clad gap	Size of the gap along the column	M	Radiography (X-ray)	Diametrical fuel-to-clad gap 21µm at 382 mm/FC bottom 40µm at 625 mm/FC bottom 50µm at 822 mm/FC bottom	For oxides only.
Clad FCCI		M	Microscopy	<50 µm	
Clad FCMI				No	

Note: DPA: displacements per atom; BOL: beginning of life; EOL: end of life; PIE: post-irradiation examination; OD: outer diameter; ID: inner diameter; SEM: scanning electron microscopy; FCCI: fuel-cladding chemical interaction; FCMI: fuel-cladding mechanical interaction.

3.2. Metal fuels

3.2.1. Irradiation AFC-1H (rodlet 4) in the ATR (US Department of Energy-Idaho National Laboratory)

The goal of the United States Department of Energy's Fuel Cycle Research & Development programme is the destruction of long-lived MA isotopes generated in irradiated nuclear fuel by transmutation in fast reactors (Hayes et al., 2002; US DOE, 2003). Transmutation of MA would dramatically decrease the volume of material requiring disposal and reduce the longer term radiotoxicity and heat load of high-level waste sent to a geologic repository (Hayes et al., 2002; US DOE, 2003). Transmutation also requires a closed fuel cycle, which may result in rare earth carry over into the recycled fuel. To better understand the fuel performance implications of adding MA and rare earth carry over to a fuel system, the Advanced Fuel Campaign (AFC) experiments examine the performance of fast reactor transmutation fuel in the INL's ATR. The AFC-1H contained low-fertile (uranium) actinide-bearing metallic alloy fuel compositions.

The AFC-1H series was irradiated in the ATR East Flux Trap. Figure 3.8 illustrates the cross-section of the AFC-1H experiment. Each AFC-1H experiment is designed as a miniature fast reactor fuel rod and consists of a metallic fuel, sodium bond, cladding material (HT-9 ferritic martensitic steel) and an inert gas plenum. It is further encapsulated in a stainless steel capsule that serves as the primary boundary between the ATR primary coolant and the experiment.

Figure 3.8. AFC-1H cross-section with capsule and rodlet (Cd basket not present)

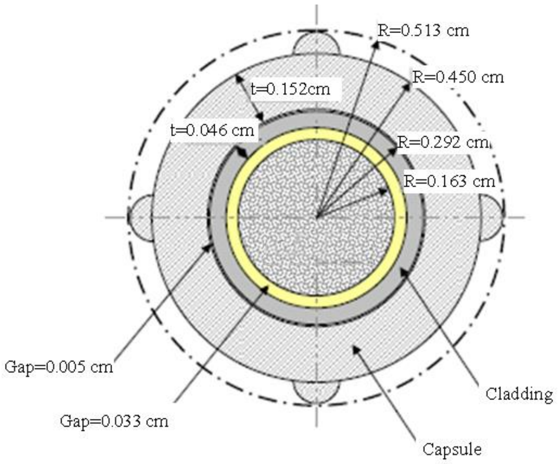

Source: Harp et al., 2018.

The power in the rodlets is driven by the power of the ATR, and the enrichment of the fuel material is tailored to give the programmatically desired linear heat generation rate at the expected ATR power conditions. The gas gap between the rodlet and the capsule is used to control the irradiation temperature in the rodlet given a linear heat generation rate. The fuel material and the cladding material are referred to as the "rodlet" (Figure 3.9 illustrates a schematic description of the AFC-1H rodlet), and the stainless steel capsule is referred to as the "capsule"; one single capsule contains six rodlets. When positioning the experiments in different ATR positions, the capsules are placed in "baskets". These experiments used a Cd-shrouded basket to eliminate thermal neutrons thus creating a neutron energy spectrum that is closer to a fast reactor spectrum than can normally be achieved in a thermal neutron reactor such as the ATR (Chang and Ambrosek, 2005; Medvedev et al., 2018; Harp et al., 2017).

Figure 3.9. Schematic description of the AFC-1H rodlet

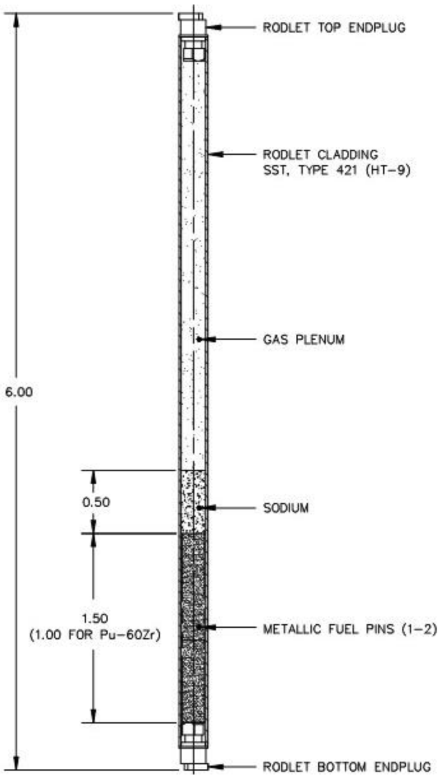

Source: Harp et al., 2017.

Rodlet 4 was selected for the benchmark exercise. The AFC-1H rodlet 4 has a nominal fuel composition of 35U-29Pu-4Am-2Np-30Zr; it was irradiated for 248 EFPD in the ATR reaching ~26 at.% heavy metal (HM) burnup. Figure 3.10 shows the LHGR profile during irradiation and Table 3.6 reports the fuel design characteristics and irradiation condition.

Figure 3.10. AFC-1H rodlet 4 linear heat generation rate profile during irradiation

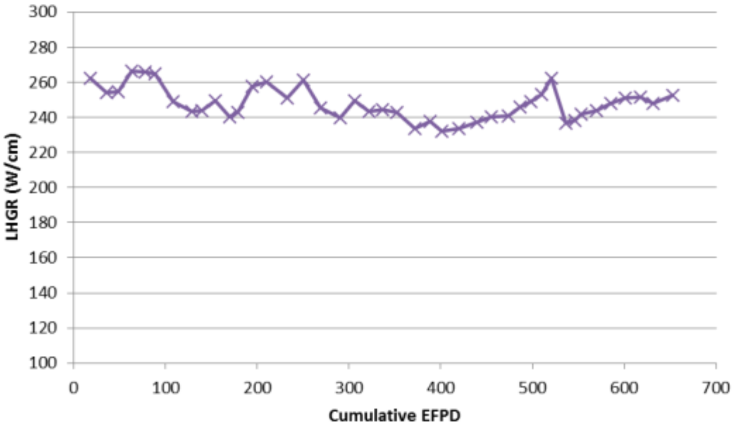

Note: LHGR: linear heat generation rate; EFPD: effective full power days.
Source: NEA EGIF data, 2019.

Table 3.6. Detailed fuel characteristics and irradiation conditions of the AFC-1H-rodlet 4

	Description	Measured/ calculated	Type of measurement/ instrument	Level of difficulty/ uncertainty	AFC-1H rodlet 4	Comment
INPUTS						
Reactor irradiation conditions						
Reactor name	ATR					
Irradiation name	AFC-1H Rodlet 4					
Power history	Power vs. time plot; linear power (W/cm)	C	MCNP/ORIGEN	1	248 W/cm (time averaged)	Time averaged linear heat generation rate (see Figure 3.10). Cd basket used in experiment hardware approximates fast reactor neutron spectrum but it is not exact. The axial flux profile over the 1.5-in. fuel slug is negligible.
Burnup		C, M	MCNP/ORIGEN		20.5 at.% HM (measured)	Measured via mass spectrometry of the fuel sample.
Coolant type					Water	Experiment is doubly encapsulated – fuel rodlet is inside a 316L SS capsule. He gas fill between rodlet and capsule walls. Capsule is in contact with ATR primary coolant (water).
Coolant inlet temperature		M		1	52°C	Average value.
Coolant pressure		M		1	1 720 kPa	Average value.
Coolant flow rate		C			1133.6 cm/s	Average value.
Fuel radial power profile		C	MCNP/ORIGEN		Semi-flat profile	In the Cd basket experiment, the radial fission power profile is somewhat flat. It goes from 82-85% of nominal power at the centre of fuel to 120-130% of nominal power at the periphery.
Axial power profile		n/a				The axial power profile over the 1.5-in. fuel slug is negligible.
Equivalent coolant channel (or cladding temperature)		C			n/a	
Final total dose (DPA)		C				DPA has not been calculated.
Fuel element						
Cladding	Cladding is defined by name				HT-9	Database of properties in the code.
Geometry	Pin	M		1	OD=5.842 mm ID=4.9276 mm; 9-10 cm plenum length, total pin length (152.4 cm)	

Table 3.6. Detailed fuel characteristics and irradiation conditions of the AFC-1H-rodlet 4 (Continued)

	Description	Measured/ calculated	Type of measurement/ instrument	Level of difficulty/ uncertainty	AFC-1H rodlet 4	Comment
Gap						
Geometry	Defined by experiment	M		1	65% smeared density	
Bond mass		M			0.406 g	
Plenum gas composition		M	Gas MS	1	22.1% He remainder Ar	
Plenum gas pressure		M	Transducer	1	12.4 psi	Assumed, not measured directly.
Upper plenum volume					1.7215 cm^3	Calculated from drawings.
Lower plenum volume					No lower plenum	
Fuel						Classically the code is specific for each fuel/reactor. Advanced codes are universal dependent on input parameters.
Element composition	Defined by experiment	M	ICP-MS	1	U-29Pu-4Am-2Np-30Zr	Specified in as-built chemistry tab.
Geometry	Defined by experiment	M		1	0.397 cm diameter 3.718 cm length	
Average grain size	Initial microstructure	M/assumed	SEM	2	As-cast 10-50 µm	
Average porosity/ density	Initial microstructure	M	Immersion, SEM	1	11.525 g/cm^3	Calculated from geometry and mass.
Surface roughness		M			Not measured	
Diffusion coefficients	Material properties	M		2	Not measured	As input or calculated down to phase, etc.
OUTPUTS						
Temperature	Everywhere, all times	C		3	~480-500°C	Inner cladding.
Plenum gas pressure		M, C	GASR	1	1 592 kPa	Pressure measured at puncture and expansion into GASR system, plenum volume measured, fission gas pressure calculated.
Plenum gas composition: – total volume – composition (at least He, Xe, Kr) – isotopic composition		M	Gas MS	1	FGR (Xe+Kr): 77.8% He release: 73%	
Fuel axial growth		M	Neutron radiography	1	13%	Initial fuel slug length: 3.718 cm Final fuel slug length: 4.2 cm.
Clad dilation/ deformation/ growth		M, C	Contact profilometry	1		Cladding diameter provided in profilometry tab, length not measured (HT-9 has negligible axial growth), bow not measured.
Maximum burnup		M	Isotopic ICP-MS + gamma scan	1	26.68 at.% HM	

Table 3.6. Detailed fuel characteristics and irradiation conditions of the AFC-1H-rodlet 4 (Continued)

	Description	Measured/ calculated	Type of measurement/ instrument	Level of difficulty/ uncertainty	AFC-1H rodlet 4	Comment
Fuel swelling		M	Immersion density, NRAD geometric measurement, microscopy	3	~30%	From optical microscopy, can see that fuel touches cladding.
Clad FCCI		M	Microscopy	2	Not measured yet	Not measured yet.
Clad FCMI				3	Not measured	Classic, not directly measured, inferred from profilometry results, is more important for oxide fuels.

Note: DPA: displacements per atom; HM: heavy metal; OD: outer diameter; ID: inner diameter; FCCI: fuel-cladding chemical reaction; FCMI: fuel-cladding mechanical reaction.

3.2.2. Irradiation X501 in EBR-II (US Department of Energy-Idaho National Laboratory)

The Fuel Cycle Research & Development programme seeks to develop and demonstrate the technologies needed to transmute long-lived transuranic actinide isotopes contained in spent nuclear fuel into shorter lived fission products. Transmutation would dramatically decrease the volume of material requiring disposal and the longer term radiotoxicity and heat load of high-level waste sent to a geologic repository (US DOE, 2003).

The X501 fuel experiments were irradiated in the EBR-II at the former Argonne National Laboratory West (ANL-W), now the INL. Irradiation of the X501 began in February 1993 (cycle 163) and was completed in August 1994 (cycle 170) for 339 EFPD, reaching 7.6 at.% of peak burnup (Meyer et al., 2008; 2009).

The EBR-II fast reactor fuel pin consists of a metallic fuel slug, sodium-bonded, HT-9 cladding and an inert gas plenum. The subassembly (named X501) was irradiated at the centre of EBR-II reactor core (Figure 3.11) and was composed of 59 driver pins of U-10Zr and 2 minor actinides bearing metallic fuel of composition U-20.2Pu-9.1Zr-1.3Np-1.2Am. The main characteristics of the fuel pin and the irradiation conditions are reported in Table 3.7; other details for the fuel fabrication are described Trybus et al. (1993).

Figure 3.11. X501 experiment location in the EBR-II

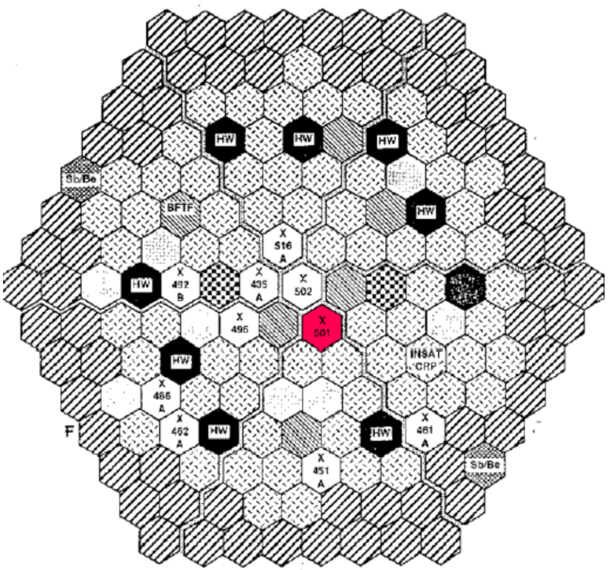

Source: Meyer et al., 2008.

Table 3.7. Detailed fuel characteristics and irradiation conditions of the EBR-II-X501-G582

	Description	Measured/ calculated	Type of measurement/ instrument	Level of difficulty/ uncertainty	X501	Comment
INPUTS						
Reactor irradiation conditions						
Reactor name	EBR-II					
Irradiation name	X501					
Power history	Power vs. time plot; linear power (W/cm)	C		1	45 kW/m max.	
Burnup		C, M	MCNP/ORIGEN			
Coolant type					Na	Database of properties in the code.
Coolant inlet temperature		M		1		
Coolant pressure		M		1		
Coolant flow rate		C				Coolant velocity.
Fuel radial power profile		C	MCNP/ORIGEN			In the fuel not the core, calculated by neutronics code.
Axial power profile		n/a				
Equivalent coolant channel diameter (or cladding temperature)		C				
Final total dose (DPA)		C				
Fuel element						
Cladding	Cladding is defined by name				HT-9	Database of properties in the code.

Table 3.7. Detailed fuel characteristics and irradiation conditions of the EBR-II-X501-G582 (Continued)

	Description	Measured/ calculated	Type of measurement/ instrument	Level of difficulty/ uncertainty	X501	Comment
Geometry	Pin	M		1	OD= 5.84 mm, ID= 4.93 mm; cm plenum length, 74.9 cm total pin length	
Gap						
Geometry	Defined by experiment	M		1	75% smeared density	
Bond mass		M				
Plenum gas composition		M	Gas MS	1	75He-Ar	
Plenum gas pressure		M	Transducer	1		Assumed, not measured directly.
Upper plenum volume					7.1 cm^3	
Lower plenum volume					No lower plenum	
Fuel						Classically the code is specific for each fuel/reactor. Advanced codes are universal dependent on input parameters.
Element composition	Defined by experiment	M	ICP-MS	1	U-20.2Pu-9.1Zr-1.3Np-1.2Am	
Geometry	Defined by experiment	M		1	0.427 cm diameter 34.3 cm length	
Average grain size	Initial microstructure	M/assumed	SEM	2	As-cast 10-50 µm	
Average porosity/ density	Initial microstructure	M	Immersion, SEM	1	15.7 g/cc	
Surface roughness		M			Not measured	
OUTPUTS						
Temperature	Everywhere, all times	C		3	700°C/540°C	Peak fuel centreline/peak cladding inner surface on.
Plenum gas pressure		M, C	GASR	1	2 448 pKPa	
Plenum gas composition: – total volume – composition (at least He, Xe, Kr)		M	Gas MS	1	Xe+Kr= 79% He= 90%	
Fuel axial growth		M	Neutron radiography	1	2.6%	

Table 3.7. Detailed fuel characteristics and irradiation conditions of the EBR-II-X501-G582 (Continued)

	Description	Measured/ calculated	Type of measurement/ instrument	Level of difficulty/ uncertainty	X501	Comment
Clad dilation/ deformation/growth		M, C	Contact profilometry	1		Cladding diameter provided in profilometry tab, length not measured (HT-9 has negligible axial growth), bow not measured.
Axial maximum burnup		M	REBUS/RCT/ORIGEN	1	7.6% HM	Exact value + axial profile.
Fuel swelling		M	Immersion density, NRAD geometric measurement, microscopy	3	30%	30% after 2-5% burnup (higher Zr content delays swelling effect).
Fuel clad gap	Size of the gap along the column	M	Radiography (X-ray)	1		For oxides only.
Clad FCCI		M	Microscopy	2	0	Not visible FCCI from optical microscope sample.
Clad FCMI				3	n/a	Not measured.

Note: DPA: displacements per atom; OD: outer diameter; ID: inner diameter; FCCI: fuel-cladding chemical reaction; FCMI: fuel-cladding mechanical reaction.

3.2.3. Irradiation SMIRP-1 in HANARO (Korea Atomic Energy Research Institute)

KAERI performed the fuel irradiation test SMIRP-1 (SFR Metal fuel Irradiation test Program-1) for 182 EFPD from 15 November 2010 to 5 January 2012 in HANARO (High flux Advanced Neutron Application ReactOr) (Cheon et al., 2011; Lee et al., 2016). PIE of the irradiated fuel pins were done at the Irradiated Material Examination Facility (Cheon et al., 2014; Kim et al., 2017). There were 12 fuel pins that consisted of 6 U-10Zr and 6 U-10Zr-5Ce slugs with T92 cladding, and the irradiation rig accommodated 6 fuel pins at each upper and lower positions, respectively. Among them, four fuel pins had a thin Cr layer which was electroplated on the inner surface of the cladding. Each fuel pin was contained in a sealing tube. There was a gap between the cladding and the sealing tube to attain a temperature jump for the desirable cladding temperature. Table 3.8 summarises the fuel pin design and irradiation condition of SMIRP-1 while Figure 3.12 shows the schematic diagram of the SMIRP-1 fuel pin.

Table 3.8. Fuel pin design and irradiation condition of SMIRP-1

Total irradiation time (EFPD)	182.4

Note: EFPD: effective full power day.

Figure 3.12. Schematic diagram of the SMIRP-1 fuel pin

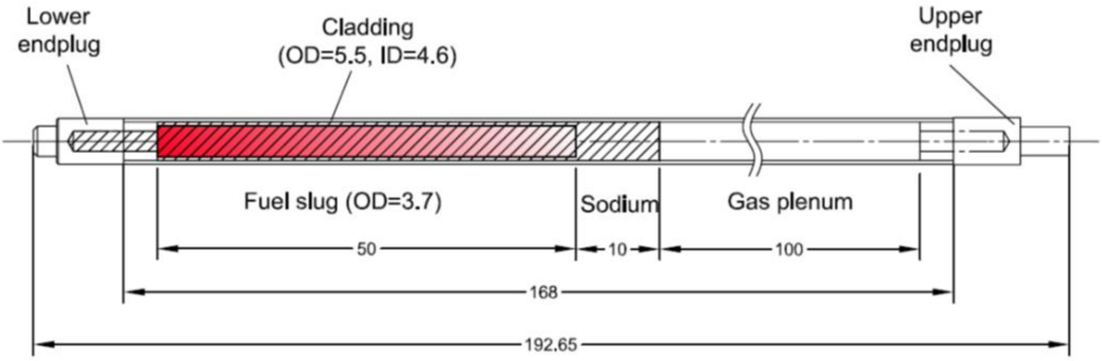

Note: OD: outer diameter; ID: inner diamter.
Source: Cheon et al., 2011.

Figure 3.13 shows the average radial power profile for six fuel pins at the upper position of the irradiation rig. They were closely placed on the same core-plane and had a similar composition. It can be assumed that the variation of radial power profile over irradiation time is negligible. The maximum average linear power and burnup for the six fuel pins at the upper position of the irradiation rig were 245.1 W/cm at the beginning of the test and 2.44 at.% at the end of the test according to an as-run analysis (Figure 3.14). Using the fuel performance analysis code MACSIS, the maximum cladding inner wall temperature and fuel centreline temperature were calculated to be 452°C and 549°C, respectively. Therefore, phase of fuel slugs were irradiated in the $\alpha+\delta$ regime as predicted in the U-Zr phase diagram (Hofman, Hayes and Petri, 1996) with respect to time and location (Figure 3.15). Nb-95 and Ru-106 isotopes were employed as measures for the axial distribution of linear power and burnup, respectively (Figures 3.16 and 3.17). Zr concentration profiles were measured across the cross-section of the fuel (Figure 3.18). Zr was observed to move against the temperature gradient. Distribution of Zr showed a maximum at around the fuel centre, gradually decreased along the fuel surface, which has a lower temperature than the fuel centre. Zr migrated towards the higher temperature side, whose behaviour was governed as a Soret effect. In this case, the Soret effect is the sole mechanism for this phenomenon since there was no phase boundary (only $\alpha+\delta$ phase exists) in the fuels. The detailed fuel characteristics and irradiation conditions for U-10Zr/T92 and U-10Zr-5Ce/T92 are shown in Table 3.9.

Figure 3.13. Average radial power profile for six fuel pins at the upper position of the irradiation rig (beginning of life) – SMIRP-1

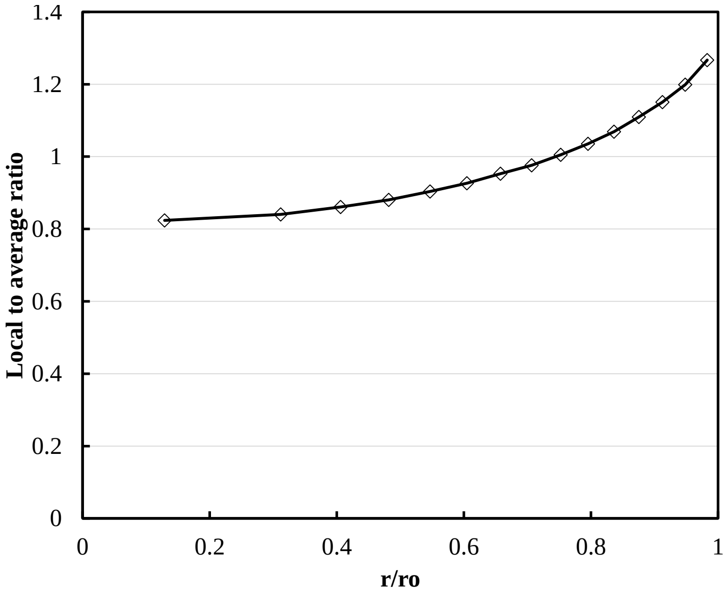

Source: Kim et al., 2017.

Figure 3.14. Average linear power and burnup for six fuel pins at the upper position of the irradiation rig as a function of effective full power days – SMIRP-1

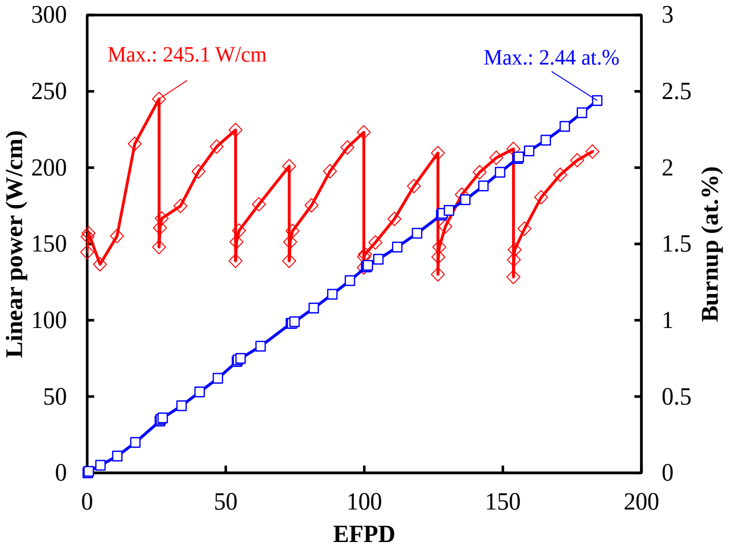

Source: Kim et al., 2017.

Figure3.15. Cladding inner wall temperature and fuel centreline temperature for six fuel pins at the upper position of the irradiation rig as a function of burnup – SMIRP-1

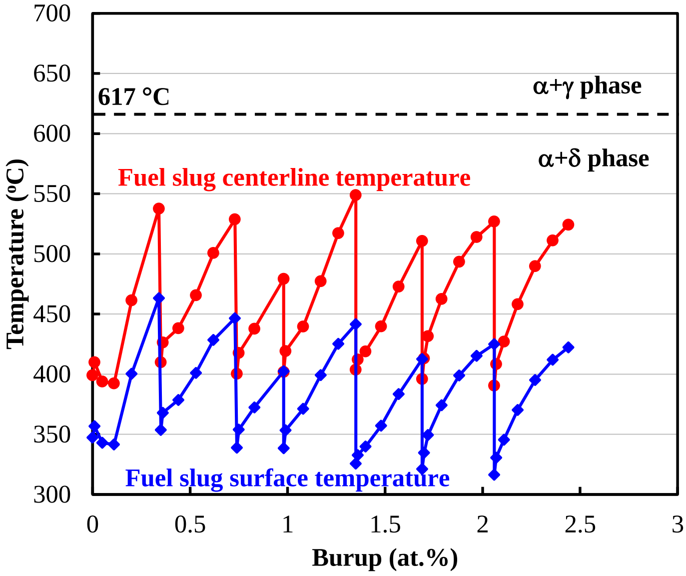

Note: EFPD: effective full power day.
Source: Kim et al., 2017.

Figure 3.16. Relative gamma ray intensity from the bottom of the fuel slug for the fuel pin at the upper position of the irradiation rig (U-10Zr/T92 with Cr barrier) – SMIRP-1

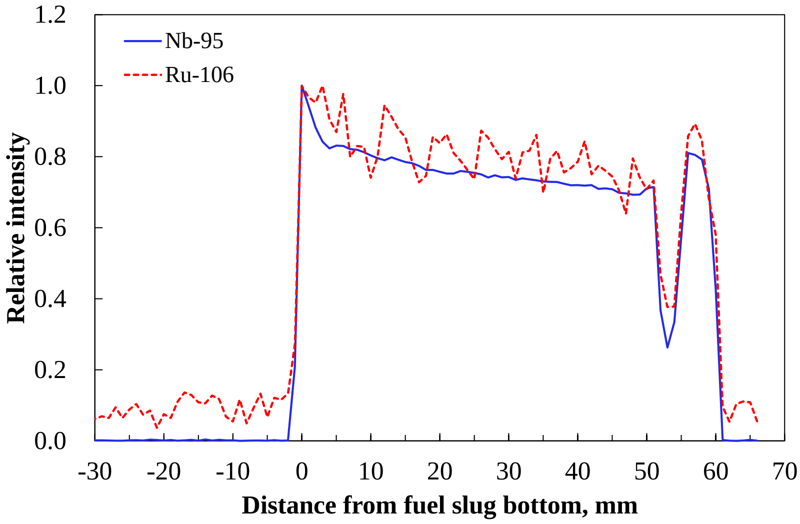

Source: Kim et al., 2017.

Figure 3.17. Relative gamma ray intensity from the bottom of the fuel slug for the fuel pin at the upper position of the irradiation rig (U-10Zr-5Ce/T92 with Cr barrier) – SMIRP-1

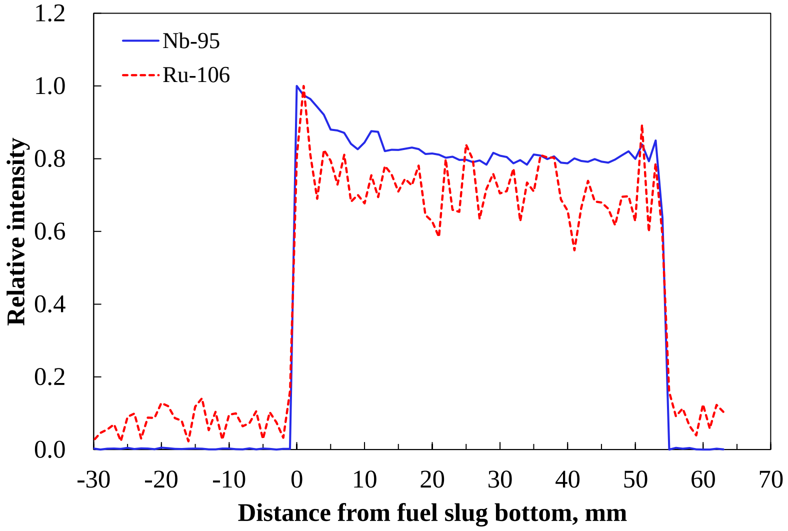

Source: Kim et al., 2017.

Figure 3.18. Zr distribution measurement along the radial direction for the fuel pin at the upper position of the irradiation rig (U-10Zr/T92 with Cr barrier) – SMIRP-1

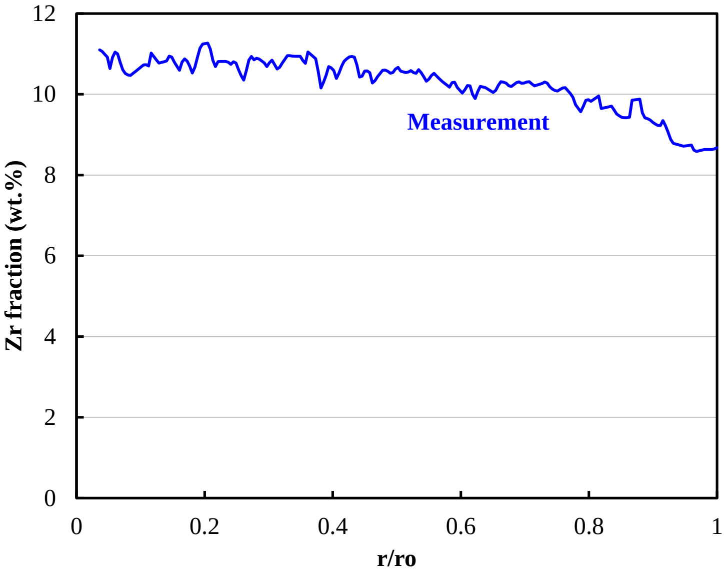

Source: Kim et al., 2017.

Table 3.9. Detailed fuel characteristics and irradiation conditions of U-10Zr/T92 of the SMIRP-1

	Description	Measured/ calculated	Type of measurement/ instrument	Level of difficulty/ uncertainty	Value	Comment
INPUTS						
Reactor irradiation conditions						
Reactor name	HANARO					
Irradiation name	SMIRP-1:U-10Zr, U-10Zr-5Ce					
Power history (W/cm)		C		1	128.3~245.1 (W/cm)	Average linear power for six fuel pins at the upper position of the irradiation rig which were closely placed on the same core-plane and had a similar composition (Figure 3.14).
Burnup		C		1	2.44 at.%	Average burnup for six fuel pins at the upper position of the irradiation rig which were closely placed on the same core-plane and had a similar composition (Figure 3.14).
Coolant type		n/a			Container filled with gas and coolant = water	Cladding is sealed in a container which is exposed to HANARO reactor coolant. He radial gap (0.06 mm) between the capsule and the fuel pin.
Coolant inlet temperature		n/a			n/a	Cladding is sealed in a container which is exposed to HANARO reactor coolant.
Coolant pressure		n/a			n/a	Cladding is sealed in a container which is exposed to HANARO reactor coolant.
Coolant flow rate		n/a			n/a	Cladding is sealed in a container which is exposed to HANARO reactor coolant.
Fuel radial power profile		C			Local to average ratio: 0.82~1.27	Average radial power profile for six fuel pins at the upper position of the irradiation rig which were closely placed on the same core-plane and had a similar composition was calculated only at beginning of life. It can be assumed that the variation of radial power profile over irradiation time is negligible (Figure 3.13).
Axial power profile		M			See comment	Nb-95 and Ru-106 gamma intensities were measured (Figures 3.16 and 3.17).
Equivalent coolant channel diameter (or cladding temperature)	If cladding temperature vs. axial position	n/a			See comment	Cladding is sealed in a container which is exposed to HANARO reactor coolant.

Table 3.9. Detailed fuel characteristics and irradiation conditions of U-10Zr/T92 of the SMIRP-1 (Cont'd)

Final total dose (DPA)		n/a			Not available	HANARO is a thermal reactor.
Fuel element						
Clad	Cladding is defined by name				T92	
Composition		M		1	ASTM-A182	
Geometry	Pin	M		1	OD=5.5 mm, ID=4.6 mm, Gas plenum length=100 mm	
Gap		n/a				Not measured.
Geometry	Defined by experiment	M		1	0.45 mm (diametral gap)	
Bond mass		M		1	0.5 g Na	Total mass of sodium in a fuel pin.
Plenum gas composition		M		1	He	Not measured.
Plenum gas pressure		M	Pressure gauge	1	3 bar	
Upper plenum volume		C			1.66 cc	Calculated from initial gas plenum length at beginning of life.
Lower plenum volume						None.
Fuel						
Element composition	Defined by experiment	M	ICP-MS	1	– U-10Zr: 9.8 wt.%Zr – U-10Zr-5Ce: 11.4 wt.%Zr 5.2 wt.%Ce	- U-10Zr: C(100), H(22), N(10), O(470) in ppm - U-10Zr-5Ce: C(450), H(25), N(40), O(370) in ppm
Isotopic composition	Defined by experiment	M	ICP-MS	1	– U-10Zr: 0.173 U234, 19.551 U235, 0.127 U236 – U-10Zr-5Ce: 0.170 U234, 19.303 U235, 0.126 U236	Unit: wt% U238 balance.
Geometry	Defined by experiment	M		**1**	– U-10Zr: OD=3.60~3.69 mm, L=49.85 mm – U-10Zr-5Ce: OD=3.55~3.68 mm L=49.96 mm	Measured.
Average grain size	Initial microstructure	M				Not measured.
Average porosity	Initial microstructure	C			– U-10Zr porosity: 0.02 – U-10Zr-5Ce porosity: 0.04	Calculated from theoretical and measured density.

Table 3.9. Detailed fuel characteristics and irradiation conditions of U-10Zr/T92 of the SMIRP-1 (Cont'd)

Surface roughness		M				Not measured.
density	Material properties	M		1	– U-10Zr: 15.6 g/cc – U-10Zr-5Ce: 14.3 g/cc	Measured.
OUTPUTS						
Temperature	Everywhere, all times	C	SEM	3	– Cladding inner wall temperature: 316~452°C – Fuel slug centerline temperature: 391~549°C	Figure 3.15.
Plenum volume at STP		C(M)	Gamma scan	1	- U-10Zr: 1.43 cc - U-10Zr-5Ce: 1.31 cc	Calculated from measured fuel axial growth.
Plenum gas composition: – total volume – composition (at least He, Xe, Kr)		M	GasMS	1	Total volume – U-10Zr: 2.47 cc (STP) – U-10Zr-5Ce: 2.15 cc (STP) Composition – U-10Zr: 85.6Xe-14.4Kr – U-10Zr-5Ce: 85.1Xe-14.9Kr	
Fuel axial growth		M	Gamma scan	1	– U-10Zr: 10~12% – U-10Zr-5Ce: 6~8%	
Clad dilation/ deformation/ growth	vs. axial position	M				Not measured.
Axial burnup	vs. axial position	M	Gamma scan	1	See comment	Gamma scan was performed along axial direction. (Nb-95 and Ru-106) (Figures 3.16 and 3.17).
Fuel swelling	vs. axial position	M	OM and SEM	1	31%	Gap between fuel slug and cladding was closed along fuel axis.
Fuel clad gap	vs. axial position	M	OM and SEM	1	None	Gap between fuel slug and cladding was closed along fuel axis.
Clad FCCI		M	OM, SEM and EPMA	2	0	No FCCI due to Cr barrier between fuel and cladding.
Clad FCMI		M		2		Not measured.
Fuel constituent redistribution		M	EPMA/SEM	2		Figure 3.18.

Note: DPA: displacements per atom; OD: outer diameter; ID: inner diameter; FCCI: fuel-cladding chemical reaction; FCMI: fuel-cladding mechanical reaction; OM: optical microscopy; SEM: scanning electron microscopy; EPMA: electron probe microanalysis.

3.2.4. Irradiation METAPHIX-2 in Phénix (Central Research Institute of Electric Power Industry)

The METAPHIX programme (Ohta et al., 2015; 2016) is a collaborative programme between CRIEPI and the European Commission JRC Karlsruhe to understand the irradiation behaviour of fast reactor metal fuel containing MA (Np, Am, Cm) and demonstrate the MA transmutation performance in fast reactors. Metal fuel pins that include U-Pu-Zr-MA alloys were fabricated at the JRC-Institute for Transuranium Elements (JRC-ITU, currently JRC Karlsruhe) and irradiated in the Phénix fast reactor up to three different burnups, approximately 2.5at.% (METAPHIX-1), 7at.% (METAPHIX-2) and 10at.% (METAPHIX-3), with the support of the French CEA.

Since the MA recovered pyrometallurgically from spent fuels entrain comparable amounts of rare earth fission products due to their chemical affinities, the effect of the contamination of MA with rare earth elements (REs) should be examined. The characterisation of U-Pu-Zr alloys containing MA and REs indicated that practically homogeneous fuel alloys can be prepared provided that the total content of the REs is limited to 5wt% or less. Based on this characterisation result, three MA-bearing fuel alloys, U-19Pu-10Zr-2MA-2RE, U-19Pu-10Zr-5MA-5RE and U-19Pu-10Zr-5MA (wt%), were selected along with a standard ternary fuel alloy, U-19Pu-10Zr, for the irradiation experiment. In the METAPHIX programme, Np, Am and Cm were used as MA, and Y, Ce, Nd and Gd as REs.

Three metal fuel pins, two of which include MA-containing alloy segments of 100 mm length in the U-19Pu-10Zr fuel stacks, were fabricated. The total length of the active fuel was 485 mm. The cladding material was 15-15Ti austenitic steel and the fuel-cladding gap was filled with sodium for thermal bonding. A schematic view of metal fuel pins No. 1, 2 and 3, compared with that of the oxide driver fuel pin, is shown in Figure 3.19. These metal fuel pins were arranged in an irradiation capsule along with 16 oxide fuel driver pins for irradiation in the Phénix fast reactor as shown in Figure 3.20. Three irradiation capsules with identical configurations were prepared to achieve different target burnups.

PIEs were performed at JRC Karlsruhe. Non-destructive tests such as cladding profilometry and axial gamma ray spectrometry were completed on all the irradiated METAPHIX fuel pins, which showed no appreciable change in the irradiation behaviour of the metal fuels caused by the addition of up to 5 wt% MA and REs. Destructive examinations including plenum gas analysis, optical microscopy, scanning electron microscopy and electron probe microanalysis have also been performed for the ~2.5 at.% and ~7.0 at.% burnup fuels. Chemical analysis using inductively coupled plasma-mass spectrometry was also performed.

Figure 3.19. Schematic view of metal fuel pins irradiated in the METAPHIX programme

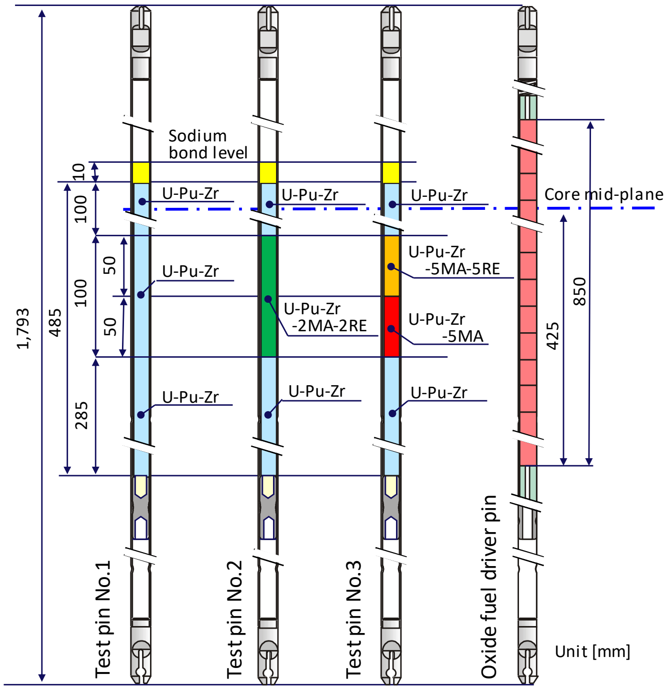

Source: NEA EGIF data, 2019.

Figure 3.20. Metal fuel pin arrangement in the irradiation capsule of the Phénix reactor

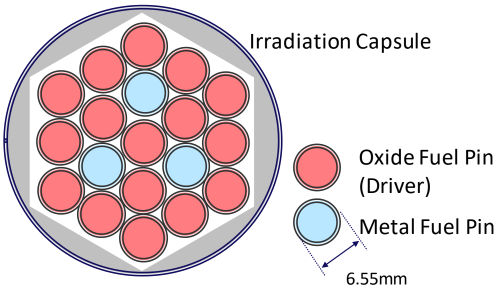

Source: NEA EGIF data, 2019.

Figure 3.21. Average linear power as a function of effective full power days

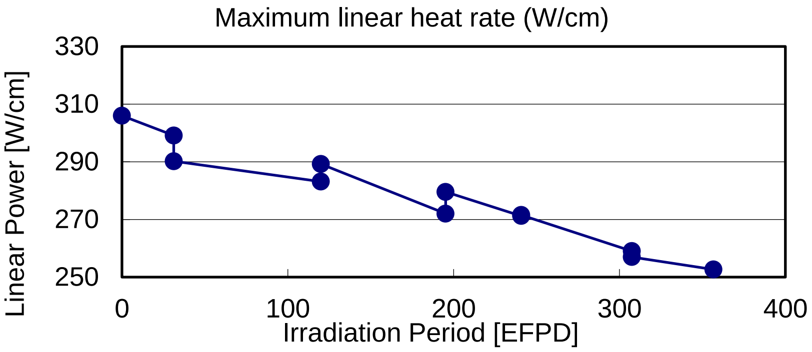

Source: NEA EGIF data, 2019.

Table 3.10. Detailed fuel characteristics and irradiation conditions of METAPHIX-2

	Description	Measured/ calculated	Type of measurement/ instrument	METAPHIX-2	Comment
INPUTS					
Reactor irradiation conditions					
Reactor name	Phénix				
Irradiation name	METAPHIX-2 #3				
Power history	Power vs. time plot; linear power (W/cm)	C		253-306 W/cm (METAPHIX-2)	
Burnup				~7 at.%	
Coolant type				Na	
Coolant inlet temperature		M		376-383°C	
Coolant pressure		M		~0.1 MPa	
Coolant flow rate		C		69 g/s/pin	Estimated value.
Fuel radial power profile		C		Flat	
Axial power profile					
Equivalent coolant channel diameter (or cladding temperature)					
Final total dose (DPA)		C		48 DPA (METAPHIX-2)	
Fuel element (as-fabricated)					
Cladding	Cladding is defined by name			15-15 Ti	
Geometry	Pin	M		Cladding: OD=6.55 mm, ID=5.65 mm; total pin length=179.3 cm	
Gap					
Geometry	Defined by experiment	M		75.2% smeared density diametral gap=650 μm	
Bond mass		M			
Plenum gas composition		M	Gas MS	He	100%
Plenum gas pressure		M	Pin puncture	0.1 MPa	Initial value
Upper plenum volume					
Lower plenum volume				None	
Fuel					
Element composition	Defined by experiment	M		U-Pu-Zr-5RE-5MA/U-Pu-Zr-5MA	
Isotopic composition	Defined by experiment	M	ICP-MS		
Geometry	Defined by experiment	M		Cylinder, 4.9 mm diameter fuel stack length=48.5 cm	
Average grain size	Initial microstructure	M/assumed	SEM		
Average porosity/ density	Initial microstructure	M	Immersion, SEM	~100%TD (15.8 g/cm^3: U-Pu-Zr)	
Surface roughness		M		n/a	
Density	Material properties	M		15.80 g/cm^3:U-Pu-Zr 15.32 g/cm^3:U-Pu-Zr-5MA 14.67 g/cm^3:U-Pu-Zr-5MA-5RE	Open literature

Table 3.10. Detailed fuel characteristics and irradiation conditions of METAPHIX-2 (Continued)

	Description	Measured/ calculated	Type of measurement/ instrument	METAPHIX-2	Comment
OUTPUTS (code + PIE)					
Temperature	Everywhere, all times	C	In-pile	400-550°C F-C, 500-650°C centre (calculation)	
Plenum gas pressure		M	Pin puncture	1.7 MPa	
Plenum gas composition: – total volume – composition (at least He, Xe, Kr)		M	Gas MS	Kr 6.23% and Xe 80.84%, He 12.9%	
Fuel axial growth		M	Gamma scan	3.5 % (total)	
Clad dilatation/ deformation/growth		M, C	Profilometry	0.319%	
Maximum burnup		M, C	Isotopic ICP-MS + gamma scan	U-Pu-Zr-5MA: 5.7-6.9 at.% at ~305 mm (measured), 6.6 at.% at ~405 mm (calculated, peak)	
Fuel swelling	Precise the axial position, at least peak power node and top of fissile column	M	Immersion density, gamma scan, microscopy	35-40%	Estimated from fuel axial growth and smear density (closed F/C gap).
Fuel clad gap	Size of the gap along the column	M	Radiography (X-ray)	Zero	Closed F/C gap closed.
Clad FCCI		M	Microscopy		Not measured.
Na logging	Na penetration into porosity	M		~12% of the initial bond Na volume at F/C gap logged into porosity	Estimated from bond Na height 116 mm after irradiation.
Clad FCMI					Classic, not directly measured, inferred from profilometry results, is more important for oxide fuels.
Fuel composition			Isotopic ICP-MS		

Note: DPA: displacements per atom; OD: outer diameter; ID: inner diameter; FCCI: fuel-cladding chemical reaction; FCMI: fuel-cladding mechanical reaction.

References

Chang, G. and R.G. Ambrosek (2005), "Hardening neutron spectrum for advanced actinide transmutation experiments in the ATR", *Radiation Protection Dosimetry*, Vol. 115/1-4, pp. 63-68, http://dx.doi.org/10.1093/rpd/nci167.

Cheon, J.S., K.H. Kim, S.J. Oh, J.H. Kim, C.T. Lee, B.O. Lee and C.B. Lee (2011), "U-Zr SFR fuel irradiation test in HANARO", IAEA Technical Meeting on Design, Manufacturing and Irradiation Behaviour of Fast Reactors Fuels, Russian Federation, 30 May-3 June 2011.

Cheon, J.S. et al. (2014), "Post-irradiation examination on SMIRP-1 fuel rods", *Transactions of the Korean Nuclear Society Spring Meeting*, Jeju, Korea, www.kns.org/files/pre_paper/31/214%EC%B2%9C%EC%A7%84%EC%8B%9D.pdf

Harp, J.M., L. Capriotti, H.J.M. Chichester, P.G. Medvedev, D.L. Porter and S.L. Hayes (2018), "Postirradiation examination on metallic fuel in the AFC-2 irradiation test series", *Journal of Nuclear Materials*, Vol. 509, pp. 454-464, https://doi.org/10.1016/j.jnucmat.2018.07.019.

Harp, J.M., S.L. Hayes, P.G. Medvedev, D.L. Porter and L. Capriotti (2017), "Testing fast reactor fuels in a thermal reactor: A comparison report", INL/EXT-17-41677, http://dx.doi.org/10.2172/1458766.

Hayes, S.L., B.A. Hilton, M.K. Meyer, G.S. Chang, F.W. Ingram, S. Pillon, N. Schmidt, L. Leconte and D. Haas (2002), "US test plans for actinide transmutation fuel development", *Transactions of the American Nuclear Society*, Vol. 87/353.

Hofman, G.L., S.L. Hayes and M.C. Petri (1996), "Temperature gradient driven constituent redistribution in U-Zr alloys", *Journal of Nuclear Materials*, Vol. 227/3, pp. 277-286, https://doi.org/10.1016/0022-3115(95)00129-8.

JAEA (n.d.), "Un-instrumented fuel irradiation subassemblies (offline irradiation rigs)", *Joyo User's Guide*, Japan Atomic Energy Agency, www.jaea.go.jp/04/o-arai/joyo_users_guide/equipment/fuel_bundle/index.html.

Kim, J.H., J.S. Cheon, B.O. Lee, J.H. Kim, H.M. Kim, B.O. Yoo, Y.H. Jung, S.B. Ahn and C.B. Lee (2017), "Measurement of microstructure and eutectic penetration rate on irradiated metallic fuel after high-temperature heating test," *Metals and Materials International*, Vol. 23, pp. 504-511, https://doi.org/10.1007/s12540-017-6515-1.

Lee, C.B., J.S. Cheon, S.H. Kim, J.Y. Park and H.K. Joo (2016), "Metal fuel development and verification for prototype generation IV sodium-cooled fast reactor", *Nuclear Engineering and Technology*, Vol. 48/5, pp. 1096-1108, https://doi.org/10.1016/j.net.2016.08.001.

McClellan, K.J., H.J.M. Chichester, S.L. Hayes and S.L. Voit (2015), "Summary of the minor actinide-bearing MOX AFC-2C and -2D irradiations", Fast Reactors and Related Fuel Cycles: Safe Technologies and Sustainable Scenarios (FR13), COMPANION CD-ROM, *Proceedings of an International Conference*.

Medvedev, P., S. Hayes, S. Bays, S. Novascone and L. Capriotti (2018), "Testing fast reactor fuels in a thermal reactor", *Nuclear Engineering and Design*, Vol. 328, pp. 154-160, https://doi.org/10.1016/j.nucengdes.2017.12.034.

Meyer, M.K. et al. (2009), "The EBR-II X501 Minor Actinides Burning Experiment", *Journal of Nuclear Materials*, Vol. 392/2, pp. 176-183, https://doi.org/10.1016/j.jnucmat.2009.03.041.

Meyer, M.K. et al. (2008), "The EBR-II X501 Minor Actinides Burning Experiment", INL/EXT-08-13835, https://doi.org/10.2172/926343.

Nicolaou, G., K. Richter, L. Koch and C. Prunier (1993), "Experience with fast reactor fuels containing minor actinides: Transmutation rates and radiation doses", IAEA-TECDOC-78, Proceedings of a Technical Committee meeting held in Vienna, 29 November-2 December 1993, pp. 203-208, https://inis.iaea.org/collection/NCLCollectionStore/_Public/26/047/26047879.pdf?r=1.

Ohta, H., T. Ogata, S. Van Winckel, D, Papaioannou and V.V. Rondinella (2016), "Minor actinide transmutation in fast reactor metal fuels irradiated for 120 and 360 equivalent full-power days", *Journal of Nuclear Science and Technology*, 53:7, 968-980, http://dx.doi.org/10.1080/00223131.2015.1086706.

Ohta, H., T. Ogata, D. Papaioannou, V.V. Rondinella, M. Masson and J.-L. Paul (2015), "Irradiation of minor actinide-bearing uranium-plutonium-zirconium alloys up to ~2.5 at.%, ~7 at.% and ~10 at.% burnups", *Nuclear Technology*, Vol. 190/1, pp. 36-51, https://doi.org/10.13182/NT14-50.

Ozawa, T. (2017), "Analysis of fast reactor fuel irradiation behaviour in the MA recycle system", *Proceedings of the 2017 25th International Conference on Nuclear Engineering*, ICONE25, 2-6 July 2017, Shanghai, China.

Prunier, C., F. Boussard, L. Koch and M. Coquerelle (1993), "Some specific aspects of homogeneous Am and Np based fuel transmutation through the outcomes of the SUPERFACT Experiment in Phénix", Global '93, Seattle, Washington, https://inis.iaea.org/collection/NCLCollectionStore/_Public/24/070/24070171.pdf?r=1.

Trybus, C.L. et al. (1993), "Casting of metallic fuel containing minor actinide additions", *Journal of Nuclear Materials*, Vol. 204, pp. 50-55, https://doi.org/10.1016/0022-3115(93)90198-8.

Walker, C.T. and G. Nicolaou (1995), "Transmutation of neptunium and americium in a fast neutron flux: EPMA results and KORIGEN predictions for the superfact fuels", *Journal of Nuclear Materials*, Vol. 218/2, pp. 129-138, https://doi.org/10.1016/0022-3115(94)00649-0.

US DOE (2003), *Report to Congress on the Advanced Fuel Cycle Initiative: The Future Path for Advanced Spent Fuel Treatment and Transmutation Research*, US Department of Energy, Office of Nuclear Science and Technology.

4. Benchmark results

The choice of the physical quantities for the code-to-code comparisons and code-to-measures comparisons in this chapter was made considering the available data from PIE.

The state of the art of fuel behaviour knowledge in fast reactors (FRs) has been described in the literature (Guérin, 2012; Ogata, 2012). More recently, a state-of-the-art report published by the NEA Expert Group on Innovative Fuels described the effect of the introduction of MA in these fuel materials (NEA, 2014).

4.1. Oxide fuels

4.1.1. Results of the benchmark on the irradiation AFC-2C

Table 4.1 shows the results of the calculations performed with the different codes.

Discrepancies were observed between the different codes for the maximum temperature at beginning of life (Figure 4.5a). This is due to the different descriptions of the gap thickness evolution and fuel properties, in particular the fuel thermal conductivity. CEPTAR and FEMAXI-FBR both use Kato's correlation (Kato et al., 2011), while GERMINAL uses Philipponneau's (Philipponneau, 1992).

At end of life (EOL) (Figure 4.5c), the mechanisms contributing to the heat transfer are not predicted to have the same weight (GERMINAL vs. FEMAXI-FBR). With a common prediction of a closed gap, FEMAXI-FBR describes an increase of heat transfer coefficient due to an increase of contact pressure between fuel and cladding, with a stabilised fission gas release. On the other hand, the prediction calculated with GERMINAL describes a maintained increase of fission gas release, leading consequently to a decrease of heat transfer coefficient.

The contribution of the fuel gas swelling to gap closure should be evaluated to quantify its influence on thermal regime, specifically at EOL.

Another cause of differences is the description of the oxygen evolution inside the fuel. Some codes describe the return to stoichiometry in oxygen (oxidising effect of fission, observed experimentally), while others do not. Similarly, some codes describe the radial redistribution of oxygen; others do not. Since deviation from stoichiometry has a strong influence on the oxide fuel thermal conductivity, this represents another cause of discrepancies between the different calculation results, particularly for the temperature field in the pellet.

Table 4.1. Irradiation AFC-2C rodlet 3: Comparison of experimental and calculation results

AFC-2C – rodlet 3	Measurements	GERMINAL	CEPTAR	FEMAXI-FBR
Burnup at EOL (at %)	5.5	5.78 (average along fuel stack)	5.59	5.26 (average)*
FGR (% and mol)	78 2.79x10^{-4}	67.7 2.50×10^{-4}	73.8 2.70×10^{-5}	47.3 1.68×10^{-4}
He release (% and mol)	7 7.83 x10^{-5}	100 1.22×10^{-4}	100 1.03×10^{-4}	100 2.18×10^{-4}
Final pin pressure (MPa)	0.74 (at 32°C)	1.70 (hot state) 0.70 (cold state)	1.34 (hot state) 0.48 (cold state)	0.48 (cold state)
Central hole diameter at peak power node (PPN) (mm)	0.611	0.67	0.95	0.53
Diameter JOG (µm)	Not measured	0 (no JOG)	0 (no JOG)	Not evaluated
Diameter gap pellet-clad (µm)	0-10 (max)	35.4 (average along fuel pellet)	47.2 (cold state)	0 (cold state)
Pu redistribution (near central hole) (at.%)	Initial value: 17 (no measurement after irradiation)	19.9	20.1	20.85
Fuel column elongation % (mm) initial = **37.97 mm**	1.4	0.6 (0.23)	0.11 (0.042)	3.1 (1.17
Exterior clad diameter increase (%)	0.8 (max)	+0.5 (max)	+0.4 (max)	- 0.16 (max)
Radial extent of columnar grains at PPN (mm)	3.7	2.32	3.718	1.41
Internal clad corrosion (µm)	80 (max)	48.2 (average along fuel stack)	0 (not calculated)	–
Maximum centre pellet fuel temperature at PPN (°C)	Not measured	2 096	1 922	1 952
Outer pellet temperature at PPN (°C)	Not measured	703	893 (max)	817 (max)
Internal clad temperature in the gap (°C)	Not measured	570	567 (max)	628 (max)
Max fast fluence (E>0.1 MeV) (neutrons/m^2)	n/a	Not used	3.91x10^{+25}	7.23x10^{+26}
Maximum dose on clad (DPA)	Not measured	Input	Not calculated	Not calculated

Note: EOL: end of life; FGR: fission gas release; JOG: joint oxyde gaine; DPA: displacements per atom.
* Isotopic variation not estimated by FEMAXI-FBR. Conversion based on 213 MeV/fission (Waltar and Reynolds, 1981).

The greatest differences between the three codes are found in the predictions of the evolution of columnar grain radius (Figure 4.4). The criteria to estimate columnar grain expansion are not the same for the models involved by the codes: CEPTAR uses criteria on fuel density (90% T.D. for CEPTAR), whereas GERMINAL and FEMAXI-FBR use criteria on temperature (1 800°C for GERMINAL grain growth correlation based on temperature and gas atom density at the grain boundary for FEMAXI-FBR). The predicted temperature field inside the pellet appears relatively far from the temperature range of the fuel restructuring.

The uncertainty about the power distribution inside the pellet may cause discrepancies between the code predictions and the measurements for the thermally induced mechanisms.

A common trend is observed for the code prediction for helium release, which is consistently overestimated because the assumption of the total release may not be appropriate for AFC-2C irradiation, which was operated at medium power conditions (see Table 4.1).

Figure 4.1. Inner and outer pellet temperature vs. time at maximum peak power node (AFC-2C rodlet 3)

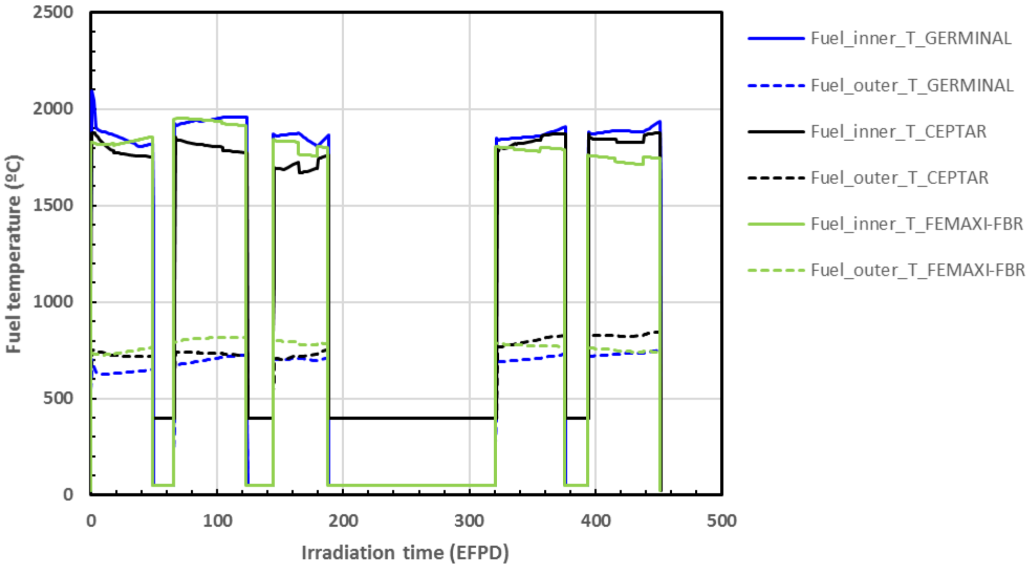

Note: EFPD: effective full power day.
Source: NEA EGIF data, 2019.

Figure 4.2. Fission gas release (AFC-2C rodlet 3)

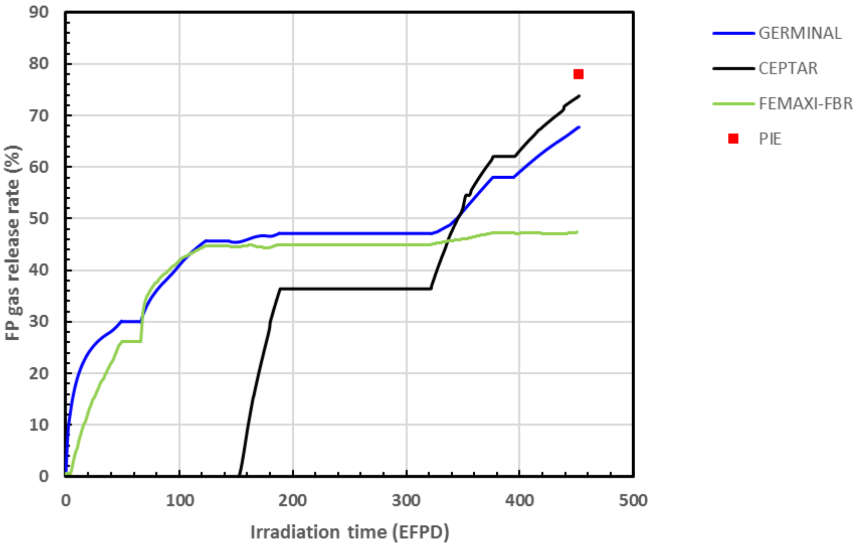

Note: FP: fission product; EFPD: effective full power day; PIE: post-irradiation examination.
Source: NEA EGIF data, 2019.

Figure 4.3. Pu, Am and O content vs. radial position at end of life (AFC-2C rodlet 3)

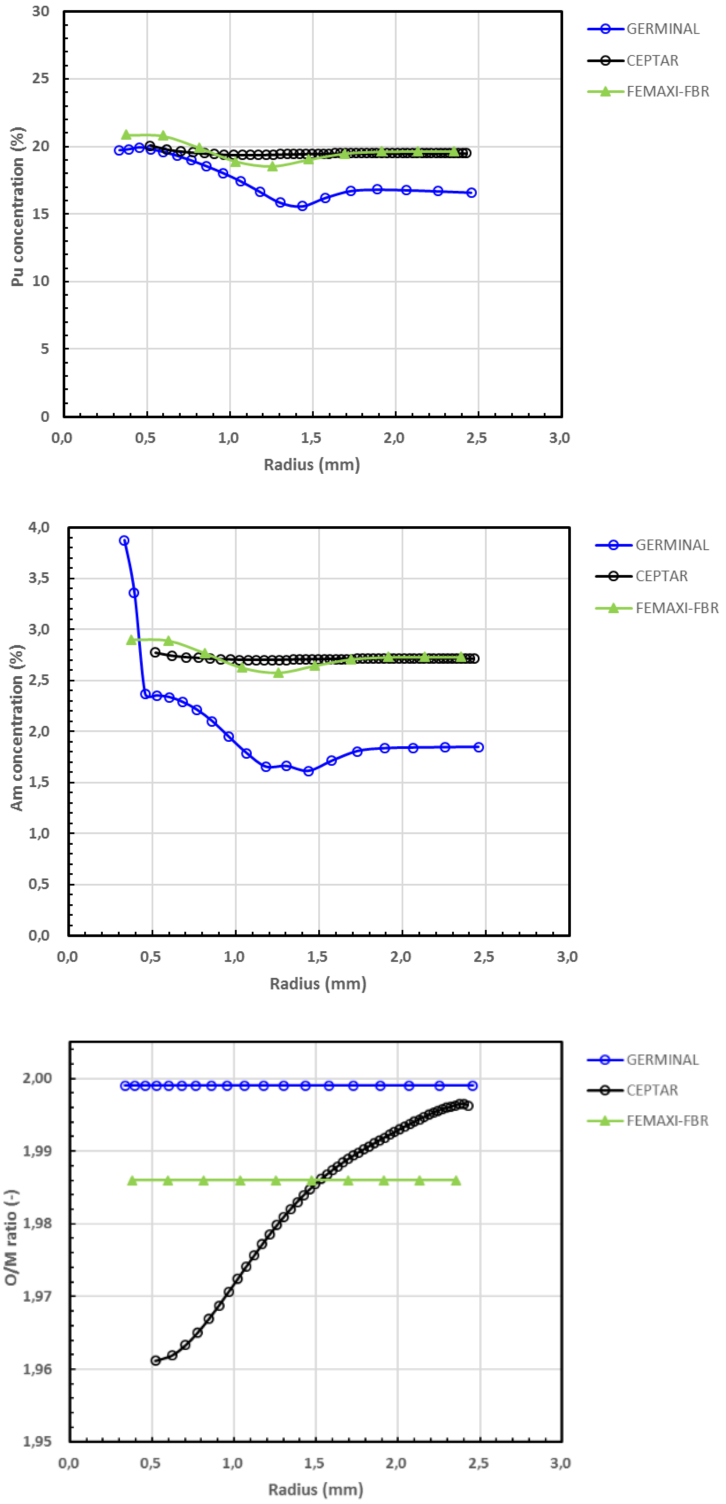

Source: NEA EGIF data, 2019.

Figure 4.4. Central hole diameter and columnar grain at maximum flux plan vs. time (AFC-2C rodlet 3)

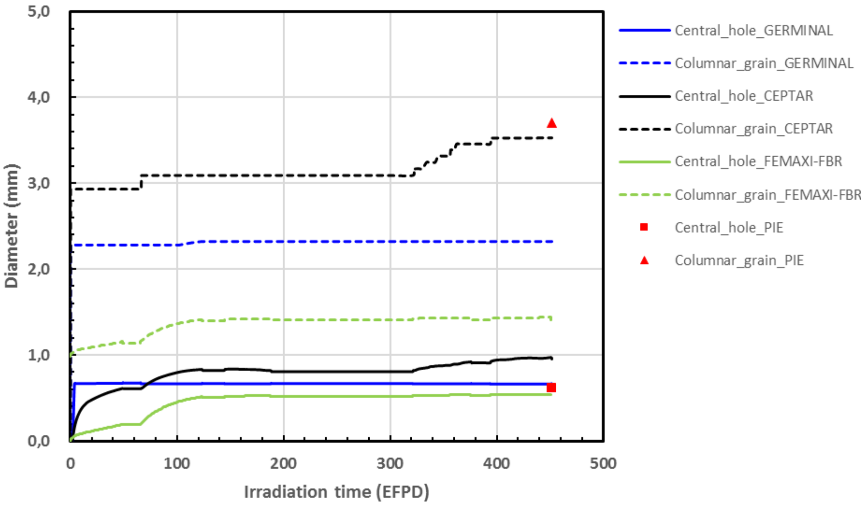

Note: EFPD: effective full power day; PIE: post-irradiation examination.
Source: NEA EGIF data, 2019.

Figure 4.5. Fuel temperature vs. radial position at (a) beginning of life, (b) just after central hole, and (c) formation and end of life (AFC-2C rodlet 3)

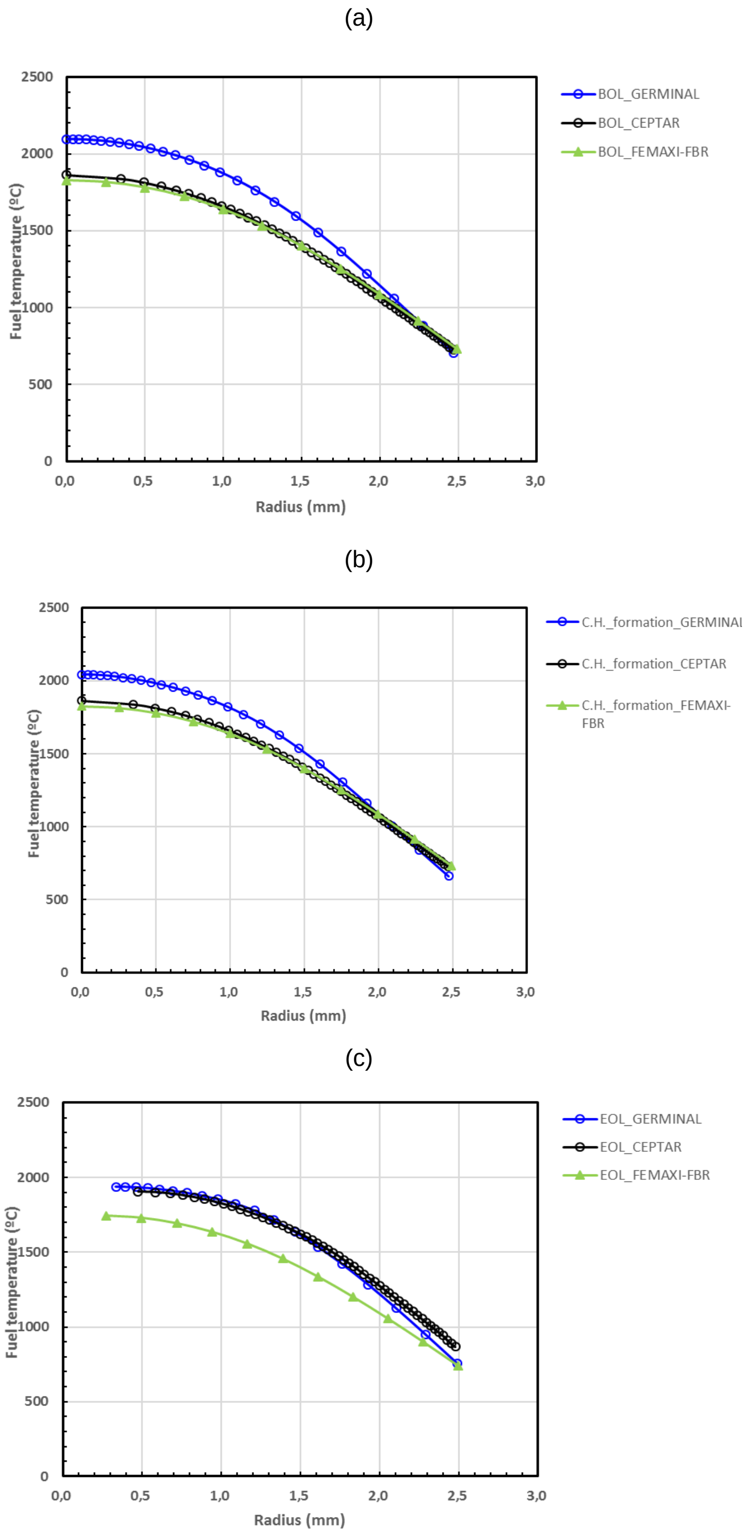

Note: BOL: beginning of life; CH: central hole; EOL: end of life.
Source: NEA EGIF data, 2019.

Figure 4.6. Evolution of gap vs. time at peak power node and gap conductance (AFC-2C rodlet 3)

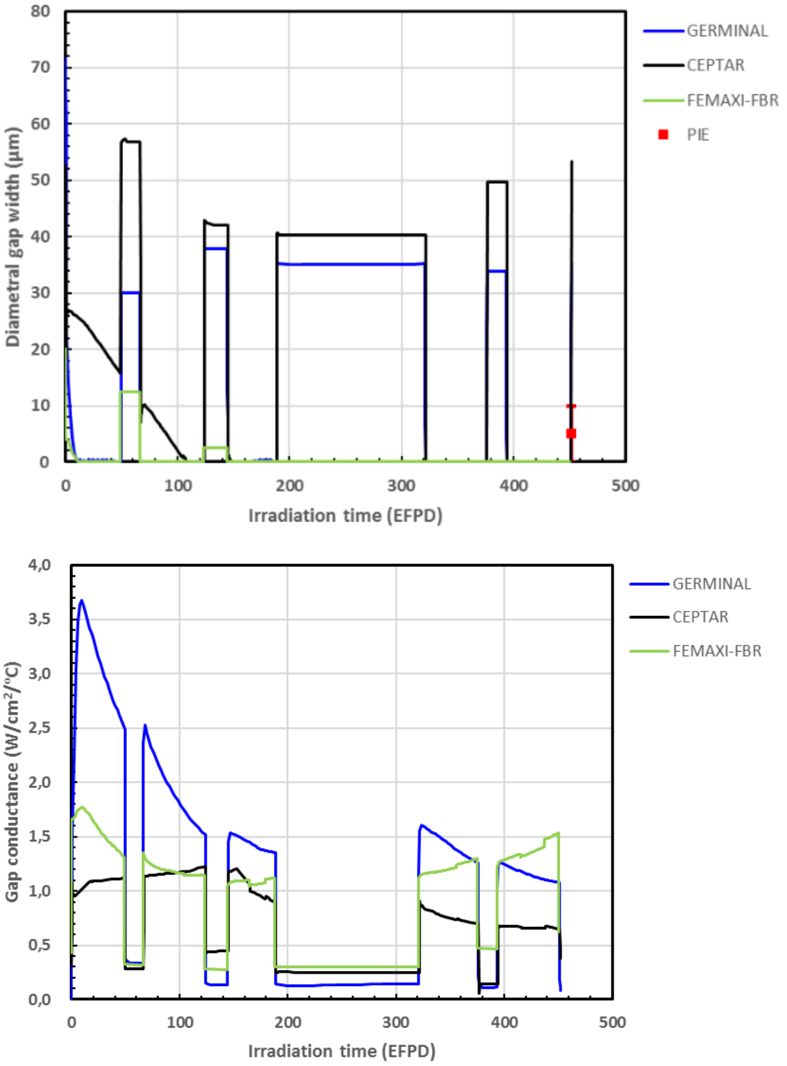

Note: PIE: post-irradiation examination; EFPD: effective full power day.
Source: NEA EGIF data, 2019.

4.1.2. Results of the benchmark on the Irradiation B8-HAM

Table 4.2 compares the results of the calculations performed with the different codes against the experimental results.

A general trend is observed for the helium release and its final quantity in the pin plenum: the helium release fraction is overestimated (Table 4.2) by the different codes (100% vs. 60.3% for the measurement), apart from TRANSURANUS, which underestimates the release fraction (20.89% vs. 60.3%). Surprisingly, when considering the total volume of helium released, all codes underpredict the measured value, except for FEMAXI-FBR, which overestimates the released volume of helium. This might be due to the different considerations of helium generation due to decay among the codes.

Table 4.2. Irradiation B8-HAM: Comparison of experimental and calculation results

B8-HAM	Measurements	GERMINAL	TRANSURANUS	CEPTAR	FEMAXI-FBR
Burnup at EOL (at.% and GWd/tHM)	2.96 (max)	2.89 (max)	2.72 (max) 27.2 GWd/tHM (max)	2.98 (max) Not calculated	2.65* (max) 26.5 GWd/tHM (max)
Integral FGR % (cm^3)	45.29 (20.05)	28.4 (14.38)	34.8 (15.82)	56.2 (24.7)	43.6 (17.75)
Integral He produced and released (% and cm^3 STP)	60.3 (3.266)	100 (2.96)	29.89 (1.81)	100 (2.27)	100 (7.56)
Final pin pressure (MPa)	0.324 (at 25°C)	0.717 (hot state) 0.254 (cold state)	0.76 (hot state) 0.25 (cold state)	Not calculated (hot state) 0.37 (cold state)	0.84 (hot state) 0.34 (cold state)
Central hole diameter at peak power node (PPN) (mm)	1.002	1.14	1.1	0.96	0.98
Diameter JOG (µm)	0 (no JOG)	0 (no JOG)	0 (no JOG)	0 (no JOG)	0 (no JOG)
Diameter pellet-clad gap (µm)	Not measured	15.8 at PPN	28.1 at PPN	140 at PPN	38 at PPN
Central Pu concentration at PPN	38.5 wt.%	31.5% at PPN	28% at PPN	35.2% at PPN	33.7% at PPN
Fuel column elongation % (mm) initial = 550 mm	+6.9	0.12 (0.66)	1.3 (7.83)	-0.45 (-2.45)	0.6 (3.3)
Exterior clad diameter increase (%)	Max. 0.4 ΔD/D	+0.07 (max)	+0.14 (max)	+0.004 ΔD/D (max)	0%
Radial extent of columnar grain growth at PPN (mm)	3.047	2.81	3.58	4.52	2.8
Internal clad corrosion thickness (µm)	Not measured	1.6 (max)	–	3.96 (max)	–
Maximum fuel central temperature at PPN (°C)	Not measured	2 309	2 554	2 191	2 171
Maximum outer pellet temperature at PPN (°C)	Not measured	816	753	996 (max)	777
Internal clad temperature in the gap (°C)	Not measured	508	565 (max)	518 (max)	512
Maximum fast fluence (E>0.1 MeV) (neutrons/m^2)	2.93 x10^{+26}	Not used	2.9 x10^{+26}	2.93 x10^{+26}	4.49 x10^{+26}
Maximum dose in clad (DPA)	14.64	Input	Not calculated	Not calculated	Not calculated

Note: EOL: end of life; FGR: fission gas release; STP: standard temperature and pressure; JOG: joint oxyde gaine; DPA: displacements per atom.

* Isotopic variation not estimated by FEMAXI-FBR. Conversion based on 213 MeV/fission (Waltar and Reynolds, 1981).

Significant differences were observed for the fuel temperature. They can be explained as follows:

- Gap closure evolution:

  GERMINAL predicts the fastest gap closure. Consequently, the fuel temperature predictions are the lowest (Figure 4.7), resulting from the highest heat transfer coefficient. The outer fuel temperature estimated by TRANSURANUS is consistent with the one calculated by GERMINAL, as both codes have the highest estimations of heat transfer coefficient.

  On the other hand, CEPTAR does not predict any gap closure during irradiation, even though the heat transfer coefficient in a gap has been calibrated by using short-term irradiation experiments in JOYO. However, this might lead to the highest prediction of the fuel outer temperature with a higher burnup, but not to the highest predicted inner temperature. This can explain the second main cause of differences, and is most likely related to dissimilar radial evolutions of thermal properties inside fuel.

- Fuel thermal conductivity estimation:

  One important cause of the discrepancy between the codes arises from the evaluation of the fuel thermal conductivity. The analysis of the differences between the predicted radial temperature profiles inside the fuel at the end of irradiation (Figure 4.13) mostly reveals the effects induced by different estimations of the fuel thermal conductivity.

A comparison of the predictions of GERMINAL and TRANSURANUS shows that the predicted temperature steps in fuel are significantly different, whereas the fuel outer temperature, the radial profile of the O/M ratio inside pellet and the central hole radius are estimated consistently. The radial temperature profile calculated by GERMINAL is therefore lower. This can be explained by the fact that different correlations for fuel thermal conductivity were used for the simulations: Kato’s correlation (Kato et al., 2011) was used for the GERMINAL calculation as suggested by JAEA, whereas the standard Philipponneau’s correlation (Philliponneau, 1992) was used for the TRANSURANUS calculation. Considering that both codes predict the return to stoichiometry in oxygen at the end of irradiation, this first possible cause of discrepancy can be discarded. The temperature and burnup dependences of the correlations can be suggested, but the porosity corrections are significantly different between Kato’s and Philipponneau’s correlation, the first one being adapted for Japanese fuels and the second one for French fuels; their microstructures are different (size of pore and grain). Regarding the B8-HAM experiment, the actual fuel density during irradiation will increase as a result of restructuring. For the purpose of this benchmark exercise, it was therefore decided to use one single correlation for the thermal conductivity in TRANSURANUS, rather than using a different correlation for the different experiments considered.

The predictions of CEPTAR and FEMAXI-FBR are in good agreement. The fuel outer temperatures predicted by both codes are the highest, due to the lowest evaluations of the fuel-to-cladding gap thermal conductance at the end of irradiation (see Figure 4.14b). The predicted temperature steps in fuel are in relative good agreement. The law for fuel thermal conductivity used in CEPTAR and FEMAXI-FBR is Kato’s correlation (Kato et al., 2011), leading to a consistent temperature increase in fuel at the beginning of irradiation. In addition, the burnup dependence is also expected to be consistent in both codes. GERMINAL predicts a similar temperature step (similar conductivity integral) but the temperature profile is globally translated down, because of the highest evaluation of the fuel-to-cladding gap heat transfer coefficient at the end of irradiation.

It should be noted that the as-fabricated B8-HAM fuel is very close to stoichiometry, having an initial (O/M) ratio of 1.99. The discrepancies linked to the oxygen evolution might have an impact on the fuel thermal conductivity estimation. The differences between the modelling implemented in the codes are clearly visible, considering the predictions of O/M radial profile at the end of irradiation (Figure 4.9c):

- FEMAXI does not predict the radial redistribution of oxygen and the return to stoichiometry along irradiation;
- CEPTAR predicts the radial redistribution of oxygen, but not the return to stoichiometry;
- TRANSURANUS and GERMINAL both predict the radial redistribution and the return to stoichiometry.

An analysis of the differences between the codes in estimating the fuel thermal conductivity confirms that the knowledge of the fuel properties and of their evolutions along irradiation represents a key point for fuel performance evaluation. This also highlights the needs for complementary research activities on fuel properties to improve the reliability of the simulations. A sensitivity analysis was performed with the different correlations for fuel properties evaluation used by the participants, leading to the above-mentioned conclusions.

Discrepancies were observed for fission gas release predictions (Figure 4.8) and are mainly due to different thermal regime evaluations. Moreover, the models describing this mechanism are different for each code: there is a threshold effect for CEPTAR, a lower threshold for FEMAXI-FBR and TRANSURANUS, and no threshold for GERMINAL. This influences the evolution of the heat transfer in the gap: at the beginning of irradiation, with a constant gap size and below the fission gas release threshold, the gap conductance predicted by CEPTAR is constant, whereas it quickly increases with GERMINAL, due to gap closure, and further decreases as a consequence of continuous gas release. The main difference observed between the codes is the trend of gap conductance with irradiation time, especially once the gap is closed. When considering the results from TRANSURANUS, the gap conductance in this case is less affected by the poisoning effect of the gas release, but rather by the increasing conductance due to an increasing contact pressure. It is difficult to draw definite conclusions about this point.

It should be noted that a direct experimental evaluation of the gap conductance is not possible, since: 1) there are no online measurements of temperature, gap size and fission gas release in an FBR; and 2) the gap conductance, derived from EOL measurements, has to be assessed in combination with the models for relocation, fuel restructuring and swelling, cladding deformation, etc.

Concerning plutonium redistribution, there is a small trend of underestimation in the code predictions, but covered by the uncertainty range of measurements. The predicted central hole expansion is also consistent with measurements.

The predictions for columnar grain expansion are considerably different, as explained above: the models’ criteria are different (density vs. temperature), leading to a significant difference from the observed value.

Figure 4.7. Inner and outer pellet temperature (B8-HAM)

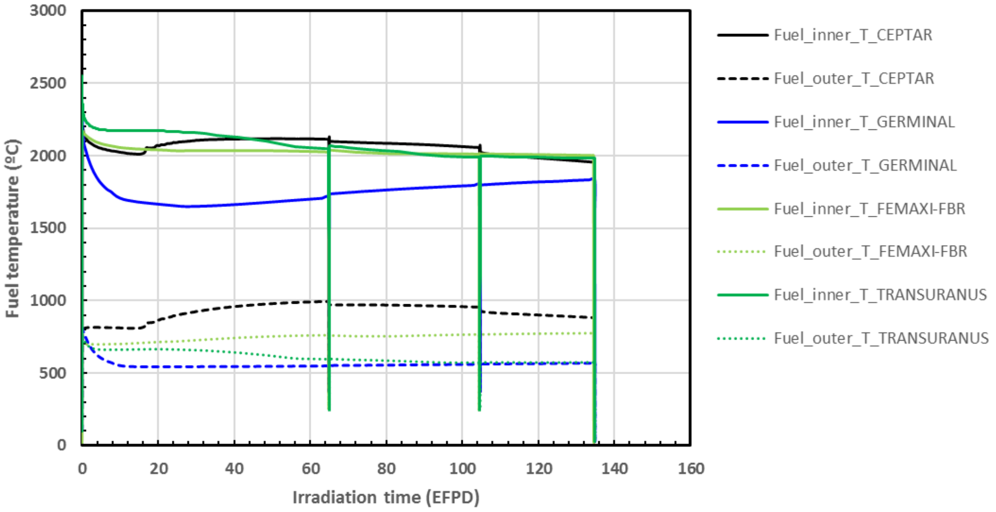

Source: NEA EGIF data, 2019.

Figure 4.8. Fission gas release (B8-HAM)

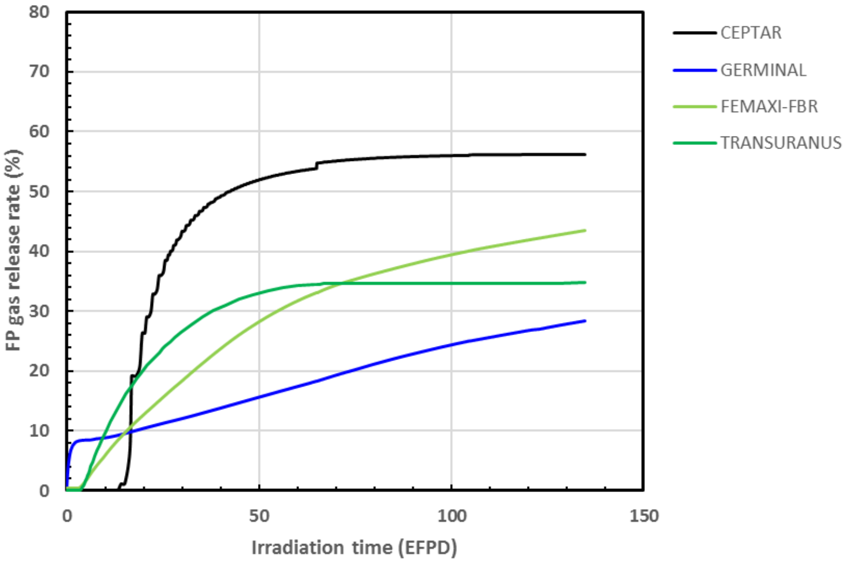

Note: FP: fission product; EFPD: effective full power day.
Source: NEA EGIF data, 2019.

Figure 4.9. Pu content (a), Am content (b) and oxygen-to-metal ratio (c) at end of life (B8-HAM)

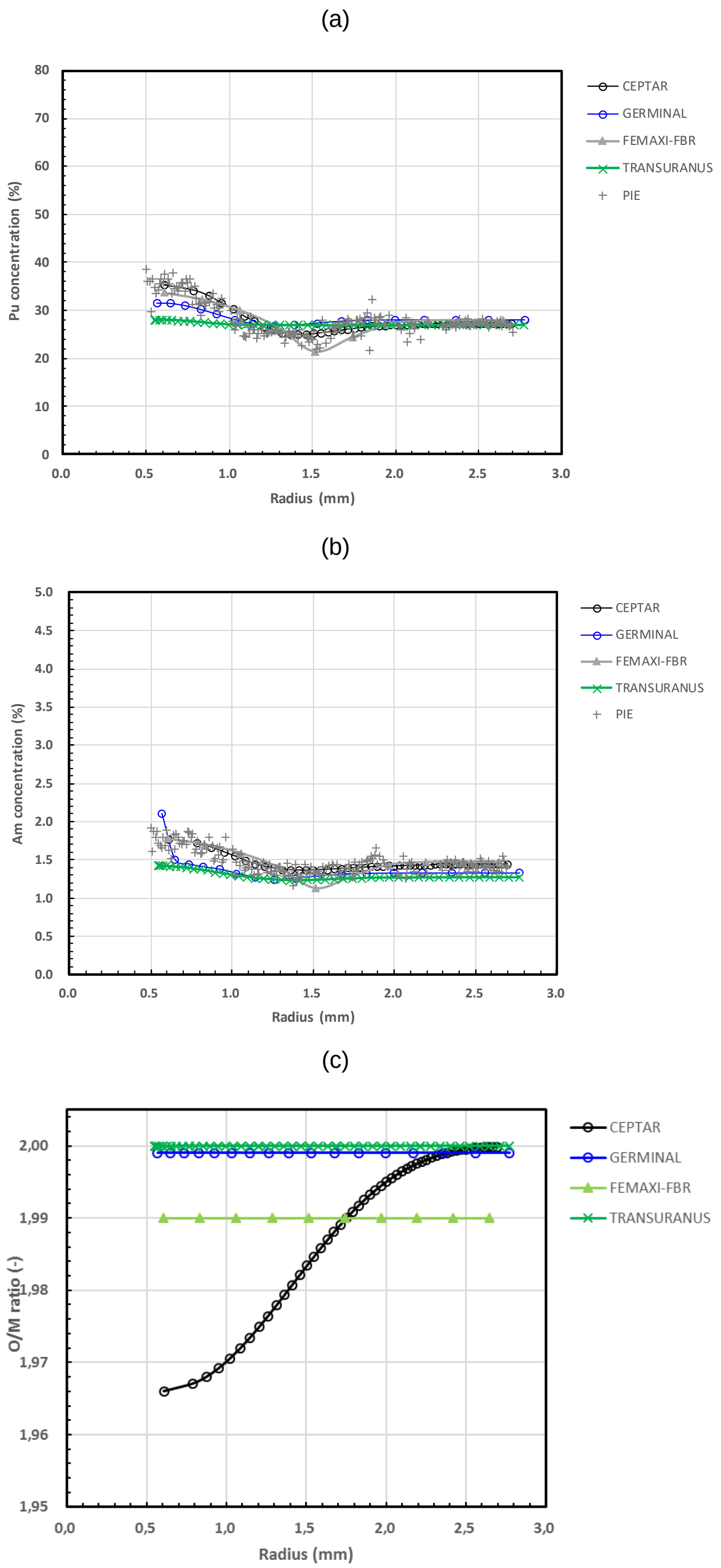

Note: PIE: post-irradiation examination; O/M: oxygen-to-metal.
Source: NEA EGIF data, 2019.

Figure 4.10. Central hole diameter and columnar grain at maximum flux (B8-HAM)

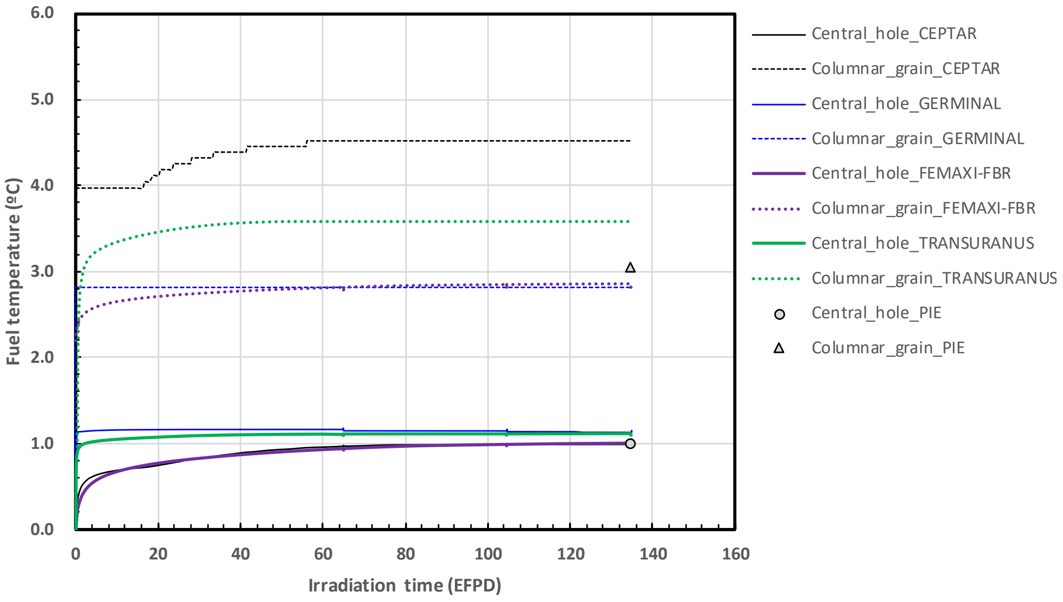

Source: NEA EGIF data, 2019.

Figure 4.11. Fuel temperature vs. radial position at beginning of life (B8-HAM)

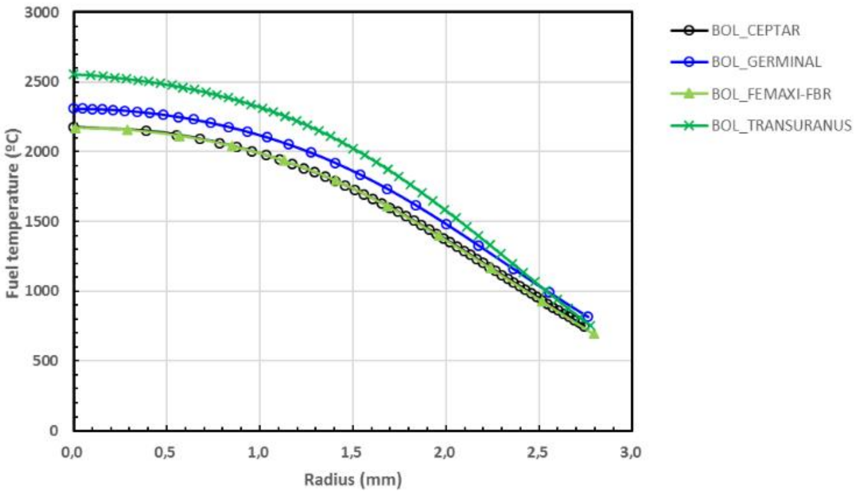

Note: PIE: post-irradiation examination; EFPD: effective full power day; BOL: beginning of life.
Source: NEA EGIF data, 2019.

Figure 4.12. Fuel temperature vs. radial position just after central hole formation (B8-HAM)

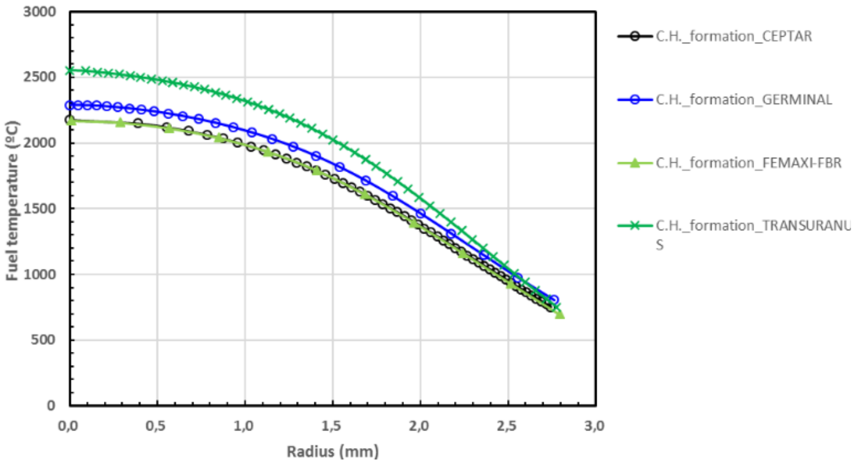

Note: CH: central hole.
Source: NEA EGIF data, 2019.

Figure 4.13. Fuel temperature vs. radial position at end of life (B8-HAM)

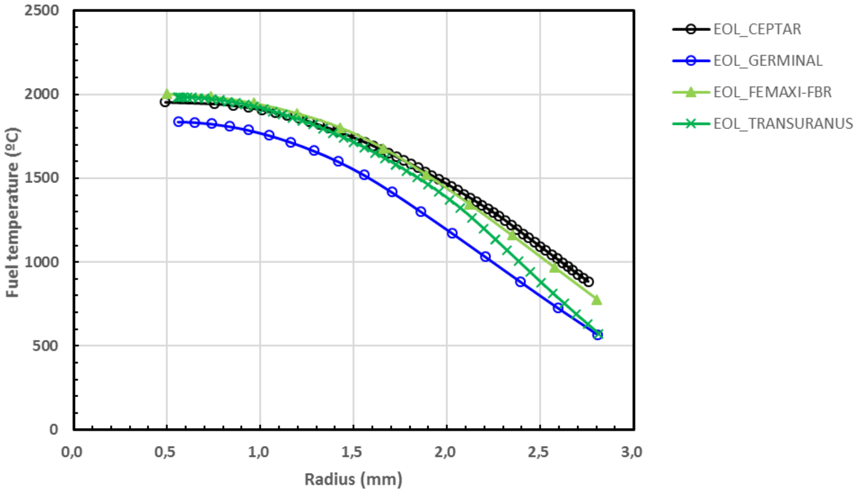

Note: EOL: end of life.
Source: NEA EGIF data, 2019.

Figure 4.14. Evolution of gap (a) at peak power node and (b) gap conductance (B8-HAM)

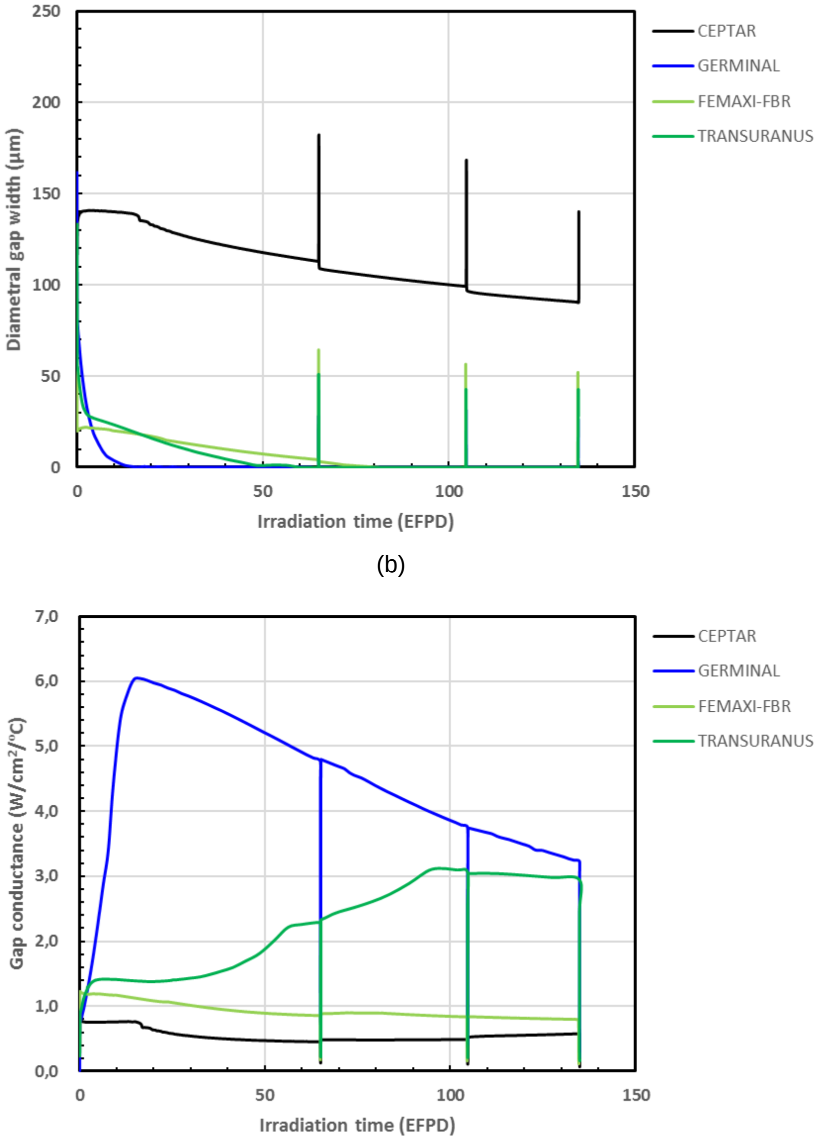

(a)

(b)

Note: EFPD: effective full power day.
Source: NEA EGIF data, 2019.

4.1.3. Results of the benchmark on the irradiation SUPERFACT

Table 4.3 compares the results calculated with the different codes against the experimental results.

Table 4.3. Irradiation SUPERFACT – pin 4: Comparison of experimental and calculation results

SUPERFACT – pin 4	Measurements	GERMINAL	TRANSURANUS	CEPTAR	FEMAXI-FBR
Burnup at EOL (at. %)	6.4 max	6.87 (max)	6.50 (max)	6.44	6.33 (max)*
FGR% (cm^3 STP)	68 154.61	66.6 157.47	58.5 137.8	56.6 135.77	58.99 137.6
He release (% and cm^3 STP)	100 39.89	100 39.73	82.4 32.1		100 71.5
Final pin pressure (MPa)	–	2.537 (hot state) 1.077 (cold state)	2.54 (hot state) 0.99 (cold state)	1.913 (hot state) 0.825 (cold state)	2.864 (hot state) 1.126 (cold state)
Central hole diameter at peak power node (PPN) (mm)	0.57	1.15	0.63	0.49	0.38
Diameter JOG (µm)	0 (no JOG)	0 (no JOG)	0 (no JOG)	0 (no JOG)	0 (no JOG)
Diameter gap pellet-clad (µm)	21 at PPN	22.5 at PPN	32.1 at PPN	42.0 at PPN	22.4 at PPN
Pu redistribution (near central hole)	No redistribution Average 19.3% at PPN	22.05% at PPN	20.97 wt.% at PPN	22.2 wt.% at PPN	22.92% at PPN
Fuel column elongation % (mm) initial = **847.8 mm**	0.73 (6.2)	0.735 (6.235)	2.9 (24.8)	-0.307 (-2.600)	0.07 (0.56)
Exterior clad diameter increase	+0.47% (max)	+0.33% (max)	0.44% (max)	+0.55 %ΔD/D (max)	0%
Columnar grain diameter at PPN (mm)	2.31	3.58	4.71	4.40	3
Internal clad corrosion (µm)	<50	40.8 (max)	–	0 (not calculated)	–
Maximum centre pellet fuel temperature at PPN (°C)	–	2 483	2 586	2 363 (max)	2 233
Outer pellet temperature at PPN (°C)	–	978	1 087	905 (max)	1 011
Internal clad temperature in the gap (°C)	–	535	565	539 (max)	549
Maximum fast fluence (E>0.1 MeV) (neutrons/m^2)	–	Not used	Not calculated	$2.25 \times 10^{+27}$	$1.19 \times 10^{+27}$
Max dose on clad (DPA)	52	Input		Not calculated	Not calculated

Note: EOL: end of life; FGR: fission gas release; STP: standard temperature and pressure; JOG: joint oxyde gaine; DPA: displacements per atom.

* Isotopic variation not estimated by FEMAXI-FBR. Conversion based on 213 MeV/fission (Waltar and Reynolds, 1981).

The simulation of SUPERFACT reveals differences between the gap evolution and its effect on thermal heat transfer between pellet and cladding, which are consistent with results from the previous cases. The estimations of the gap thermal conductance are very different from one code to another and are mostly linked to the evolution of the gap thickness (affected by relocation, swelling, creep, etc.). Specific analytical experiments combined with 3D simulations are therefore suggested to more accurately assess the microstructural changes as well as the microscopic changes induced by strong thermal gradients in fast reactor oxide fuels.

The differences between predicted fuel temperatures (Figure 4.15) are consistent with those observed for the two previous cases; they are linked to gap closure in particular.

The size and the resulting heat conductance of the fuel-to-cladding gap play a key role in calculating the thermal and mechanical behaviour of the fuel element. The gap size can either be intuitively the distance between the pellet outer radius and the cladding inner radius (as in TRANSURANUS and GERMINAL), or an effective mechanical or thermal gap size applied in the code. This second approach allows considering the eccentricity of the pellets and/or the fragments. In all code predictions of the SUPERFACT irradiation, the gap size decreases very rapidly at the beginning of irradiation, mainly as a result of the fuel relocation. Due to its stochastic nature, the relocation process is, however, not well known, especially the kinetics of the mechanism. This is reflected in the various models (correlations) available in open literature. GERMINAL, TRANSURANUS and FEMAXI-FBR use one of these models. Due to the unavailability of instrumented irradiation experiments, the validation of these models is not possible due to coupling effects.

It is important to note that the physics described by all the models is not always the same: behind a common term of “relocation”, even the driving physical mechanisms that are considered are not the same. Relocation models for pressurised water reactor fuel rods usually describe an outward movement of fuel fragments under the influence of the thermal gradient and the corresponding 3D deformations. As this shape cannot be predicted with a 1D-radial model, an additional displacement is taken into consideration for this effect. Some relocation models for fast reactor fuel pins (e.g. GERMINAL) also consider a second physical mechanism: fuel fragments relocation towards clad inner bound as a macroscopic effect induced by the thermally activated fuel material radial redistribution. A closer look at the beginning of irradiation also indicates that the gap size of TRANSURANUS slightly increases after relocation is complete, which is not observed in the other code predictions. While fuel densification is an empirical model that also needs to be adapted to the particular fuel type (depending on total porosity, pore size-distribution, etc.), it does not seem to play an important role in view of the limited amount of porosity in the pellets of SUPERFACT. The explanation and the description of the mechanisms contributing to the fuel-to-cladding gap evolution are far from reaching a consensus. This underlines the need for future analytical experiments – especially short-term ones – to investigate further the correlations between the physical mechanisms occurring at beginning of life, in particular during first heat-up.

Moreover, the SUPERFACT case reveals important differences between the different codes in the description of fission gas release. The release rate at the EOL is quite consistent with the measurements, but the way the different codes reach the final value are significantly different. There is a visible threshold effect in gas release predicted by CEPTAR, probably linked to the use of a correlation established for low density fuel (effect of gas trapping in porosity). The initial peak of gas release predicted by GERMINAL is an artefact of simulation, induced by excessive thermal activation at maximum temperature. It is interesting to note that a more simplified power history (applied in earlier simulations by TRANSURANUS) only has an insignificant impact on the calculated quantities at the end of irradiation. This can be explained by the fact that the released quantity of fission gases at the end of irradiation represents a “time-integrated” result. Simplifications introduced in the description of power increase/power decrease at the beginning/end of each cycle have an insignificant impact on the released quantity at the end of irradiation, as the duration of these evolutions (power increase/decrease) are negligible compared to the cumulated duration of the cycles. For the same reason, the initial peak of gas release predicted by GERMINAL only has a negligible impact on the final release rate (ratio of the released quantity since the beginning of irradiation divided by the produced quantity since the beginning of irradiation). The initial peak of release rate during the first heat-up has a negligible impact on the result.

The temperatures in the fuel are predicted to increase during the first irradiation cycle by FEMAXI-FBR and TRANSURANUS. This is due to a combination of gap size reduction and early fission gas release leading to thermal feedback. For the last irradiation cycle, gas release is consistently predicted by the different codes, apart from the gap thickness, which is still open for CEPTAR, and leads to the maximum fuel temperature at the end of irradiation (estimated by CEPTAR).

In the SUPERFACT irradiation, no significant plutonium redistribution was observed. Inversely, the calculations by GERMINAL, CEPTAR and FEMAXI-FBR showed a heterogeneous repartition of plutonium inside the pellet at the end of irradiation. This may be due to the transport properties sensitivity to the O/M ratio, which is not taken into account by the models. With a lower initial O/M ratio in SUPERFACT fuel, partial pressures of oxides are comparable, leading to no preferential migration of uranium. The results obtained by TRANSURANUS are in better agreement with the experiments. With a return to stoichiometry predicted faster than for other codes, the partial pressures of uranium oxides estimated by GERMINAL become greater than those of plutonium oxides earlier in irradiation, leading, as a consequence, to a heterogeneous repartition of actinides at end of irradiation.

The low stoichiometry also has an effect on fuel thermal conductivity, which is not taken into account in the same manner by the different codes, as underlined in the previous irradiation cases. Furthermore, the laws that are used to evaluate the fuel thermal conductivity are different: CEPTAR and FEMAXI-FBR use Kato's correlation (Kato et al., 2011); GERMINAL and TRANSURANUS use Philipponneau's correlation (Philipponneau, 1992). This will affect temperature predictions in fuel, and consequently fuel restructuring and gas release.

The analysis of the differences between predictions for the columnar grain expansion is similar to the explanation given for the previous irradiations. It should be kept in mind that not only do the temperature differences have an effect but the models for the columnar grain growth are subject to uncertainties, similar to even models for normal grain growth in fresh MOX published in Van Uffelen et al. (2013). The criteria used to define the columnar grain zone differ; as previously mentioned, some codes use the temperature as the empirical limit while others apply grain growth models and define a given size as a limit.

Figure 4.15. Inner and outer pellet temperature vs. time at maximum peak power node (SUPERFACT – pin 4)

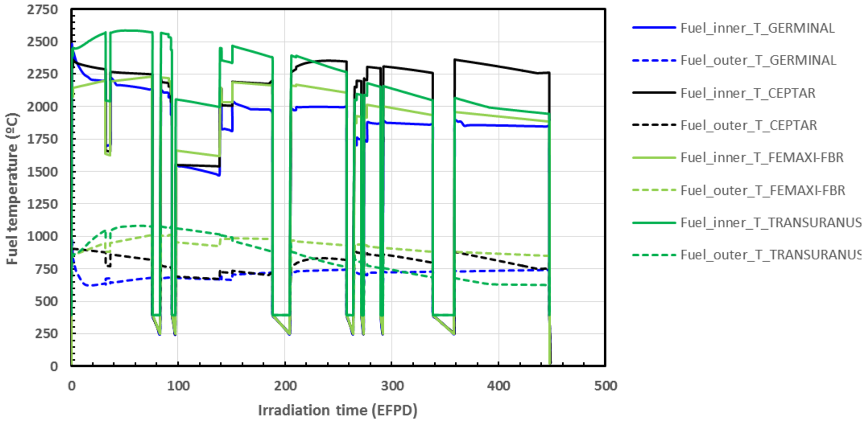

Note: EFPD: effective full power day.
Source: NEA EGIF data, 2019.

Figure 4.16. Fission gas release (SUPERFACT – pin 4)

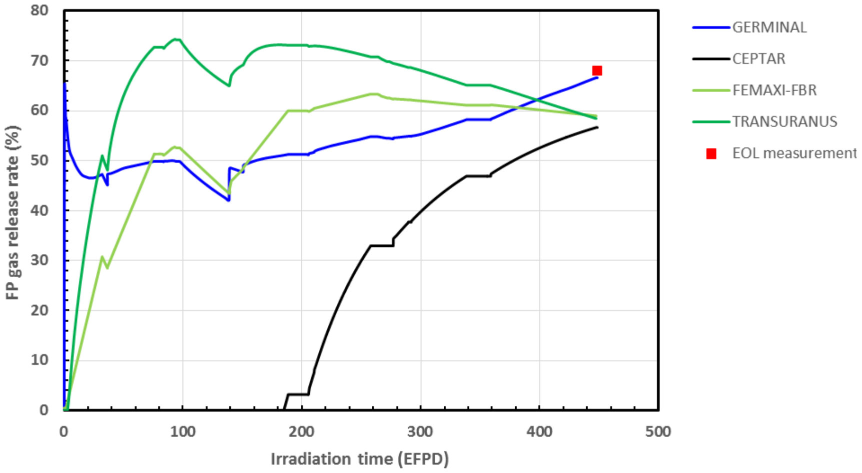

Note: FP: fission product; EOL: end of life; EFPD: effective full power day.
Source: NEA EGIF data, 2019.

Figure 4.17. Pu, Am and O content vs. radial position at end of irradiation (SUPERFACT – pin 4)

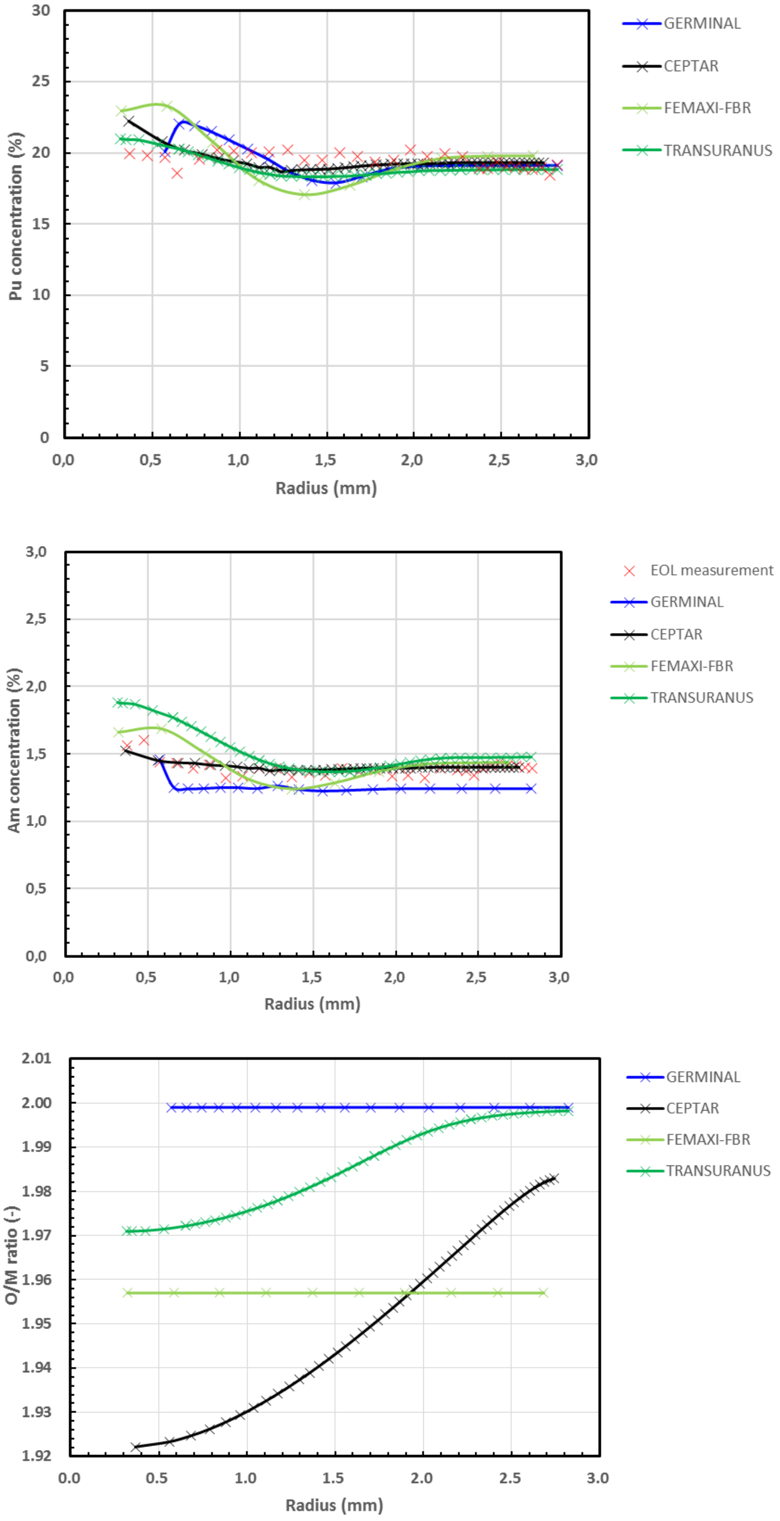

Source: NEA EGIF data, 2019.

Figure 4.18. Central hole diameter and columnar grain at maximum flux plan vs. time (SUPERFACT – pin 4)

At cold state

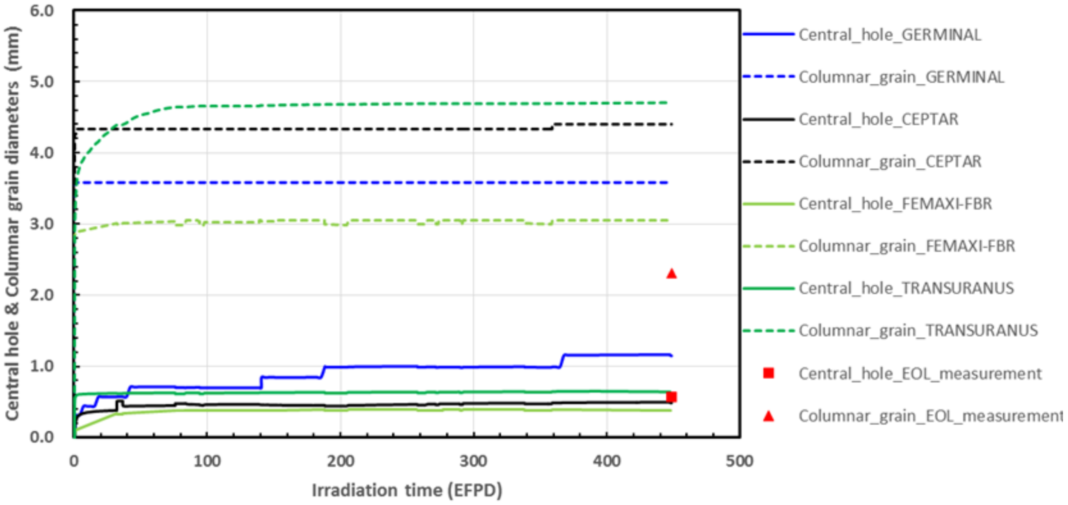

Note: EFPD: effective full power day; EOL: end of life.
Source: NEA EGIF data, 2019.

Figure 4.19. Fuel temperature vs. radial position at (a) beginning of life, (b) just after central hole formation and (c) end of life (SUPERFACT – pin 4)

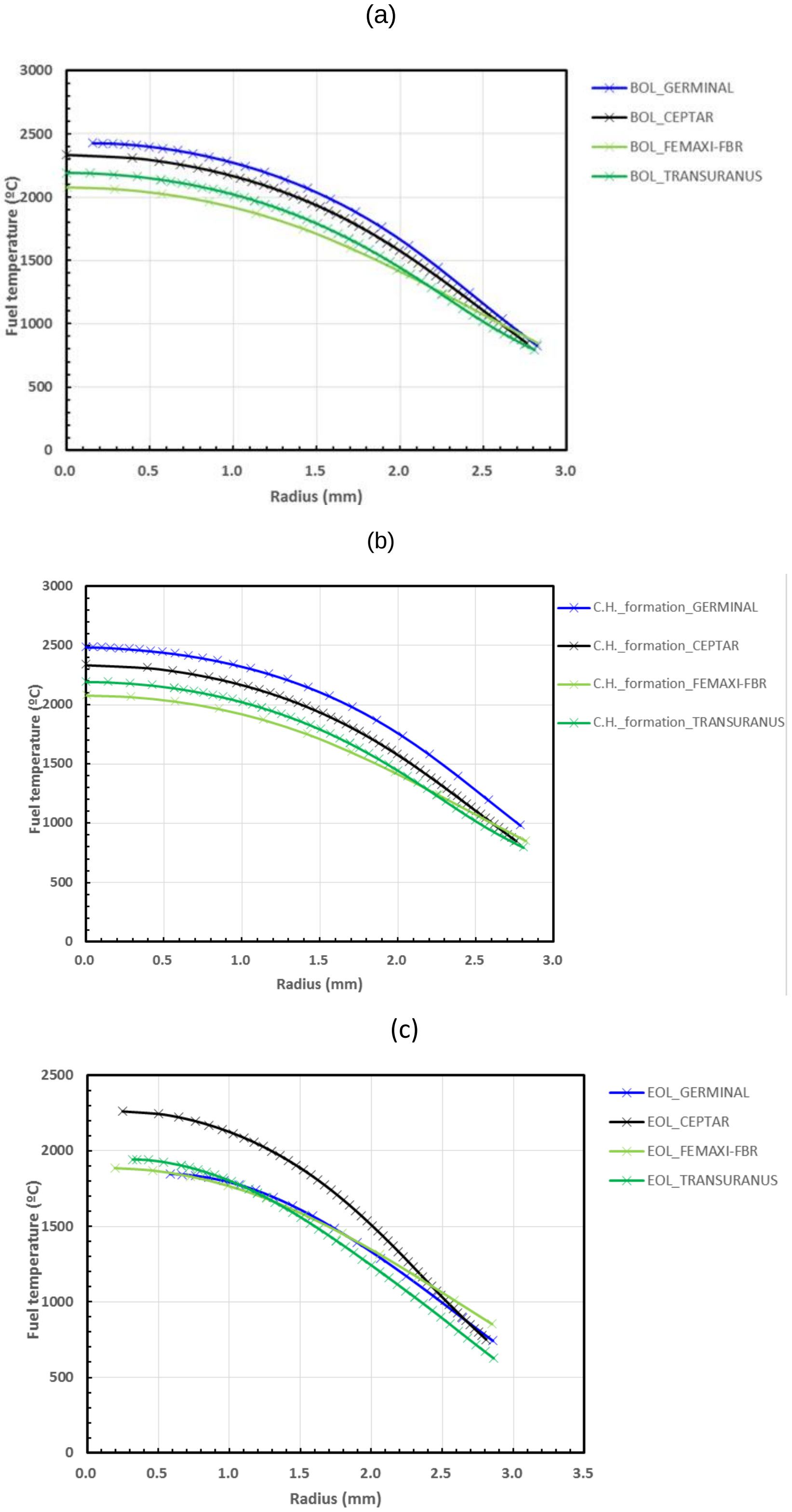

Note: BOL: beginning of life; CH: central hole; EOL: end of life.
Source: NEA EGIF data, 2019.

Figure 4.20. Evolution of gap vs. time at (a) peak power node and (b) gap conductance (SUPERFACT – pin 4)

At cold state

(a)

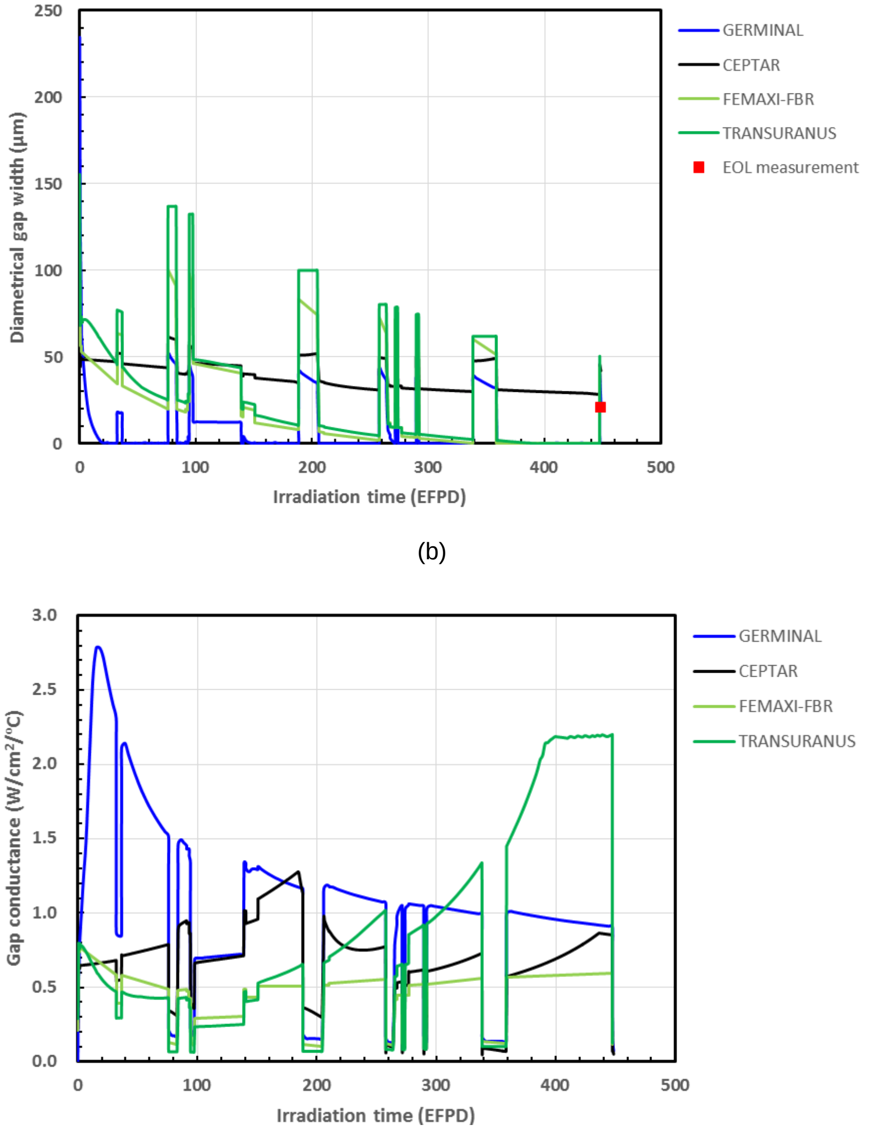

(b)

Note: EFPD: effective full power day; EOL: end of life.
Source: NEA EGIF data, 2019.

4.1.4. Summary and conclusions on the benchmark exercise for oxide fuels

The benchmark exercise for the oxide fuels proved to be a good opportunity to compare fuel performance codes for fast reactor fuels, a study that had not been carried out for a while. Discrepancies between codes and experimental results show that the MA loading for the considered fuel materials is not the source of these differences. Even if most of the codes are not validated for these specific compositions, the results are encouraging. Nevertheless, to increase the reliability of code results for transmutation applications, this exercise has provided lessons and has shown some ways of improving the modelling that are to be implemented in the codes.

The most important discrepancy between the calculation results deals with the temperature predictions, since they affect all the other processes. The discrepancies between calculations may be due to three main reasons:

1. prediction of gap size evolution as a result of the combination of several phenomena: fuel swelling and creep, pellet fragments relocation and clad deformation;
2. estimation of gap heat conductance, linked to gap size evolution and to fission gas release;
3. evaluation of fuel thermal conductivity as a result of radial redistribution of actinides and oxygen.

A deeper analysis showed that the gap conductance predictions are quite scattered throughout the irradiation. One of the main factors influencing this parameter is the gap size, i.e. the average distance between the pellet outer surface and the cladding inner surface. In all code predictions of the oxide fuels cases, the gap size decreases rapidly at the beginning, mainly due to the fuel relocation and thermal expansion. The relocation process, in particular the kinetics of the mechanism that includes the unforeseen occurrence of cracking in a pellet, is not yet completely understood. This phenomenon causes a variety of gap conductance evaluation among codes. These results showed that more accurate experimental data are needed from analytical experiments for the micro- and macro-structural changes in the pellets as a function of temperature, in combination with the multidimensional and/or multiscale simulations available today. Such experiments could, for instance, rely on the laser-based measurements used to derive the high-temperature properties of fuels. Furthermore, to achieve a level of validation of fuel performance codes for fast reactor fuel that is similar to the one achieved for LWR fuels, the online measured (central) temperatures and internal pressures during irradiation (online measurements of gas release) are useful. However, experiences in the JOYO reactor, i.e. instrumented test assembly experiments, revealed that this kind of online measurement is difficult, especially in the case of FR irradiation, due to the errors caused by higher fuel temperature and higher fast neutron dose on the device compared to LWR irradiations.

The laws for fuel thermal conductivity implemented in the codes take into account different parameters, the temperature but also the deviation from stoichiometry, density and burnup effects. The estimations of the input parameters and the law themselves are different among the considered codes, leading to differences in the property evaluation and consequently in the temperature field in fuel.

In conclusion, it is recommended to improve the models listed above to increase the reliability of the code results through analytical experiences and micro-characterisations and properties measurements on fresh and irradiated fuels.

Nevertheless, the irradiations studied in this benchmark did not reach high performances in terms of final burnup and transmutation rate. For higher performances, the impact of MA on the fuel behaviour should be considered:

- high helium production and release will affect the gap conductance and the gaseous swelling;
- the increase of oxygen potential will enhance the FCCI;
- the effect on thermal properties (namely thermal conductivity and melting temperature).

These effects of MA loading may have consequences for some situations to be considered for safety analysis.

4.2. Metal fuels

4.2.1. Results of the benchmark on the irradiation AFC-1H

Table 4.4 shows the results of the calculations from the different codes and compares them with the results of the experiments for the irradiation AFC-1H.

Table 4.4. Irradiation AFC 1H – rodlet 4: Comparison of experimental and calculations

AFC 1H pin 4	Measurements	ALFUS	MACSIS
Burnup (at.%)	26.68	26.68	23.7
Fission gas (Xe+Xr) release (%)	77.8	90.7	80.5
Final pin pressure (MPa)	1.59 (32°C)	4.77 (530°C) 1.83 (20°C)	2.75 MPa (501°C) 1.02 MPa (22°C)
Diameter gap fuel slug-clad (μm)	0 (full contact)	0 (full contact)	0 (full contact)
Zr redistribution	Not measured		–
Fuel slug elongation (%)	13	12.8	6.2
Exterior clad diameter increase (%)	<1.6	<0.04	<0.1
FCCI thickness (μm)	Not measured	58-73	22
Maximum fuel slug centerline temperature (°C)	Not measured	760	751
Maximum fuel slug surface temperature (°C)	Not measured	580	550
Maximum cladding inner wall temperature (°C)	Not measured	526 (mid-wall)	536
Maximum fast fluence (E>0.1 MeV) (neutrons/m^2)	n/a	2.43×10^{22}	–
Maximum dose on clad (DPA)	Not measured		–
Final plenum volume (cc)	1.52	1.45	1.38

Note: FCCI: fuel-cladding chemical interaction; DPA: displacements per atom.

Both the MACSIS and the ALFUS codes were tuned, verified and validated by using the data of U-Zr and U-Pu-Zr test fuel pins irradiated in the EBR-II. These test fuel pins had fuel slugs 343 mm in length, approximately 4.3-5.7 mm in diameter, Zr content of 6-14 wt.% and Pu content of 0 wt.% (U-Zr binary) to 26 wt.% (Ogata, 2012). Attention must be paid when these two codes are applied to a fuel pin with specifications that are largely different from the EBR-II test fuel pins. The AFC-1H fuel pin has a higher Zr content (30 wt.%) and much shorter fuel slug length (37.18 mm) than those of the EBR-II test fuel pins. Fuel burnup of about 27 at.% of the AFC-1H is also higher than that of the EBR-II test fuel pins.

Figures 4.21 and 4.22 show the results of the cladding and fuel temperature calculations, performed respectively by MACSIS and ALFUS. The difference in the temperature curves between both codes can be attributed to differences in the modeller’s assumptions for the uncertain peak inner cladding temperature, which has been evaluated at a value ranging from 480°C to 500°C at the beginning of the irradiation, i.e. 20°C uncertainty. The difference in the temperature calculation model between MACSIS and ALFUS also has an influence on the calculation results for the fuel and cladding temperature. For example, ALFUS considers axial heat conduction through the bond sodium above the fuel slug while MACSIS does not.

Figure 4.21. Cladding mid-wall temperatures at beginning of life and end of irradiation (AFC 1H – rodlet 4)

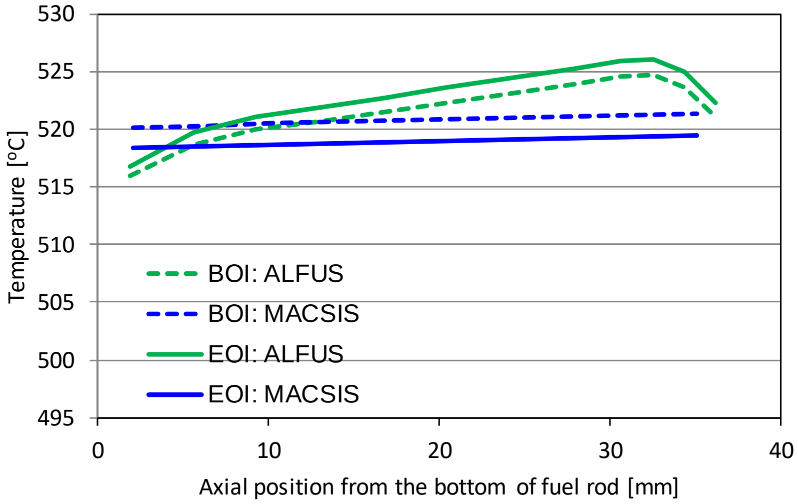

Note: BOI: beginning of irradiation; EOI: end of irradiation.
Source: NEA EGIF data, 2019.

Figure 4.22. Radial distributions of fuel temperatures at beginning of irradiation and end of irradiation (AFC 1H – rodlet 4)

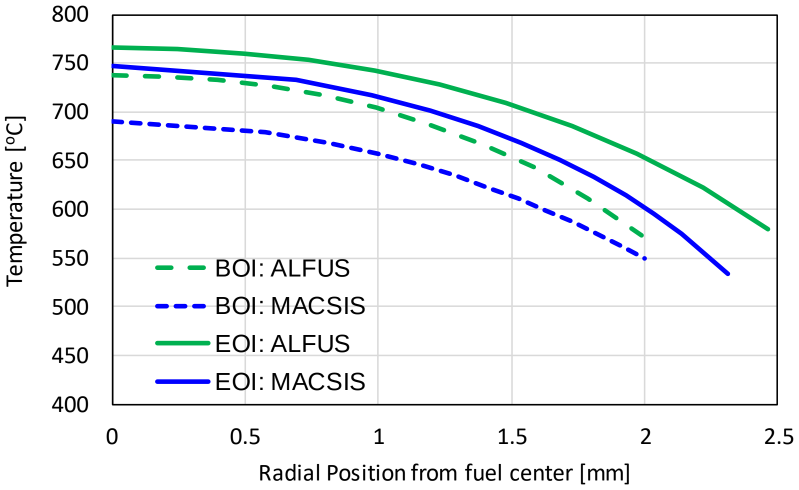

Note: BOI: beginning of irradiation; EOI: end of irradiation.
Source: NEA EGIF data, 2019.

Figure 4.23 compares the measured fuel slug axial elongation with the one calculated using the two codes. U-Zr and U-Pu-Zr metal fuel slugs show larger radial swelling than axial swelling before the fuel slug contact with the cladding. This anisotropic swelling is due to radial cracking in the slug and tearing at the grain boundary of orthorhombic (alpha)-

uranium, which causes anisotropic irradiation growth (Ogata, 2012). The EBR-II test fuel pins having 75% fuel smear density (the cross-sectional area ratio of the fuel slug to the cladding inside) typically exhibited axial swelling of 3-8% while radial swelling amounted to 15.5% $=100\text{x}((100/75)^{1/2}-1)$ at the fuel-cladding contact, hence the axial/radial swelling ratio was in the range of approximately 0.2-0.5. For the AFC-1H fuel pin of 65% fuel smear density, radial swelling should be 24% $=100\text{x}((100/65)^{1/2}-1)$, hence the measured data of 13% axial elongation means an axial/radial ratio of 0.54, which is close to the range of the EBR-II irradiation test data. Agreement between the ALFUS calculation and the AFC-1H measured data for fuel slug axial elongation suggests that the radial cracking model installed in ALFUS is applicable to a high Pu content (as high as 30 wt.%) and short (37.18 mm) fuel slug. The result found with MACSIS, 6%, is about half of measured axial elongation, which is the typical value for a U-Pu-Zr fuel pin with 75% fuel smear density irradiated at a high linear power rate.

Figure 4.23. Fuel slug elongation history (AFC 1H – rodlet 4)

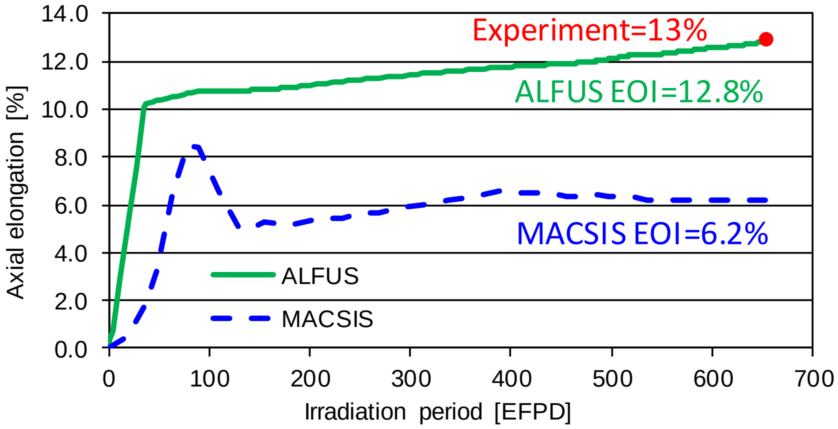

Note: EOI: end of irradiation; EFPD: effective full power day
Source: NEA EGIF data, 2019.

Figure 4.24 shows a comparison between gas plenum volumes measured after irradiation and the value calculated by the two codes. The gas plenum volume of a sodium-bonded metal fuel pin decreases along with extrusion of the bond sodium in the fuel slug-cladding gap in the course of the fuel slug swelling during irradiation. Infiltration of part of bond sodium into the swollen, porous fuel slug moderates the decrease in the gas plenum volume. Both of the codes reproduce well the measured gas plenum volume.

Figure 4.24. Plenum volume history (AFC 1H – rodlet 4)

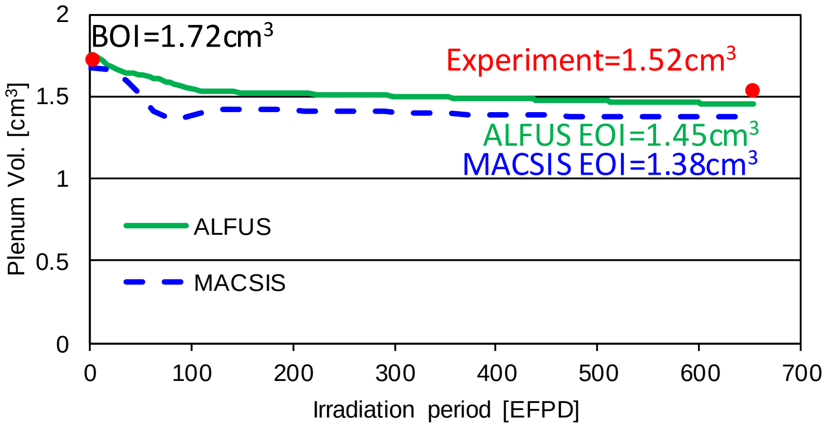

Note: EOI: end of irradiation; EFPD: effective full power day
Source: NEA EGIF data, 2019.

MACSIS predicts well the measured fission gas release, as shown in Figure 4.25, while ALFUS slightly overestimates it.

Figure 4.25. Fission gas release history (AFC 1H – rodlet 4)

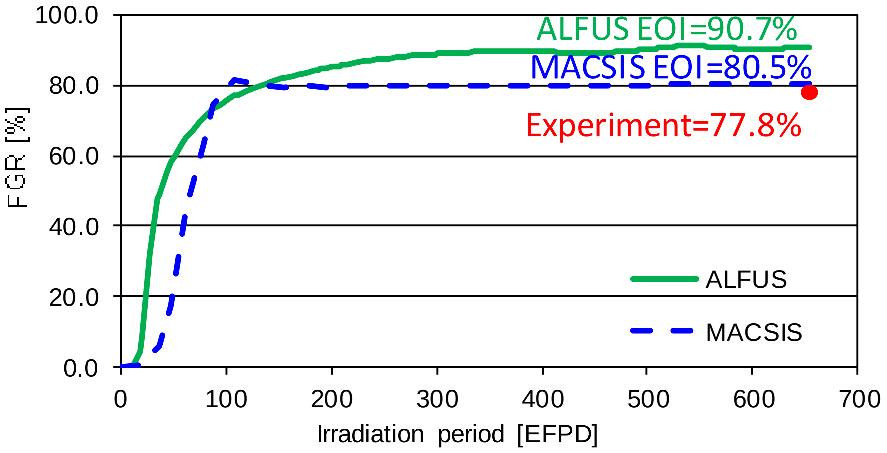

Note: EOI: end of irradiation; FGR: Fission gas release; EFPD: effective full power day
Source: NEA EGIF data, 2019.

The difference in the FCCI calculation results between MACSIS and ALFUS, shown in Figure 4.26, can be attributed to the difference in the FCCI models installed in the two codes. The FCCI in the metal fuels during steady-state irradiation can be characterised by the metallurgical reaction between the lanthanide fission products and iron-base cladding alloys (Ogata, 2012; NEA, 2014), and generally increases with increasing cladding temperature and increasing fuel burnup. It is also considered to be dependent on the linear power rate. However, the combined effect of the cladding temperature, fuel burnup and linear power rate on the FCCI at an axial position is not well understood at present, and the FCCI calculations of the AFC-1H fuel pin can be considered as an extrapolation in terms of the fuel burnup. Improvements in the FCCI models are desired in the future.

Figure 4.26. Axial distribution of fuel-cladding chemical interactions thickness (AFC 1H – rodlet 4)

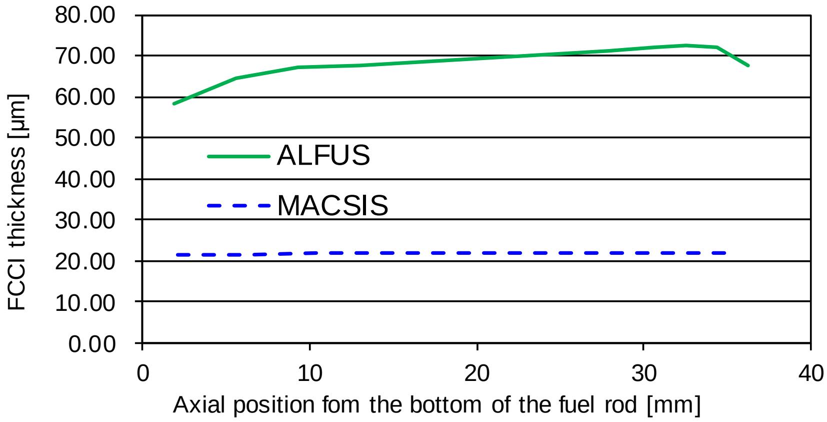

Note: FCCI: fuel-cladding chemical interaction.
Source: NEA EGIF data, 2019.

Both codes predicted insignificant cladding diametral strain of less than 0.1%, which is consistent with the measured data. Such an insignificant diametral strain, in spite of higher burnup than 20 at.%, can be attributed to suppressed FCMI due to a low smear density (65%) and a small plenum gas pressure rise resulted from a relatively large plenum to fuel volume ratio.

4.2.2. Results of the benchmark on the irradiation X501

Table 4.5 shows the results of calculations from the different codes, comparing them with results of the experiments.

The EBR-II test fuel assembly, X501, irradiated up to about 7.6 at.%. The test fuel pin in X501 contained a U-Pu-Zr fuel slug bearing a small amount of MA, specifically U-20.2Pu-9.1Zr-1.3Np-1.2Am (in wt.%). The specification of the X501 test fuel pin is similar to those of typical EBR-II test fuel pins, with which both the MACSIS and ALFUS codes were validated.

Table 4.5. Irradiation X501: Comparison of experimental and calculation results

X501	Measurements	ALFUS	MACSIS
Burnup (at.%)	7.6	7.6	7.6
Fission gas (Xe+Xr) release (%)	79	79	63.7
Final pin pressure (MPa)	2.45 MPa (32°C)		4.62 (482°C) 1.70 (22°C)
Diameter gap fuel slug-clad (µm)	0 (full contact)	0 (full contact)	0 (full contact)
Zr redistribution	Semi-quantitative measurement		–
Fuel slug elongation (%)	2.6	2.5	6.3
Exterior clad diameter increase (%)	n/a	n/a	0.13
FCCI thickness (µm)	n/a	n/a	n/a
Maximum fuel slug centreline temperature (°C)	Not measured	690	703
Maximum fuel slug surface temperature (°C)	Not measured		543
Maximum cladding inner wall temperature (°C)	Not measured	550	540
Maximum fast fluence (E>0.1 MeV) (neutrons/m^2)	n/a	6.5×10^{22}	6.41×10^{26} (using tentative maximum fast neutron flux: 2.33×10^{19} neutrons/m^2·sec)
Maximum dose on clad (DPA)	n/a		–
Final plenum volume (cc)	n/a		4.89

Note: FCCI: fuel-cladding chemical interaction; DPA: displacements per atom.

Figures 4.27 and 4.28 show the results of cladding and fuel temperature calculations with MACSIS and ALFUS. Some discrepancies in the temperature curves between MACSIS and ALFUS were noticed and may be attributed to differences in the calculators' assumptions due to unknown irradiation conditions, such as the linear power profile and history, which were provided in graphs, not as a table or correlation.

The measured data (2.6%) of the fuel slug axial elongation, as shown in Figure. 4.29, is in the lower bound of the EBR-II irradiation test data band. This low axial elongation is caused by highly anisotropic swelling due to a large radial crack, which is characteristic of a U-Pu-Zr fuel pin with a 75% fuel smear density irradiated at a high linear power rate. ALFUS predicts well the axial elongation measured for X501, while MACSIS overestimates it.

Figure 4.27. Cladding mid-wall temperatures at beginning of irradiation and end of irradiation (X501)

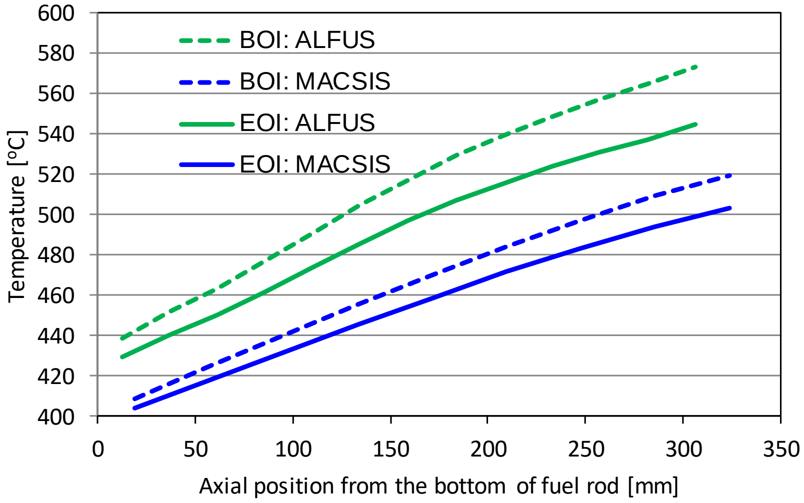

Note: BOI: beginning of irradiation; EOI: end of irradiation.
Source: NEA EGIF data, 2019.

Figure 4.28. Radial distributions of fuel temperatures at beginning of irradiation and end of irradiation (X501)

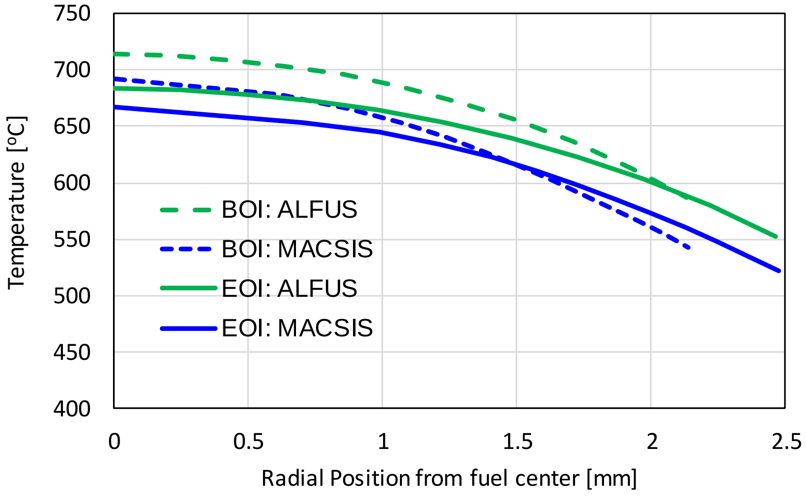

Note: BOI: beginning of irradiation; EOI: end of irradiation.
Source: NEA EGIF data, 2019.

The measured fission gas release (80%) for X501 is a typical value of the EBR-II irradiation test data. As indicated in Figure 4.30, the calculations of fission gas release with ALFUS are close to the measured value, while the results of MACSIS calculations lead to a relatively lower value.

Both MACSIS and ALFUS codes calculate a very low level of cladding diametral deformation. This is consistent with the measured cladding outer diameter shown in Figure 4.31, which is even smaller than the nominal value (5.84 mm = 0.2299 inch). The difference between the outputs of both codes is not significant at this level of deformation.

Figure 4.29. Fuel slug elongation history (X501)

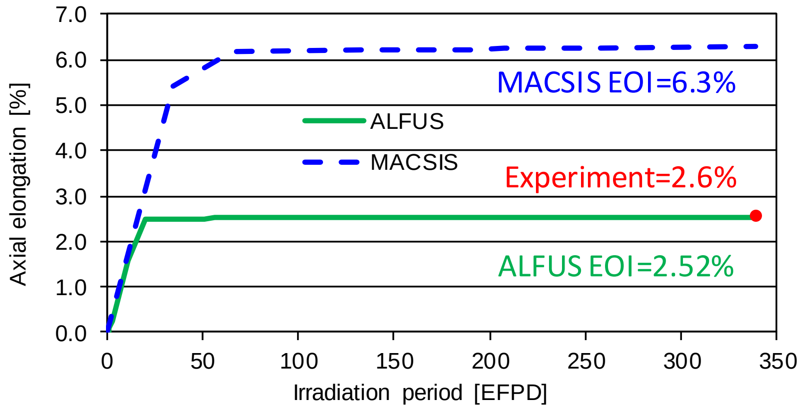

Note: EOI: end of irradiation; EFPD: effective full power day.
Source: NEA EGIF data, 2019.

Figure 4.30. Fission gas release history (X501)

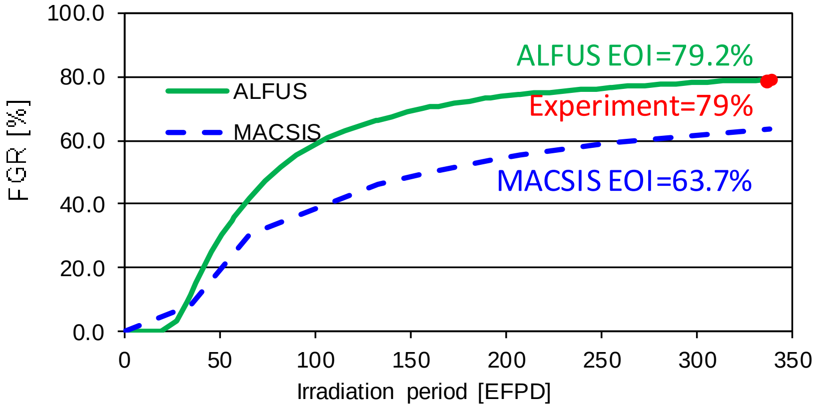

Note: FGR: Fission gas release; EOI: end of irradiation; EFPD: effective full power day.
Source: NEA EGIF data, 2019.

Figure 4.31. Axial distribution of cladding diameter at end of irradiation (X501)

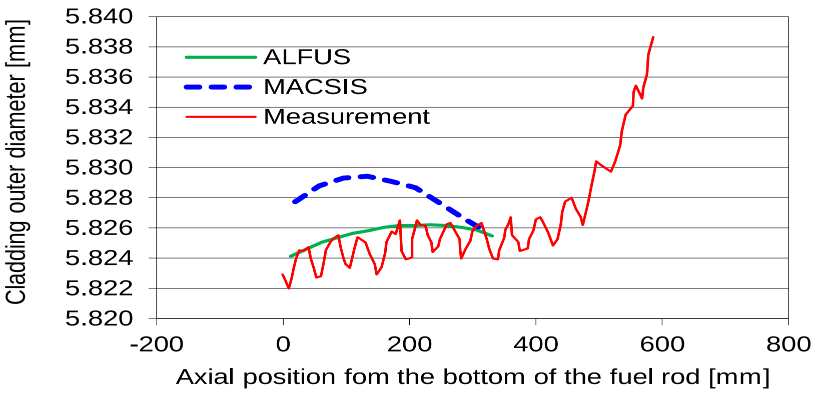

Source: NEA EGIF data, 2019.

4.2.3. Results of the benchmark on the irradiation SMIRP-1

Table 4.6 shows the results of calculations from the different codes and comparisons with the results of the experiments.

Table 4.6. Irradiation SMIRP-1: Comparison of experimental and calculation results

SMIRP-1	Measurements	ALFUS	MACSIS
Burnup (at.%)	2.4 (average burnup for six fuel pins)	U-10Zr: 2.4 U-10Zr-5Ce: 2.84	2.4
Fission gas (Xe+Xr) release (%)	U-10Zr: 53.9 U-10Zr-5Ce: 47	U-10Zr: 15 U-10Zr-5Ce: 20	46
Final pin pressure (MPa)	Not measured		0.39 (397°C) 0.17 (22°C)
Diameter gap fuel slug-clad (µm)	0 (fuel slug contacts with cladding along fuel axis)	U-10Zr: partly closed U-10Zr-5Ce: almost closed	0 (full contact)
Zr redistribution	See Figure 4.34	n/a	See Figure 4.34
Fuel slug elongation (%)	U-10Zr: 10~12% U-10Zr-5Ce: 6~8%	U-10Zr: 12.7 U-10Zr-5Ce: 12.8	10.4
Exterior clad diameter increase (%)	Not measured	<0.0005	<0.01
FCCI thickness (µm)	0 (Cr barrier is present between fuel and cladding)	0	0
Maximum fuel slug centerline temperature (°C)	<617	U-10Zr: 510 U-10Zr-5Ce: 520	549
Maximum fuel slug surface temperature (°C)	–	U-10Zr: 430 U-10Zr-5Ce: 430	463
Maximum cladding inner wall temperature (°C)	–	U-10Zr: 425 (mid-wall) U-10Zr-5Ce: 405	452
Maximum fast fluence (E>0.1 MeV) (neutrons/m^2)	– (fuels were irradiated in HANARO, which is a thermal reactor)		–
Maximum dose on clad (DPA)	– (fuels were irradiated in HANARO, which is a thermal reactor)		–
Final plenum volume (cc)	U-10Zr: 1.43 U-10Zr-5Ce: 1.31	U-10Zr: 1.49 U-10Zr-5Ce: 1.48	1.34

Note: FCCI: fuel-cladding chemical interaction; DPA: displacements per atom.

In the SMIRP-1 irradiation test, two short (50 mm in length) U-10Zr and U-10Zr-5Ce (in wt.%) fuel slugs were irradiated up to about 2.4 at.% burnup. These test fuels are beyond the fuel specification range with which MACSIS and ALFUS have been validated so far. Attention must be paid to the radial power profile in the fuel slugs because they are not uniform as shown in Figure 3.13 due to thermal spectrum neutron irradiation. According to the report on the feasibility study of the SMIRP-1 irradiation test in HANARO (Cheon and Kim, 2010), the effect of the radial power profile on the fuel slug temperature is less than 10°C, which can be ignored from the standpoint of the irradiation test feasibility. However, the radial power profile shown in Figure 3.13 leads to a large variation in the local fuel burnup rate, approximately a 50% higher burnup rate at the fuel slug peripheral region than at the central region. This local burnup rate variation affects the fuel irradiation behaviour such as fission gas release, which is closely related to local fuel swelling rate.

The results of cladding and fuel temperature calculations by the two codes are shown in Figures 4.32, 4.33 (U-Zr), 4.40 and 4.41 (U-Zr-Ce). There is a 20°C difference between fuel slug temperature calculated with MACSIS and that calculated with ALFUS. This is mainly due to the difference in the assumptions of the axial linear power profile. In the MACSIS calculation, an axially uniform power profile was assumed, while in the ALFUS calculation, an inclined linear profile (about 20% higher at the bottom of the fuel slug than at the top) was assumed based on the result of auto-gamma radiography of the irradiated SMIRP-1 fuel. Difference in the temperature calculation modes, i.e. the axial heat conduction considered in ALFUS as explained in Section 4.2.1, also affects the fuel temperature calculation results. It should be noted that the current version of ALFUS cannot allow radially non-uniform power profile. If ALFUS considered the radial power profile as indicated in Figure 3.13, it would calculate less than 10°C lower fuel slug temperature than those shown in Figures 4.33 and 4.41. Although this enhances the difference from the fuel slug temperature calculated by MACSIS, such a difference in the calculated fuel slug temperature, less than 30°C, would not significantly affect other irradiation behaviour calculations.

Figure 4.32. Cladding mid-wall temperatures at beginning of irradiation and end of irradiation (SMIRP-1 U-Zr)

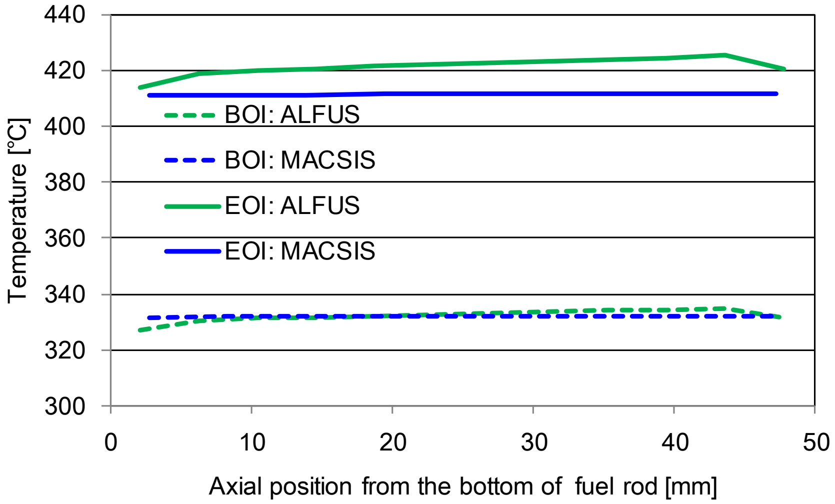

Note: BOI: beginning of irradiation; EOI: end of irradiation.
Source: NEA EGIF data, 2019.

In U-Zr and U-Pu-Zr metal fuels, fuel alloy constituents, in particular, U and Zr, redistribute in accordance to the radial temperature profile in the fuel slug. This behaviour is due to the thermo-diffusion phenomenon caused by chemical potential gradients of the fuel constituents produced by radial temperature distribution. Figure 4.34 shows the comparison of radial Zr content profile between the measurements and the results calculated with MACSIS. From the fuel temperature calculations, all of the fuel slugs of the SMIRP-1 fuel pins were in the alpha-delta two-phase region of U-Zr alloy. Considering that Zr solubility in U alpha-phase increases with increasing temperature, the Zr migration to the hotter part is plausible. The measured result indicates that Zr migration to the central, hotter part of the fuel slug and MACIS reproduces the qualitative trend of the measurement.

Figure 4.33. Radial distributions of fuel temperatures at beginning of irradiation and end of irradiation (SMIRP-1 U-Zr)

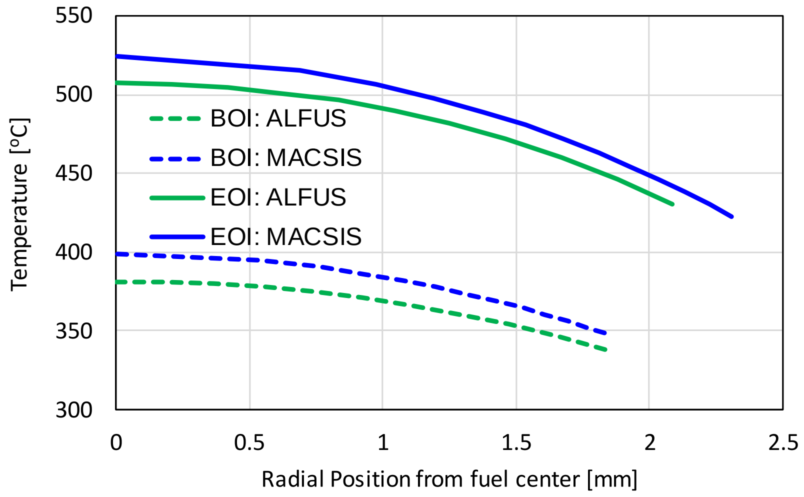

Note: BOI: beginning of irradiation; EOI: end of irradiation.
Source: NEA EGIF data, 2019.

Figure 4.34. Zr distribution along radial direction at end of irradiation (SMIRP-1 U-Zr)

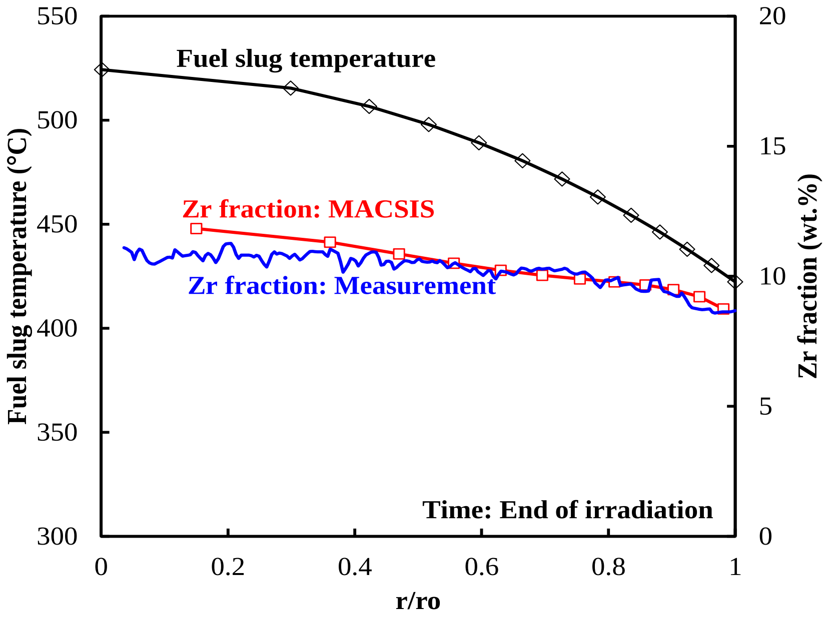

Source: NEA EGIF data, 2019.

Figures 4.35 (U-Zr) and 4.42 (U-Zr-Ce) show the calculated axial distributions of the fuel-cladding gap width at the end of irradiation. Figures 4.36 (U-Zr) and 4.43 (U-Zr-Ce) show the calculated histories of the maximum fuel-cladding gap width. The PIE results indicated that the gaps in both fuel pins were closed for all the axial positions. MACSIS calculations shown in Figures 4.35 and 4.42 agree with the PIE results. The dotted lines in the figures indicate “the fuel slug radial strain equivalent to the radial crack at fuel-cladding contact” that is assumed in ALFUS. In other words, ALFUS estimates that the radially cracked fuel slug comes into contact with cladding when the fuel-cladding gap reaches the dotted lines in Figures 4.35 and 4.42. The ALFUS calculation shown in Figure 4.35 shows the fuel-cladding contact at 0-15 mm from the bottom of the U-Zr slug. If ALFUS considered radial power profile as depicted in Figure 3.13, it would predict a full fuel-cladding contact since larger gas swelling would be calculated at the peripheral, higher burnup region of the fuel slug. As for U-Zr-Ce fuel (Figure 4.42), ALFUS predicts almost full contact, which is consistent with the PIE results.

Figure 4.35. Axial distribution of fuel-cladding gap at end of irradiation (SMIRP-1 U-Zr)

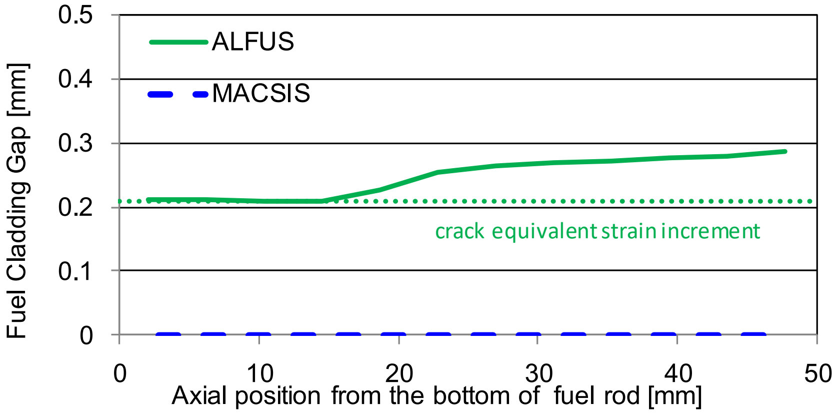

Source: NEA EGIF data, 2019.

Figure 4.36. Fuel-cladding gap history (SMIRP-1 U-Zr)

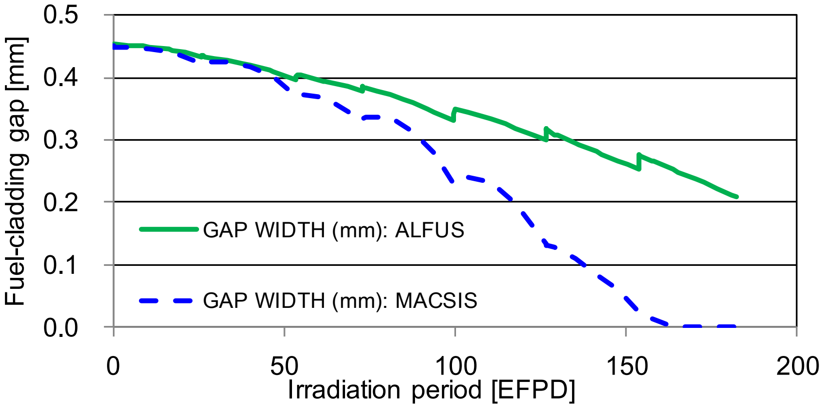

Note: EFPD: effective full power day.
Source: NEA EGIF data, 2019.

Figures 4.37 (U-Zr) and 4.44 (U-Ce-Zr) compare the measured fuel slug axial elongations at the end of irradiation with the histories calculated by the two codes. Both codes consistently reproduce the measured data. Large (>10 %) axial elongations were calculated by both codes. This is because in the 65% fuel smear density fuels for SMIRP-1, a larger gas swelling, compared to those for 75% fuel smear density fuels in the EBR-II irradiation tests, is calculated before the fuel-cladding contact. It should be noted that the fuel slug axial elongation of 12% of the SMIRP-1 U-Zr fuel is equivalent to those of the AFC-1H. The relatively smaller axial elongation of 8% of the SMIRP-1 U-Zr-Ce fuel, compared to the U-Zr fuel, might be attributed to a higher rate of radial cracking enhanced by embrittlement of the U-10 wt.%Zr alloy due to the addition of Ce, which has a low (<1 wt.%) solubility in the U-Zr alloy and may cause Ce precipitation at the grain boundaries.

Figure 4.37. Fuel slug elongation history (SMIRP-1 U-Zr)

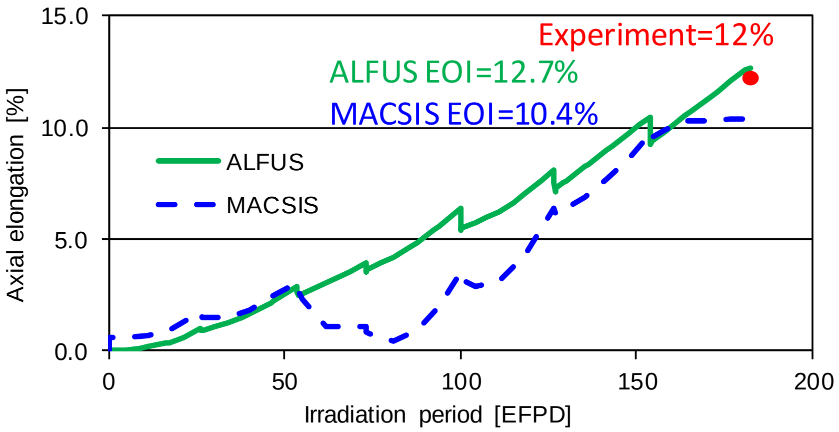

Note: EOI: end of irradiation; EFPD: effective full power day.
Source: NEA EGIF data, 2019.

The measured gas plenum volumes at the end of irradiation were compared with those histories calculated by the two codes in Figures 4.38 (U-Zr) and 4.45 (U-Zr-Ce). Both codes were in good agreement with the measured data, which is reasonable since MACSIS and ALFUS predict well the measured data of fuel slug radial deformation (fuel-cladding gap width) and axial elongation.

Figure 4.38. Plenum volume history (SMIRP-1 U-Zr)

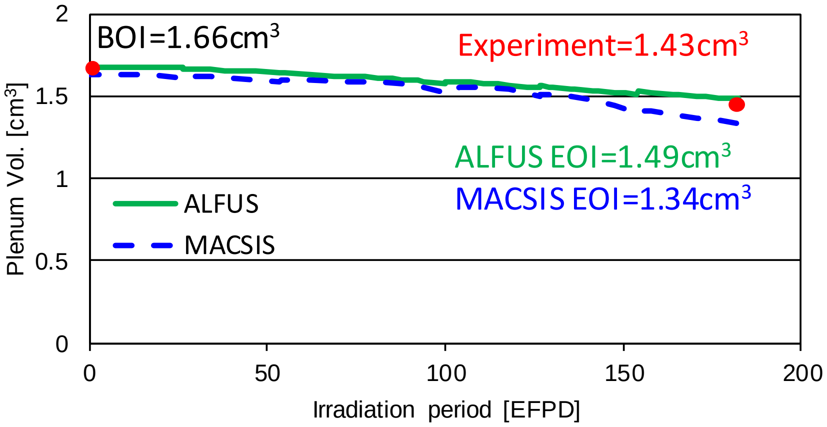

Note: BOI: beginning of irradiation; EOI: end of irradiation; EFPD: effective full power day.
Source: NEA EGIF data, 2019.

Figures 4.39 (U-Zr) and 4.46 (U-Zr-Ce) show the comparison between the measured fission gas release data at the end of irradiation with the values calculated using the two codes. The MACSIS calculations are in good agreement with the measured data. On the other hand, the values calculated by ALFUS are lower than the measured data. This may be explained by the assumption of radially uniform power profile in ALFUS, which is inconsistent with the actual radial power profile. In the SMIRP-1 fuels, the peripheral region of the fuel slug burnt more than the average fuel burnup shown in Table 4.6, which led to the enhancement of coalescence among fission gas bubbles, open pore formation and fission gas release through the open pore. ALFUS underestimates the local burnup at the peripheral region, open pore formation and the fission gas release.

Figure 4.39. Fission gas release history (SMIRP-1 U-Zr)

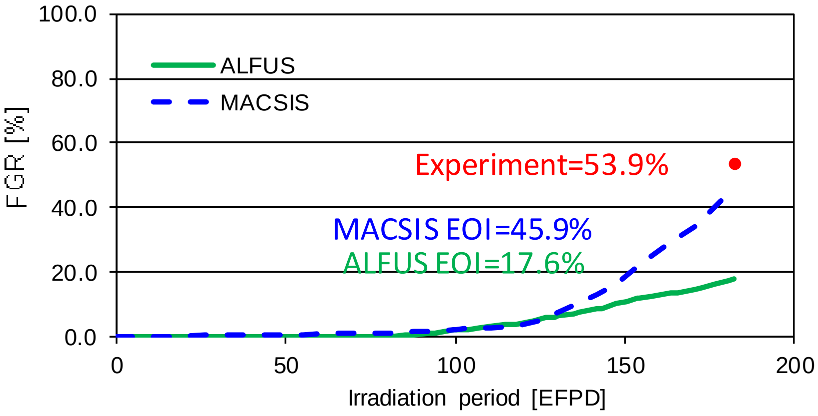

Note: FGR: Fission gas release; EFPD: effective full power day.
Source: NEA EGIF data, 2019.

Figure 4.40. Cladding mid-wall temperatures at beginning of irradiation and end of irradiation (SMIRP-1 U-Zr-Ce)

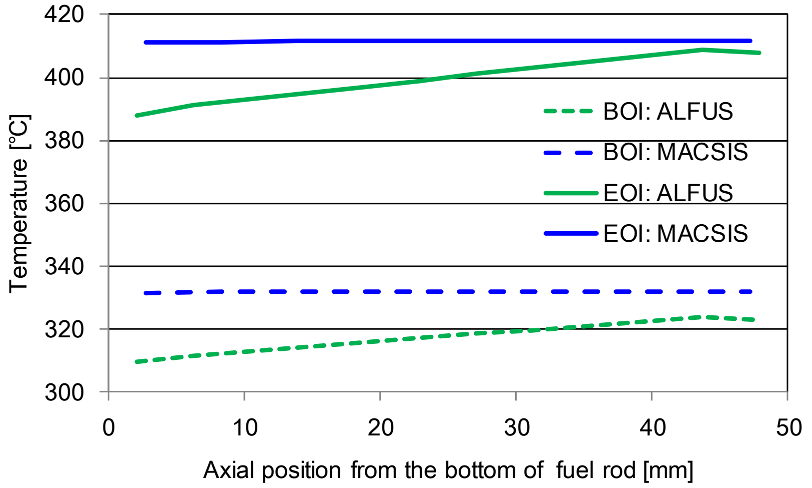

Note: BOI: beginning of irradiation; EOI: end of irradiation.
Source: NEA EGIF data, 2019.

Figure 4.41. Radial distributions of fuel temperatures at beginning of irradiation and end of irradiation (SMIRP-1 U-Zr-Ce)

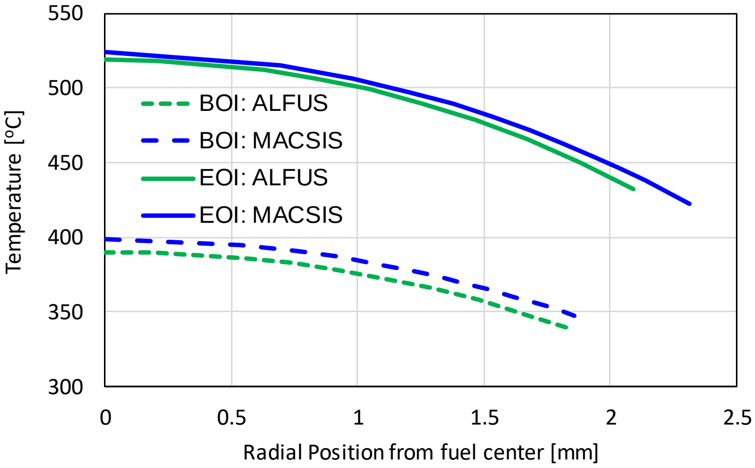

Note: BOI: beginning of irradiation; EOI: end of irradiation.
Source: NEA EGIF data, 2019.

Figure 4.42. Axial distribution of fuel-cladding gap at end of irradiation (SMIRP-1 U-Zr-Ce)

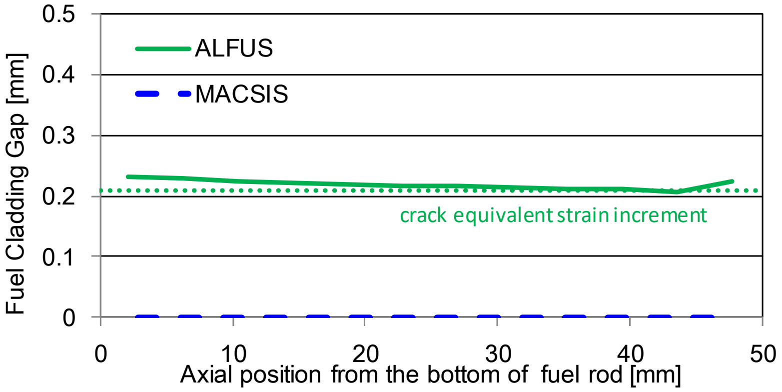

Source: NEA EGIF data, 2019.

Figure 4.43. Fuel-cladding gap history (SMIRP-1 U-Zr-Ce)

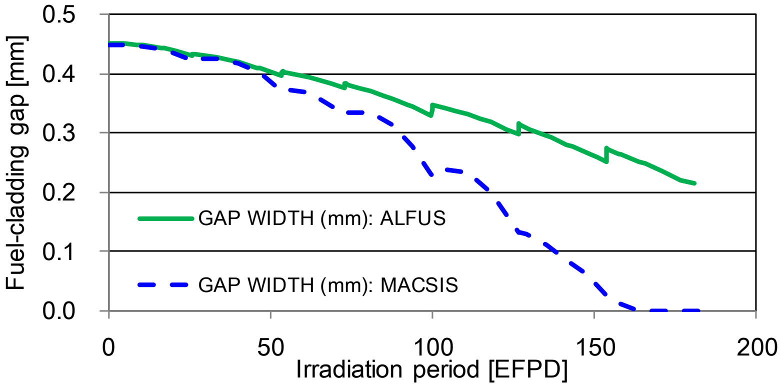

Note: EOI: end of irradiation; EFPD: effective full power day.
Source: NEA EGIF data, 2019.

Figure 4.44. Fuel slug elongation history (SMIRP-1 U-Zr-Ce)

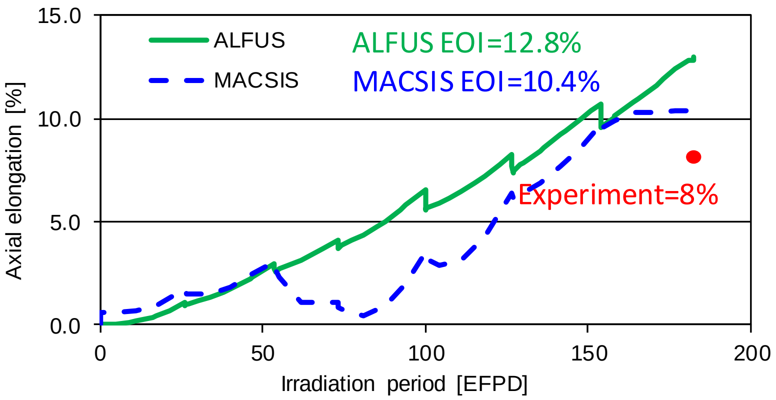

Note: EFPD: effective full power day.
Source: NEA EGIF data, 2019.

Figure 4.45. Plenum volume history (SMIRP-1 U-Zr-Ce)

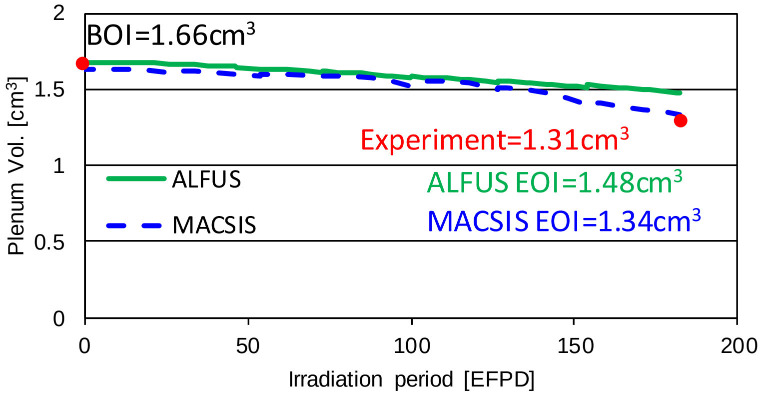

Note: BOI: beginning of irradiation; EOI: end of irradiation; EFPD: effective full power day.
Source: NEA EGIF data, 2019.

Figure 4.46. Fission gas release history (SMIRP-1 U-Zr-Ce)

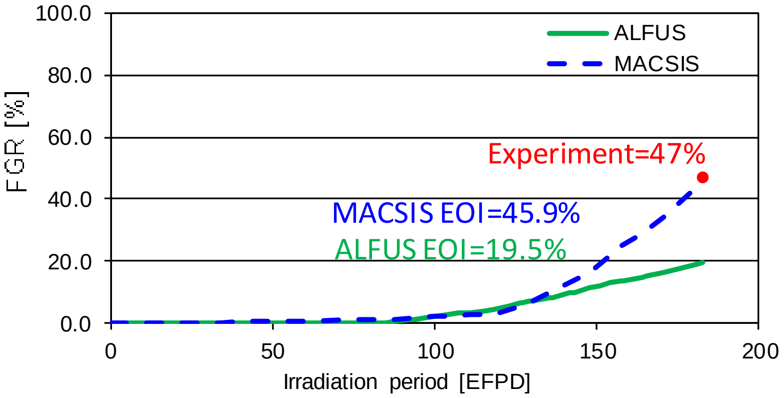

Note: FGR: Fission gas release; EOI: end of irradiation; EFPD: effective full power day.
Source: NEA EGIF data, 2019.

4.2.4. Results of the benchmark on the irradiation METAPHIX-2

Table 4.7 presents the results of the calculations from the different codes and comparisons with results from the experiments on the irradiation METAPHIX-2.

Table 4.7. Irradiation METAPHIX-2 #3 pin: Comparison of experimental and calculation results

METAPHIX-2 #3 pin	Measurements	ALFUS	MACSIS
Burnup (at.%)	5.7-6.9 at ~305 m	6.4 at ~310 mm	6.5
Fission gas (Xe+Xr) release (%)	68.6	77.1	68.5
Final pin pressure (MPa)	1.7 (21.4C)	4.74 (503°C)	4.0 (507°C) 1.4 (22°C)
Diameter gap fuel slug-clad (µm)	0 (contact)	0 (contact)	0 (contact)
Zr redistribution			See Figure 4.49
Fuel slug elongation (%)	3.5	4.3	5.2
Exterior clad diameter increase (%)	0.3 at 350 mm	0.4 at 200 mm	0.12 (HT9)~0.47 (D9)
FCCI thickness (µm)	Not measured	Not applicable to austenitic cladding	39
Maximum fuel slug centreline temperature (°C)		675	675
Maximum fuel slug surface temperature (°C)		575	559
Maximum cladding inner wall temperature (°C)		545 (mid-wall)	555
Maximum fast fluence (E>0.1 MeV) (neutrons/m^2)		9.7×10^{22}	9.64×10^{26}
Maximum dose on clad (DPA)	48		–
Final plenum volume (cc)	8.3	9.4	8.3

Note: FCCI: fuel-cladding chemical interaction; DPA: displacements per atom.

Unlike for the AFC-1H and the SMIRP-1, the irradiation conditions and specifications of the METAPHIX-2 test fuel pin are comparable to those of the EBR-II test fuel pins, which were used for the validation of MACSIS and ALFUS, except for relatively longer fuel stack (485 mm), 5 wt.% MA and 5 wt.% lanthanides additions in the METAPHIX-2 fuel pin.

Figures 4.47 and 4.48 show the cladding and fuel slug temperatures calculated by MACSIS and ALFUS. The results calculated with both codes are in fair agreement with each other.

Figure 4.49 displays the measured radial Zr distribution at the end of irradiation in comparison with the MACSIS-calculated radial Zr distribution. The boundary between the lower temperature delta-containing phase region and the mid-temperature zeta phase-dominant region appears to exist roughly at r/r0=0.4 from the measured Zr profile and the cross-sectional metallography. MACSIS also indicates this boundary at a similar position. However, MACSIS does not reproduce remarkable depression in Zr concentration at the central region, although the measured data are based on qualitative SEM-EDS. Some modifications may be needed for the fuel constituent migration model in MACSIS. ALFUS is not capable of calculating fuel constituent migration.

Figure 4.47. Cladding mid-wall temperatures at beginning of irradiation and end of irradiation (METAPHIX-2 #3 pin)

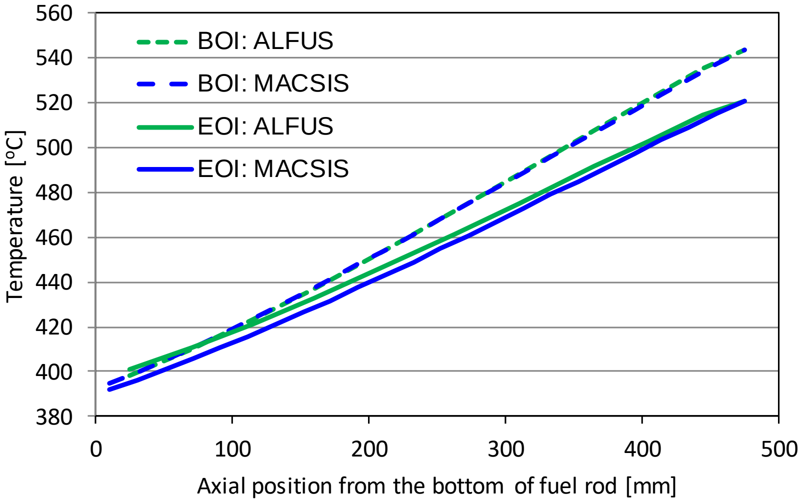

Note: BOI: beginning of irradiation; EOI: end of irradiation.
Source: NEA EGIF data, 2019.

Figure 4.48. Radial distributions of fuel temperatures at beginning of irradiation and end of irradiation (METAPHIX-2 #3 pin)

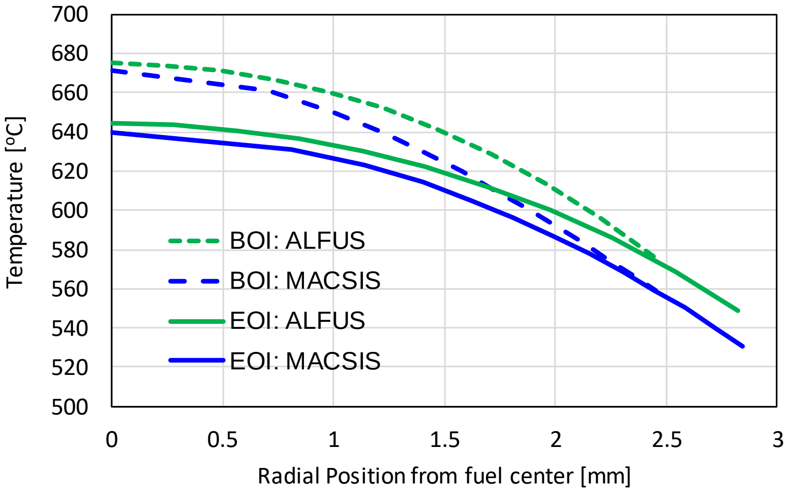

Note: BOI: beginning of irradiation; EOI: end of irradiation.
Source: NEA EGIF data, 2019.

Figure 4.49. Zr distribution along radial direction at end of irradiation (METAPHIX-2 #3 pin)

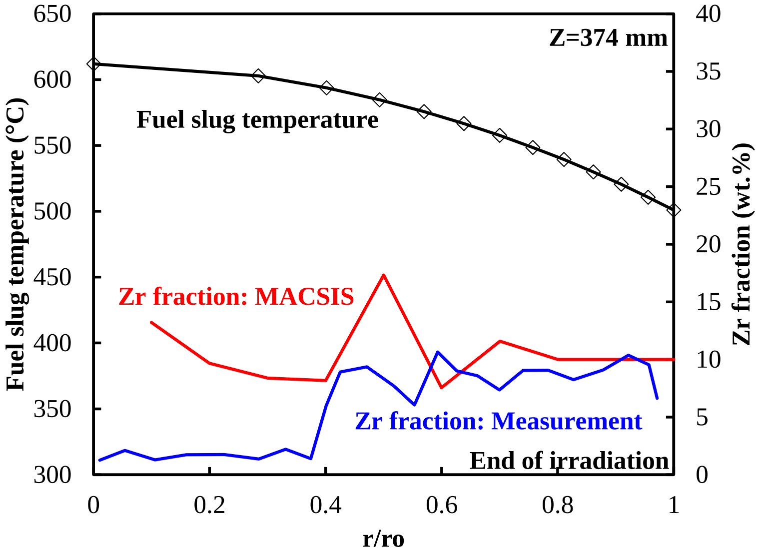

Source: NEA EGIF data, 2019.

Figure 4.50 compares the measured axial fuel slug elongation at the end of irradiation with that history calculated by the two codes. Both codes predict relatively higher values than the measured data. The fuel stack of the METAPHIX-2 consisted of a number of short (20-50 mm in length) fuel slugs, so that local axial elongations of lower, medium and higher parts of the fuel stack were able to be determined from the neighbouring slug boundaries observed in the scanning gamma spectroscopy of the irradiated fuel pin. The red-coloured solid line in Figure 4.51 indicates the determined local axial elongations. Although the values calculated by both codes (dotted lines in the figure) show a flatter distribution of local axial elongation than the measured data, the calculated value trends in the upper part of the slug showing higher axial elongation are in a qualitative agreement with the measured data trend.

Figure 4.50. Fuel slug elongation history (METAPHIX-2 #3 pin)

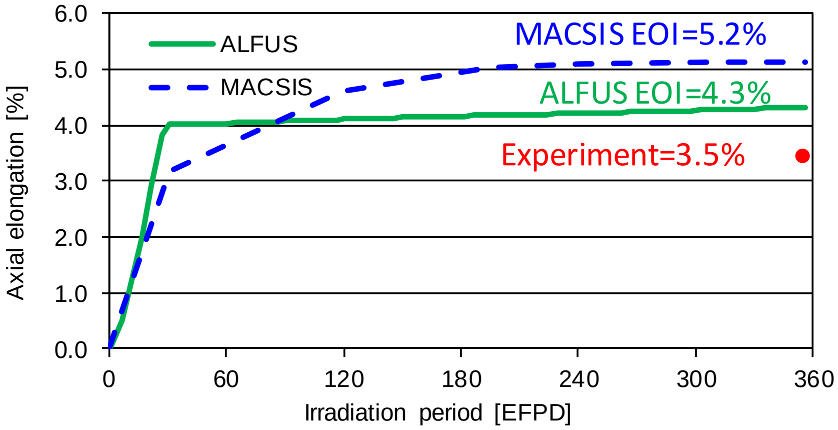

Note: EOI: end of irradiation; EFPD: effective full power day.
Source: NEA EGIF data, 2019.

Figure 4.51. Axial elongation of each composition zone at end of irradiation (METAPHIX-2 #3 pin)

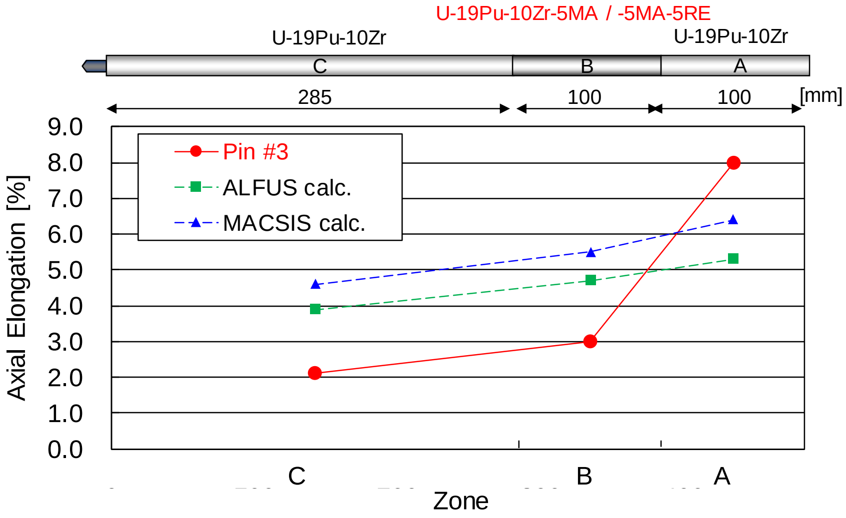

Source: NEA EGIF data, 2019.

Figures 4.52 and 4.53 show the measured data of the gas plenum volume and fission gas release, respectively, at the end of irradiation, compared with the values calculated by MACSIS and ALFUS. Both codes reproduce well these measured data.

Figure 4.52. Plenum volume history (METAPHIX-2 #3 pin))

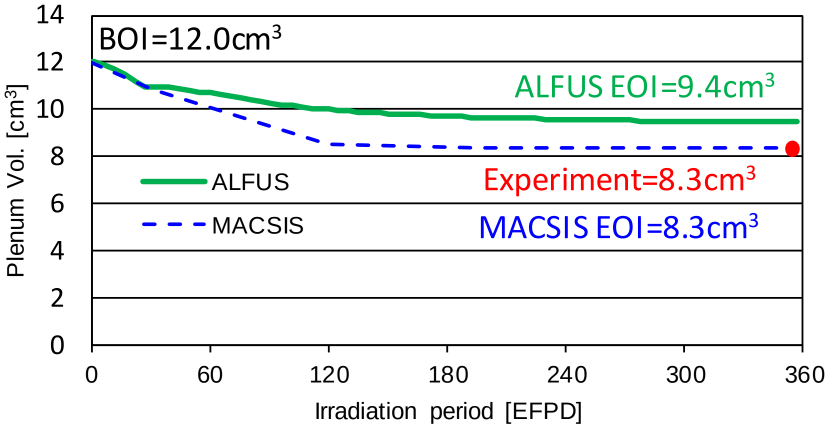

Note: BOI: beginning of irradiation; EOI: end of irradiation; EFPD: effective full power day.
Source: NEA EGIF data, 2019.

The axial distributions of cladding diametral deformation measured by a laser profilometry are compared with those calculated by the two codes, as shown in Figure. 4.54. Since the mechanical properties of the METAPHIX-2 cladding material have not been published, it seems difficult to discuss the results.

Figure 4.53. Fission gas release history (METAPHIX-2 #3 pin)

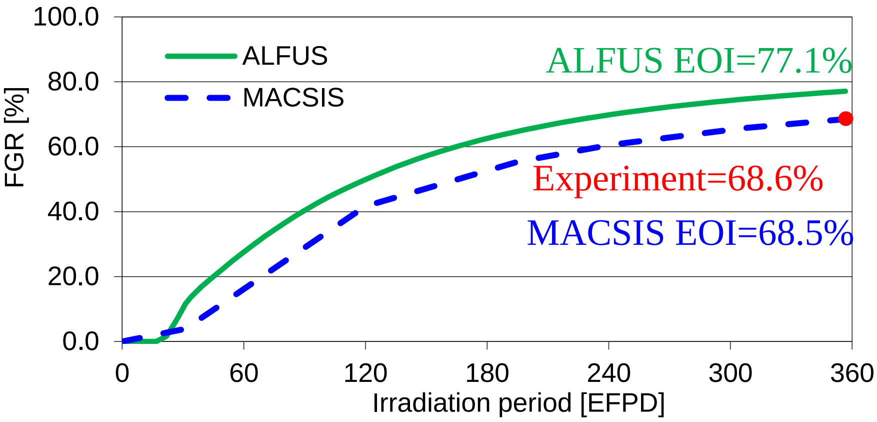

Note: FGR: Fission gas release; EOI: end of irradiation; EFPD: effective full power day.
Source: NEA EGIF data, 2019.

Figure 4.54. Axial distribution of cladding diametrical strain at end of irradiation (METAPHIX-2 #3 pin)

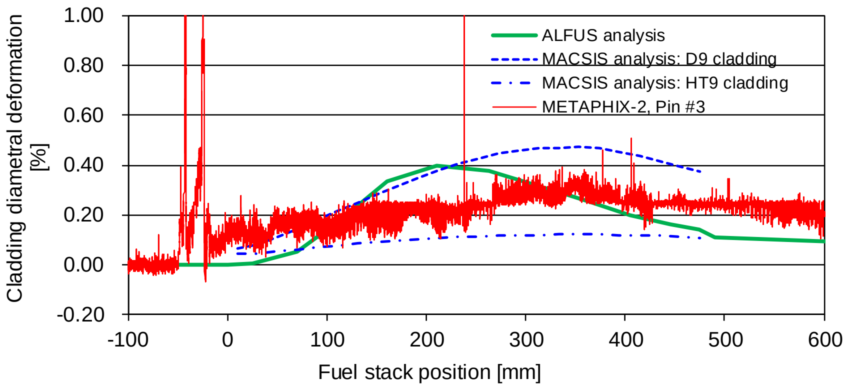

Source: NEA EGIF data, 2019.

4.2.5. Summary and conclusion on the benchmark exercise for metal fuels

The swelling behaviour of short fuel slugs (<50 mm in length) irradiated in the AFC-1H and SMIRP-1 tests may be less affected by self-weight than that of longer fuel slugs. Such short fuel slugs are out of the fuel specification range where the MACSIS and ALFUS codes have been validated. Both codes, however, successfully reproduced the measured data of fuel slug axial elongation, gas plenum volume and fission gas release. This suggests that the two codes are applicable to such short fuel slugs, although some improvements in relevant models of the codes are preferable.

Good agreement between the measured and calculation data has been seen for the X501 and METAPHIX-2 test fuel pins, the specifications of which are almost in the range of MACSIS and ALFUS validation with data from the U-Pu-Zr test fuel pins irradiated in EBR-II. As Ogata (2012) reported, addition of as high as 5 wt.% MA does not affect the mechanical behaviour and fission gas release of U-Pu-Zr fuel up to 7 at.% burnup. This is supported by the present benchmark calculations by MACSIS and ALFUS.

The present benchmark study results indicate that ALFUS and MACSIS have a similar level of capability to simulate metal fuel irradiation behaviour, while the fuel constituent migration and radially non-uniform heat generation cannot be treated in ALFUS.

The addition of MA to metal fuel slugs is considered to influence FCCI and He gas behaviour. FCCI in metal fuels during steady-state irradiation is characterised by cladding inner wall wastage due to a reaction between lanthanide fission products and Fe-base cladding steel. As the chemical behaviour of MA in metal fuel is expected to be similar to that of lanthanide fission products, the MA addition may enhance FCCI. Lanthanide elements that can be entrained by MA in a MA separation process may also assist it. Unfortunately, the present four metal fuel tests have not revealed obvious FCCI, partly due to lower irradiation temperatures and/or lower burnup. Helium gas, which is produced mainly by alpha disintegration of MA, may affect the swelling behaviour of the fuel slug and contribute to increasing plenum gas pressure. However, He behaviour has not yet been observed clearly in the irradiation tests, and a He behaviour model has not been developed to date.

The following work is recommended to fully understand MA-bearing metal fuel irradiation behaviour.

- Obtaining FCCI data of MA-bearing metal fuel pins irradiated at high cladding temperatures (>600°C) up to high local burnups (>10 at.%) to understand the cladding wastage by lanthanide fission products and MA elements, where the cladding temperatures should be evaluated quantitatively (this kind of data is also desirable for standard U-Pu-Zr metal fuels without MA addition).
- Modelling FCCI in metal fuels with/without MA addition, and out-of-pile tests to support the modelling.
- Irradiation tests dedicated to understanding He behaviour in MA-bearing metal fuels.
- Modelling He behaviour in MA-bearing metal fuels, and out-of-pile tests to support the modelling.

For transient performance of metal fuels, which is out of the scope of the present benchmark study, uncertainties in metal fuel properties such as thermal conductivity and solidus temperature significantly influence the prediction of power-to-melting in transient overpower events. In loss-of-flow events, another mode of FCCI, which is the cladding wastage due to the liquefaction reaction above a threshold temperature between the fuel constituents (U and Pu) and Fe-base cladding steel, predominantly controls the time to cladding breach. A benchmark study for such transient performance is preferable for the future.

References

Cheon, J.S. and K. H. Kim (2010), “Feasibility study of the SMIRP-1 irradiation test in HANARO”, SFR-FD330-WR-02-2010 Rev.00, Korea Atomic Energy Research Institute.

Guérin, Y. (2012), “2.21 – Fuel performance of fast spectrum oxide fuel”, *Comprehensive Nuclear Materials*, Vol. 2, pp. 547-578, https://doi.org/10.1016/B978-0-08-056033-5.00043-4.

Kato, M., K. Maeda, T. Ozawa, M. Kashimura and Y. Kihara (2011), “Physical properties and irradiation behavior analysis of Np- and Am-bearing MOX fuels”, *Journal of Nuclear Science and Technology*, Vol. 48/4, pp. 646-653, http://doi.org/10.1080/18811248.2011.9711745.

NEA (2014), *State-of-the-Art Report on Innovative Fuels for Advanced Nuclear Systems*, NEA No. 6895, OECD Publishing, Paris, www.oecd-nea.org/jcms/pl_14574.

Ogata, T. (2012), “3.01 – Metal fuel”, *Comprehensive Nuclear Materials*, Vol. 3, pp. 1-40, https://doi.org/10.1016/B978-0-08-056033-5.00049-5.

Philipponneau, Y. (1992), “Thermal conductivity of (U, Pu)O_{2-x} mixed oxide fuel”, *Journal of Nuclear Materials*, Vol. 188, pp. 194-197, https://doi.org/10.1016/0022-3115(92)90470-6.

Van Uffelen, P., P. Botazzoli, L. Luzzi, S. Bremier, A. Schubert, P. Raison, R. Eloirdi and M.A. Barker (2013), “An experimental study of grain growth in mixed oxide samples with various microstructures and plutonium concentrations”, *Journal of Nuclear Materials*, Vol. 434/1-3, pp. 287-290, https://doi.org/10.1016/j.jnucmat.2012.11.053.

Waltar, A.E. and A.B. Reynolds (1981), *Fast Breeder Reactors*, Pergamon Press Inc.

5. Conclusion and perspectives

This benchmark exercise, which compares the results of code calculations between themselves and with experimental measurements, was the first-of-a-kind benchmark study realised at an international level on fuels loaded with MA. The results of seven experimental irradiations from different experimental reactors were shared and thus allowed each participant to extend their validation database without having to carry out new irradiations whose duration and cost are prohibitive.

Comparison of the results of the different codes showed differences in modelling for both the oxide and metal fuels. An analysis of the discrepancies between the calculations provided by the different codes has provided interesting comments on the differences in modelling (see Chapter 4).

The effect of MA on the fuel behaviour was not significant in both fuels: introducing 2-3% Am in the driver fuel does not change the overall thermomechanical behaviour of the whole pin. Nevertheless, the irradiations studied in this benchmark did not reach high performances in terms of final burnup and transmutation rate. For high performances, the impact of MA on the fuel behaviour must be considered, especially high helium production and release, high gaseous swelling, increase of oxygen potential and properties degradation. These effects could enhance the fuel clad chemical interaction and the fuel clad mechanical interaction, but could also decrease the margin to fuel melting. These effects of MA loading may have consequences for some situations to be considered by safety analysis.

Another source of discrepancies is the set of fuel properties, which are different from one code to another even though the fuel composition is the same. Based on this observation, the EGIF has initiated a new activity on fuel properties that involves sharing experimental property data, analysing the data and making property recommendations along with corresponding uncertainty bands. These recommendations on the properties of fuels will enhance the reliability of the codes' predictions. A database on properties could be developed, as is already the case for nuclear data at the NEA Databank.

Phase 2 of the benchmark exercise will consider the unprotected transient over power and unprotected loss of flow transients since the participants all agreed on the great utility of this type of activity, completing the activities of development and validation of the codes in each laboratory.

List of contributors

Nathalie CHAUVIN (CEA, France)
Marc LAINET (CEA, France)
Simone GIANFELICI (KIT, Germany)
Takayuki OZAWA (JAEA, Japan)
Takanari OGATA (CRIEPI, Japan)
Hirokazu OHTA (CRIEPI, Japan)
June-Hyung KIM (KAERI, Korea)
Chan Bock LEE (KAERI, Korea)
Luca CAPRIOTTI (INL, United States)
Jason HARP (INL, United States)
Heather CHICHESTER (INL, United States)
Paul VAN UFFELEN (JRC Karlsruhe, European Union)
Arndt SCHUBERT (JRC Karlsruhe, European Union)
Stéphanie CORNET (NEA)
Gabriele GRASSI (NEA)